RRFM IGORR 2007

LYON, France 11.3. - 15.3. 2007

Transactions

11th International Topical Meeting

Research Reactor Fuel Management (RRFM)
and
Meeting of the International Group on Reactor Research (IGORR)

Centre de Congrès, Lyon, France
11– 15 March 2007

Organised by the
European Nuclear Society (ENS)

and

IGORR: International Group on Research Reactors

in co-operation with the
International Atomic Energy Agency (IAEA)

© 2007
European Nuclear Society
Rue de la Loi 57
1040 Brussels, Belgium
Phone + 32 2 505 30 54
Fax +32 2 502 39 02
E-mail ens@euronuclear.org
Internet www.euronuclear.org

These transactions contain all contributions submitted by 9 March 2007.

The content of contributions published in this book reflects solely the opinions of the authors concerned. The European Nuclear Society is not responsible for details published and the accuracy of data presented.

Poster Session

Poster Session

THE NEW AREA RADIATION MONITORING SYSTEM OF THE TRIGA NUCLEAR RESEARCH REACTOR FACILITY OF THE UNIVERSITY OF PAVIA

G. MAGROTTI, D.ALLONI, A. BORIO DI TIGLIOLE, M. CAGNAZZO, M.CONIGLIO, S. MANERA, M. PRATA, A. SALVINI, G. SCIAN

Laboratorio Energia Nucleare Applicata – LENA - University of Pavia
Via Aselli 41, 27100 Pavia - Italy

The area radiation monitoring system of the TRIGA nuclear research reactor facility of the University of Pavia has been renewed after 30 years of operation. The new system is based on a commercial micro-computer and an home-made software developed on Lab-View platform. The system collects the data sampled by six β-γ dose-rate proportional counters, a free-air ionization chamber and a weather station through a serial data bus line RS232. Collected data are displayed through a desktop PC in the reactor control room and are also accessible, for a restricted number of users, through internet using the TCP/IP protocol. The software allows the operator to access the data, to modify parameters and perform tests remotely, by means of any common web browser.
For an improved safety level, data are stored both in the micro-computer and in the desktop PC, both accessible remotely. The system is provided by output relays that activate automatically the nuclear alarm detection system of the facility when pre-set levels of environmental radiation dose-rate are exceeded. A watchdog, integrated into the micro-computer, tests the whole data acquisition system regularly in order to prevent possible software or hardware failures.

1. Introduction

The purpose of the new radiation monitoring system is to perform a continuous acquisition of the radiation level throughout the facility. According with the requirements of the Radiation Protection Officer of the reactor facility, the following parameters are constantly monitored:

- β-γ Dose-rate inside the reactor room and inside the air outlet chimney
- β-γ Dose-rate of the water of the reactor primary cooling circuit
- Activity of the air particulate inside the reactor room
- Environmental data collected inside and outside the building (i.e. wind speed and direction, pressure, inside and outside temperatures)

2. General description

The system is made of a network of different instruments coupled, trough a serial bus line, with a data acquisition station.
The detection system is configured as follows (see Fig.1):

- three Berthold LB111 proportional counters equipped with two β-γ dose-rate probes each, placed as follows: four probes mounted inside the reactor room at each cardinal point position and at the same level, one probe mounted on the reactor room ceiling, exactly over the reactor open tank and one probe inside the air outlet chimney;
- one proportional counter Berthold LB111 with one β-γ dose-rate probe for the monitoring of the water of the reactor primary cooling circuit;
- a free air Ionization Chamber for the monitoring of the activity of the air particulate inside the reactor room;
- one weather station Peet Brothers placed on the roof of the building, connected to Peet Brothers U2000 instrument (placed in the reactor control room) for the acquisition of environmental data;
- one National Instruments Compact Field Point (NI CFP 2020), placed in the reactor control room, for radiation monitoring data acquisition and analysis;

- one personal computer (Host PC), placed in the reactor control room, for radiation monitoring data display (throughout a graphic interface) and storage.

In order to get the best reliability and to ensure a continuous operation, the system power supply is served by an Uninterruptible Power Supply (UPS). When a power failure or abnormality occurs, the UPS will effectively switch from utility power to its own power source instantaneously.

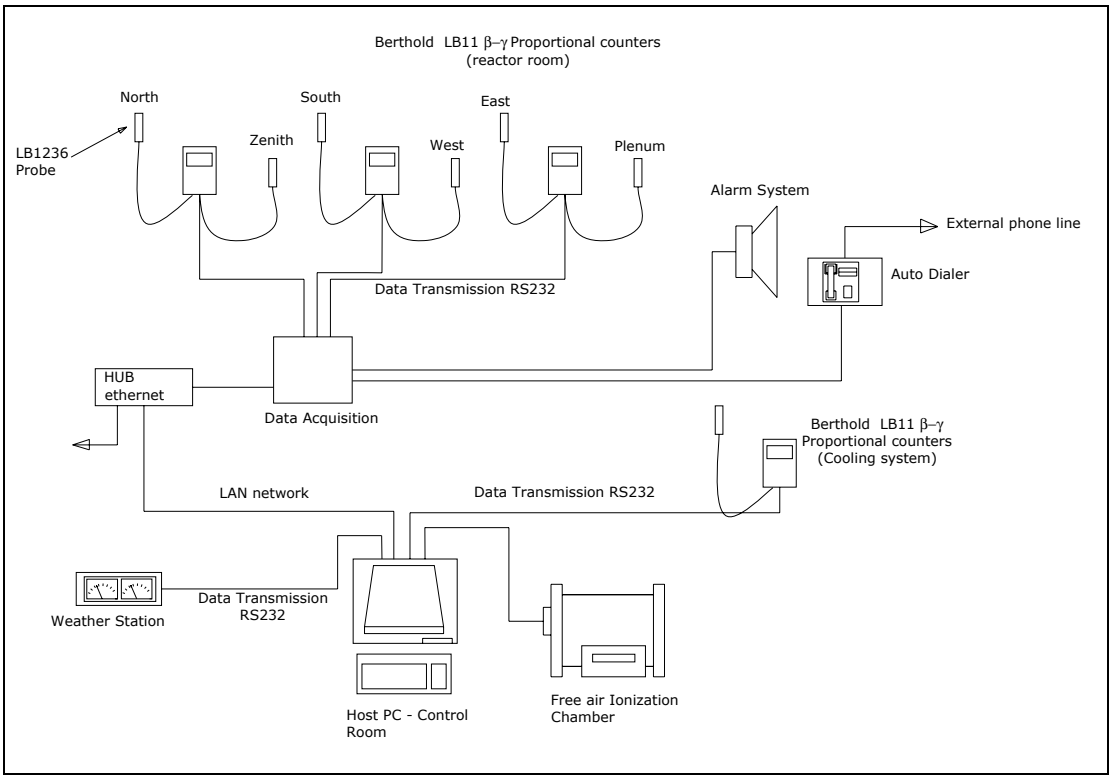

Fig. 1 – System lay-out

3. Instruments description

Berthold LB111 Micro-Gamma proportional counter

The LB111 Micro Gamma is a versatile instrument to measure local doses and doserates in one or two channels. It can be software-programmed for manifold applications, and contains all facilities for data storage and data transmission. The instrument can be employed as a stand-alone system with local result and alarm indication. Several LB111 systems may be connected to one central data station inside one premise via a local network with leased line, e.g. RS232 or RS485 bus system.

National Instruments Compact Field Point (CFP) data acquisition system

National Instruments Compact Field Point® is a programmable automation controller composed of I/O modules and intelligent communication interface. Compact Field Point® network communication interfaces and automatically publishes measurements with an Ethernet network. Is it possible to access I/O points nearby or miles away on the network using the same simple read/write software framework. The instrument can acquire data from serial lines RS232, RS485 or from analog I/O banks. It can also operate a series of output relays trough an output module.

4. Data acquisition and analysis software

Data acquisition and storage is performed in two different ways:

- the six proportional counters that monitor the dose-rate inside the reactor room transmit the data to the acquisition system CFP, via a RS232 serial line. The CFP decodes and stores data on a local flash memory and then re-transmit them, via Ethernet, to the Host PC for the visualization and for the backup storage on a local hard disk. CFP can activate output relays for the alarm system intervention;

- all the other parameters monitored (i.e. weather data, primary reactor cooling circuit water activity, air particulate activity) are acquired, processed, displayed and stored directly by the Host PC.

The home-made software developed on LabVIEW platform operate contemporary on two different levels, sharing data but maintaining a physical independence: a part of the software is resident on the CFP and is dedicated to the acquisition of the dose-rate monitoring data inside the reactor room, while the other part of the software is resident on the Host PC and performs the acquisition of all the other parameters.

This kind of configuration was chosen in order to grant redundancy and better reliability for the acquisition and storage of dose-rate monitoring data inside the reactor room.
The program installed on the CFP contains an automatic start-up file and provides the following tasks:

- acquire the dose-rate monitoring data inside the reactor room
- decode the transfer patterns
- compare the dose-rate with pre-set alarm thresholds
- operate the output relays
- transmit data to the Host PC via TCP/IP protocol
- storage data every 60 s on an removable flash memory

The tasks chain, except for the storage on the flash memory, has an execution time of 2 seconds. In the case of software failure, the program automatically saves an error report with the position of the failure in the execution chain.
In order to get an accurate data log, data from CFP are saved also on the Host PC every 60 seconds.

The software running on the Host PC collects, saves, and displays all the data, those coming from the CFP and the others acquired directly. The program code has been split in several “while loop”, one for each operation required, with an execution time of 1 second. The PC displays data both as numeric values and graphs (i.e. bar graphs, gauges, history charts) as shown in Fig.2.

Fig. 2- Host PC Front panel

From the main menu is possible to access the history charts of all data stored as shown in Fig.4. Is it also possible to access the program remotely via TCP/IP, using any common web browser. For security reasons though, only authorized clients can access the program and the data files.

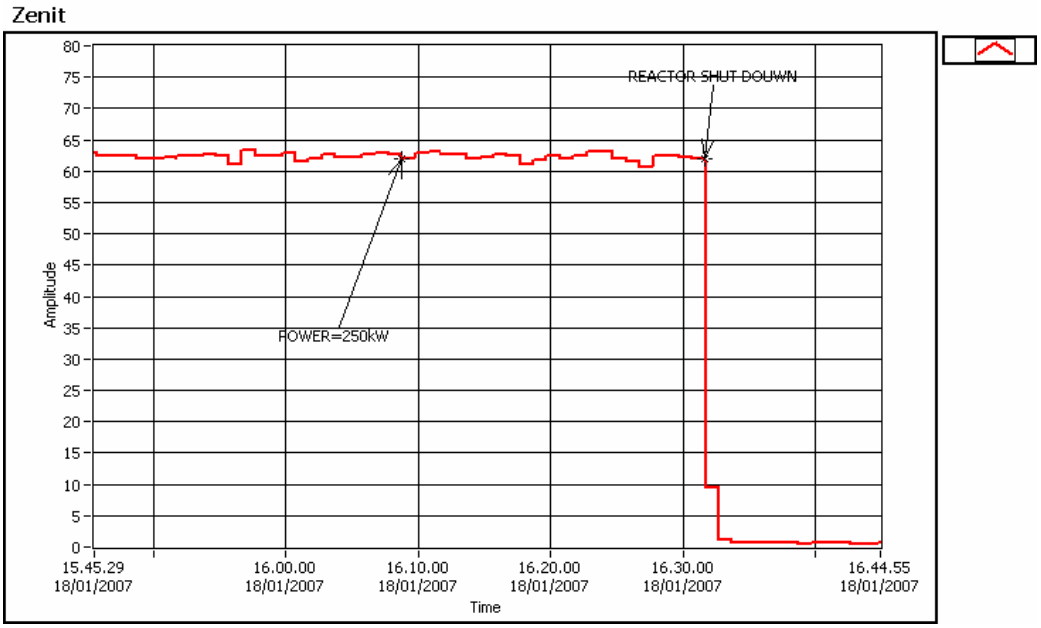

Fig.4 – Historical dose-rate data (Amplitude = µSv/h)

The system recognizes and operate for two different pre-set levels of alarms:

- *Investigation Level Alarm*: as soon as the measured dose-rate in one of the counters reaches the first pre-set alarm threshold, both acoustical and light signals on the local counter (through a yellow signal lamp and a buzzer – see Fig.5) and on the front panel of the Host PC (buzzer and a blinking yellow led) are activated;
- *Intervention Level Alarm*: as soon as the measured dose-rate in one of the counters reaches the second pre-set alarm threshold, both acoustical and light signals on the local counter (through a red signal lamp and a buzzer– see Fig.5) and on the front panel of the Host PC (buzzer and a blinking red led) are activated. In this case CFP operates two output relays that activate the general alarm horn of the facility and the telephone dialler respectively. The dialler alert on the mobile phones the emergency personnel by means of a pre-registered message.

The alarm-activation channels do not depend on the PC. Radiation counters failures or program crashes are promptly notified to the personnel on call via the auto-dialler
CFP has also a watchdog which is a computer hardware timing device that triggers a system reset if the main program, due to some fault condition, such as a hang, neglects to regularly service the watchdog. The watchdog goal is to bring the system back from the hung state into normal operation. If an error occurs, the watchdog activates the Intervention Level Alarm relay.

Fig.5 – LB111 Proportional Counter

5. Data communication

Both CFP and Host PC access the instruments, via the bus line, to request data or to set parameters. Data transfer is always initiated and executed by the Host PC or by the CFP and the request flag is stored in the battery-buffered memory of the instruments with the FIFO content. Every instrument has its own COM port, in order to avoid possible failures of the whole system due to a problem on the communication line. The communication protocol is the RS232 standard, and, after several test, the following parameters have been set in order to get the best performance:

Transfer mode asynchronous	
Full duplex	
ASCII type	
Start bit	1
Stop bit	1
Parity	No
Baudrate	1200
Handshaking	RTS/CTS
Signal GND	

Tab. 1- Serial interface RS232 parameters setting

The wind direction and speed are displayed on a polar graph collecting data from the last 12 hours. This representation is very useful to follow diffusion of a radioactive cloud in the case of a nuclear emergency.
Monthly, a file with the report of the average temperatures and atmospheric pressures of every single day is sent by e-mails to the Health Physics Service of the reactor.
Whenever the CFP or Host PC memories usage reaches the 80% of its capacity, the program sends an alert e-mail to the maintenance manager of the system.

6. Conclusion

The new radiation monitoring system has been calibrated and tested for three months at the reactor facility of the University of Pavia showing to be very reliable and accurate. The new system will be implemented as substitute of the old one within a couple of months.

7. References

- National Instruments Compact Field Point (CFP) 2020 User Manual
- Berthold LB111 Micro-Gamma proportional counter Operating Manual
- LabVIEW Real-Time Module 8.0 Manuals

EVALUATION OF THE FEASIBILITY OF APPLYING CERMET FUEL PINS ON BASIS OF URANIUM ENRICHED UP TO 20% ^{235}U TO UPRATED POWER RESEARCH REACTORS

Yu.D. BARANAEV, A.P. GLEBOW, A.D. KARPIN, V.V. POPOV
SSC RF-IPPE (249033, Bondarenko Sq. 1, Obninsk, Russia)

ABSTRACT

The paper deals with the feasibility of employing fuel pins with a cermet fiel composition (UO_2 particulates in an Al-based alloy) clad with the zirconium-based Zr+l%Nb alloy to elevated power research reactors.

The fuel pin production process enables to place uranium dioxide particulates, up to 65 % by volume, into small diameter claddings and to attain in fuel composition the volume densities up to 6.4 g U/cm^3 of uranium. The impregnation of the charged UO_2 particulates with the liquid matrix material in the subsequent course of fuel pin fabrication enables to ensure high thermal conductivity of the cermet fuel composition and zero thermal resistance at the fuel-cladding interface

The computations (made, by way of example, with reference to the IR-8 research reactor) have shown that the replacement of tubular fuel elements with high-enriched uranium, by fuel pins whose cermet fuel is enriched not more than to 20 % is possible in principle, with the main thermal-hydraulics and neutronics characteristics of the reactor being conserved.

1. Introduction

Russian water-water research reactors (RR) are operated now with use of tubular cermet fuel elements with a cermet fuel (UO_2 in an aluminium-alloy matrix), fabricated by means of the extrusion technique. Alongside with the extended energy conduction surface as an advantage, these tubular fuel elements possess several disadvantages:

- diversity as to the shapes and sizes of fuel elements;
- spatial unevenness of energy release across the section of a fuel assembly (FA) and a high unevenness of longitudinal distribution of energy;
- the extrusion method of fuel element fabrication limits the volume content of UO_2 fuel particulates to 29 %, and the volume concentration of uranium to 2.5 gU/cm^3 [1]. This limitation requires high enrichment with uranium, coming up to 90 %.

The above mentioned disadvantages can be eliminated in case of the transfer from tubular elements to fuel pins. With that end in view it is essential to ensure the extended energy conduction surface; it can be made at the expense of lowering the fuel pin diameter.

2. Cermet fuel pins

The process of fabricating cermet fuel pins developed in Russia [2] is similar to that of fabricating fuel pins for the Bilibino NPP that had been mastered at the Elektrostal Engineering Plant, Russia.

In a few words, the process of fabricating such a fuel pin looks as follows: a cladding made of the zirconium-based (Zr+1%Nb) alloy is filled (up to 65% of its volume) with UO_2 particulates, after which the charge is impregnated with a liquid aluminium-based alloy as the matrix material (whose volume fraction is 35% or somewhat higher). This process ensures the metallurgical bondage between the fuel and its cladding. The measured values of thermal resistance at the fuel-cladding interface, R_k, are of an order of $10^{-6} \div 10^{-5}$ m^2·degree/W.

The fabrication process like this guarantees the metallurgical bondage between the fuel and its cladding. Moreover, the examination carried out by far has shown that the fuel of this kind possesses sufficiently high thermal conductivity, as can be seen in Table 1.

Table 1. The values of the thermal conductivity coefficients of cermet fuel (UO_2+aluminium-based alloy) as a function of temperature

Temperature, ^oC	200	300	400	500	Percent composition of cermet fuel
Thermal conductivity coefficient, λ, W/m·degree	37,4	35,9	34,3	32,8	60 vol% UO_2 + aluminium-based alloy

This fabrication process has been mastered for cermet fuel pins 5 mm in diameter whose fuel composition can contain up to 6.4 g uranium per 1 cm^3. It is expected that the enrichment of their fuel with ^{235}U, X_5, can be lowered to ≤ 20 %.
Nevertheless, the transfer from the present tubular fuel elements to the suggested fuel pins will bring about a certain reduction in the specific heat removal surface, and a certain increase in the loading of ^{235}U, which will result in some changes of physical and thermo-hydraulic characteristics of a reactor. The question whether such changes are acceptable is being studied now, by way of example, with reference to the IR-8 research reactor (Kurchatov Institute, Moscow), where a rather considerable extension of the heat removal surface per volume unit of the reactor core, $F_{h.r.}/V_{core}$=525 m^2/m^3, has already been achieved. With reference to the IR-8 reactor we have carried out a comparative computational analysis of physical and thermo-hydraulic characteristics as applied to the transfer from tubular fuel elements to fuel pins. However, it is yet of a preliminary character as it has been carried out without taking into account both the control and protection system of specifically that reactor, and its structural distinctions.

3. Results of thermo-hydraulic and physical computations

Table 2 presents thermo-hydraulic characteristics of a standard FA of the IR-8 reactor, and a FA with fuel pins.

Table 2

Characteristics and units	Values	
Type of fuel elements	Standard, tubular	Pin type, ∅ 5 mm
Number of fuel elements in a FA, pcs.	8	121
Spacing of FAs (in a square lattice), mm	71.5	71.5
Spacing of fuel elements in a square lattice, mm	–	6.5
Surface of heat removal in a FA, m^2	1.45	1.1
Open flow area in a FA, m^2	0.0030	0.00274
Maximum thermal load, kW/m^2	740	976
Temperature drop from a fuel element to water, ^oC	22	24.4
Maximum temperature of a fuel element surface, ^oC	72	74.4
Thermal load ruling out the possibility of surface boiling of water, not more than, kW/m^2	1746	2072
Marginal load capacity up to surface boiling	2.36	2.12

It follows from the data of Table 2 that in the view of thermo-hydraulic characteristics the version of a FA with 121 fuel pins for utilization in the IR-8 reactor in exchange for its standard FAs seems to be accessible.
The comparative physical computations have been carried out both for a standard FA of the IR-8 reactor with eight tubular fuel elements and for a FA with 121 fuel pins. The fuel pins were considered as loaded with a cermet fuel (30 %UO_2+70 vol%Al) on basis of uranium enriched with $X_5 \approx 21$ wt% of ^{235}U. The results of these computations are presented in Figure 1 and in Table 3.

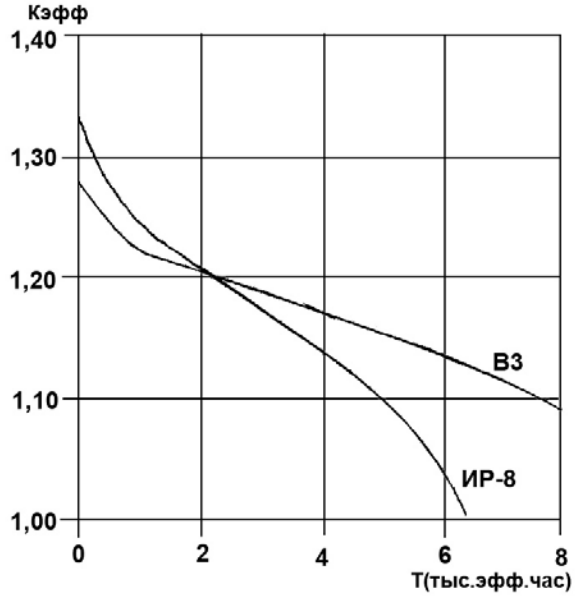

Fig. 1. The temperature dependence of K_{eff} in cases of tubular and pin fuel elements as a function of durance of life (in thousands of operational hours)

Table 3. Results of reactor physics computations relating to the versions of the reactor core considered

Variant	Number of FA, pcs	Number of fuel elements per FA, pcs	X_5, %; composition of fuel	$K_{eff}(0)$	T, eff days	Φ^{max}_{core} (10^{14}n/cm^2·s)	
						thermal, E_n<1eV	fast, E_n>0,1MeV
Pin type fuel elements, ∅ 5 mm (*B3*)	16	121	21 30%UO_2+70%Al	1,2766	370	0,93	3,66
Standard FA of the IR-8 reactor	16	8	90 U-Al	1,3315	280	1,7	3,31

As can be seen in the figure and in the table, the values of $K_{eff}(0)$ for fuel pins in the beginning of the life cycle are somewhat lower than for the standard fuel elements of the IR-8 reactor. But owing to a greater load of ^{235}U and a contribution from plutonium into the fission of nuclei the slope of curves becomes more gentle, and the core life time turns out to be longer.
If the standard life time of the IR-8 reactor is regarded as acceptable also for cermet fuel pins, and the volume fraction of UO_2 particulates in cermet fuel is increased up to 60÷65%, it will become possible to reduce the degree of enrichment with ^{235}U even to values of ≤15 %.

4. On the efficiency of pin-type fuel elements

Computations of the stressed-strained state and efficiency of a cermet fuel pin under the operating conditions of the IR-8 reactor have been also carried out. The following admissions have been made for these computations:

Cladding material	(Zr+1%Nb) alloy
Enrichment with ^{235}U in UO_2	20% of ^{235}U
Volume fraction of UO_2 in the fuel composition	60% UO_2 + 40% Al
Burnup of uranium at the end of life (EOL), %	80% ^{235}U, or 16% h.a.
Swelling rate of UO_2, ΔV/V, up to B ≈ 3% h.a.	0
at B ≥ 3 % h.a.	0,59 % per 1 % h.a.
Core life time T, eff. hours	$6 \cdot 10^3$

These computations have shown that the swelling particulates of UO_2 cause the strain of the fuel pin cladding at a rate of $\dot{\varepsilon}_\theta = 1{,}95 \cdot 10^{-6}$ 1/h. Such a rate of loading of the cladding is compensated by its irradiation creep, see [4], at a stress of $\sigma_\theta \approx 200$ MPa, which is considerably less than the yield stress of the (Zr+1%Nb) alloy ($\sigma_T \geq 450$ MPa at $\Phi \approx 8 \cdot 10^{21}$ n/cm^2, E > 0.1 MeV). At the end of life (EOL) the cladding will increase its diameter by $\Delta d \approx 0.04$ mm, which will have practically no influence on the thermo-hydraulic characteristics of the reactor core.

5. Conclusion

As has been shown, it is possible in principle to replace tubular fuel elements with HEU in Russian research reactors by fuel pins with cermet fuel whose uranium is enriched less than to 20%. At that the thermo-hydraulic and neutronics characteristics of reactors, as well as the performance *of* its fuel elements, will remain acceptable.

The use of cermet fuel pins in research reactors will enable:

- to replace a broad spectrum of tubular fuel elements, as to their shapes and dimensions, by the unified fuel pin of the same diameter;
- to perform a transfer from the fuel elements on basis of HEU to that on basis of LEU (with less than 20% ^{235}U);
- to use the fuel elements with and without gadolinia as a burnable poison in their fuel composition to compensate the most part of their initial reactivity excess, which will enable to simplify the control and protection system, to improve the economy and the safety of the reactor.

6. References

[1] G.A.Sarakhova, Yu.A.Stetsky, V.B.Suprun. Development of high density fuel for research reactors IAEA-TECDOC-970/ Studies on fuels with low fission gas release, October 1997.

[2] V.Troyanov, V.Popov, Yu.Baranaev. Cermet fuel in a light water reactor: a possible way to improve safety. Part I. Fabrication and characterization. Progress in Nuclear Energy, Vol.38. №3-4, pp.267-270. 2001.

[3] Ю.Д.Баранаев и др. Оценка возможности использования в исследовательских реакторах ИР-8, ВВР-Ми ВВР-Ц стержневых твэлов с обогащением урана до 21%. Препринт ГНЦ РФ-ФЭИ, №ФЭИ-2600, Обнинск, 1997 (The evaluation of the feasibility of applying fuel pins with uranium enriched to 21% in the research reactors IR-8, WWR-Mi and WWR-*Ts*. A preprint of the SSC RF-IPPE No. ФЭИ-2600, Obninsk, 1997, in Russian).

[4] M.G.Bulkanov *et al*. Study of in-reactor creep in the alloys employed as structural materials for research reactor core components and fuel pins. Transactions of the 6th. International Topical Meeting on Research Reactor Fuel Management March 17 to 20, 2002, Ghent, Belgium.

SOURCE OF RADIONUCLIDES IN PRIMARY CIRCUIT WATER OF LVR-15 REACTOR

L. VIERERBL, Z. LAHODOVA, V. KLUPAK, M. MAREK, A. VOLJANSKIJ
Nuclear Research Institute Rez plc
250 68 Rez, Czech Republic

ABSTRACT

The early detection of a damaged fuel assembly in reactor core is one of the most important aspects for safety operation of the reactor and radiation protection of the research reactor staff. The indication of damaged fuel assembly can be based on evaluation of the primary circuit water activity. Radionuclides in the water are produced by activation of stable nuclides and by fission of fissile nuclides, mainly ^{235}U. From comparison of theoretical results made by ORIGEN 2.1 code and measured values of volume activities of fission products and ^{239}Np (activation product of ^{238}U) the enrichment of the irradiated uranium has been estimated in LVR-15 research reactor. Finally, on the basis of the known enrichment it can be concluded if the source of fission products is mainly natural uranium (e.g. from demineralized water) or uranium from fuel assemblies (contamination of fuel cladding or damage of fuel assembly).

1. Introduction

The LVR-15 reactor is a light water research type reactor, which is situated in Nuclear Research Institute, Rez near Prague. At present the IRT-2M fuel of Russian production with enrichment of 36 % is used. In the reactor core there are usually from 28 to 32 fuel assemblies with the total mass about 5 kg of ^{235}U. Reactor is cooled by demineralized water. The maximum thermal power is 10 MW and the reactor is operated in 21-days irradiation cycles, with 8 to 10 cycles per year.

The indication of damaged fuel assembly can be made e.g. from gas effluents. This paper deals with the method based on the primary circuit water activity measurement. The measurement using gamma spectrometry method has been performed regularly (weekly) since 1996, measurement of actinides using alpha spectrometry method in evaporated samples of primary circuit water since 2005.

2. Methods of measurement

The samples of primary circuit water are taken every week (on Thursday) and the spectrometric measurement is made 4 days later (on Monday).

Originally the Marinelli beakers were used for the gamma activity measurement. Since 1998 the same 0,5 l PET bottle has been used both for taking of the sample and measurement (no trapping of radioisotopes on the walls of the bottle used for taking of the sample and on the walls of the Marinelli beaker, minimum handling with the radioactive water).

A gamma spectrometric assembly (Canberra) with an HPGe detector with relative efficiency of 18 % and FWHM=1.8 keV for energy of 1332 keV is used for gamma activity measurements (Fig. 1). The detector is placed in a shielding box with 5 cm thick lead walls. For calibration special radionuclide standards of 0,5 l bottle has been used. The minimum detectable volume activity is 10 Bq/l for ^{137}Cs and measuring time of 3600 s, which is sufficient for the measurements. The analysis is made for the library of about 100 radionuclides but only 26 radionuclides is used for standard evaluation.

For alpha measurement the water sample is evaporated on cup made from Al foil. The same water sample previously used for gamma measurement is used for evaporation (Fig. 2). An alpha spectrometric assembly (Canberra) with a PIPS (Passivated Implanted Planar Silicon) detector with FWHM = 20 keV for energy of 5486 keV is used for alpha activity measurements. Each sample is measured in vacuum chamber for 3 days.

Fig. 1. Gamma activity measurement

Fig. 2. Evaporation of water sample

3. Time dependence of fission product activities

In Fig. 3 the time dependence of ^{131}I and ^{137}Cs volume activity is given. Increased values in 1996 are due to a damaged fuel assembly in the reactor core, low values in 1996 due to reactor shutdown and cleaning during a maintenance period. Missing data in 2002 are related to flood near the reactor building.

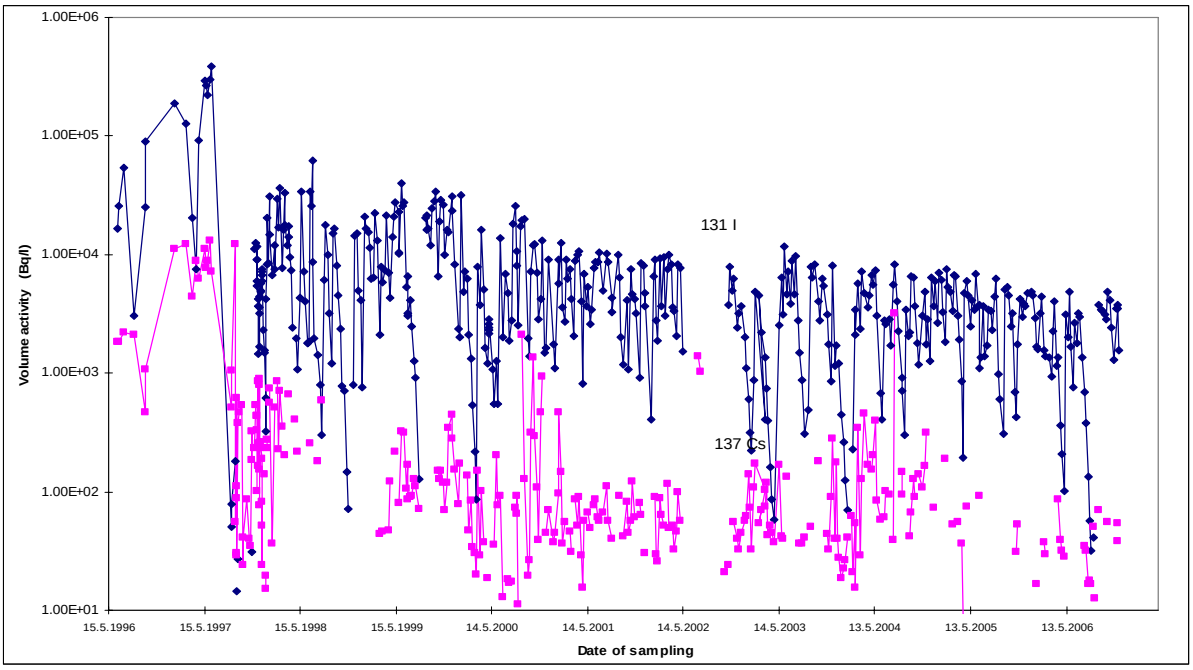

Fig. 3. Time dependence of volume activity of ^{131}I and ^{137}Cs in primary circuit water

4. Analysis of radionuclide sources

In Table 1 the example of volume activities and volume mass of source element values primary circuit water sample is given. The sample was taken on 28. 4. 2005 during the reactor cycle started at 13. 4. 2005.

Table 1. The example of volume activities and volume mass of source element values

Radionuclide	Half life	Reaction	Volume activity	Volume mass of source element (^{235}U or ^{238}U)
	(days)		(Bq/l)	(μg/l)
^{95}Zr	64.03	^{235}U(n,f)^{95}Zr	1.99E+03	0.346
^{95}Nb	35.15	^{235}U(n,f)^{95}Nb	3.17E+03	0.761
^{99}Mo	2.78	^{235}U(n,f)^{99}Mo	5.57E+03	0.468
^{103}Ru	39.5	^{235}U(n,f)^{103}Ru	6.19E+02	0.183
^{131}I	8.05	^{235}U(n,f)^{131}I	5.85E+03	1.339
^{132}Te	3.24	^{235}U(n,f)^{132}Te	7.31E+02	0.088
^{133}I	0.867	^{235}U(n,f)^{133}I	2.62E+04	1.92
^{133}Xe	5.30	^{235}U(n,f)^{133}Xe	5.63E+03	0.492
^{137}Cs	11000	^{235}U(n,f)^{137}Cs	7.45E+01	1.268
^{140}Ba	12.75	^{235}U(n,f)^{140}Ba	9.56E+03	1.162
^{140}La	1.678	^{235}U(n,f)^{140}La	1.57E+04	2.07
^{141}Ce	32.5	^{235}U(n,f)^{141}Ce	1.78E+04	2.706
^{143}Ce	1.375	^{235}U(n,f)^{143}Ce	1.63E+04	1.358
^{144}Ce	284.3	^{235}U(n,f)^{144}Ce	1.04E+03	0.601
^{24}Na	0.623	^{23}Na(n,γ)^{24}Na	4.75E+06	
^{41}Ar	0.076	^{40}Ar(n,γ)^{41}Ar	4.33E+05	
^{46}Sc	83.9	^{45}Sc(n,γ)^{46}Sc	2.85E+04	
^{51}Cr	27.7	^{50}Cr(n,γ)^{51}Cr	8.56E+05	
^{54}Mn	312.3	^{54}Fe(n,p)^{54}Mn	4.54E+03	
^{56}Mn	0.108	^{55}Mn(n,γ)^{56}Mn	1.26E+05	
^{58}Co	70.86	^{58}Ni(n,p)^{58}Co	2.63E+03	
^{59}Fe	44.50	^{58}Fe(n,γ)^{59}Fe	2.96E+04	
^{60}Co	1921	^{59}Co(n,γ)^{60}Co	3.39E+04	
^{65}Zn	243.9	^{64}Zn(n,γ)^{65}Zn	1.42E+04	
^{110m}Ag	255	^{109}Ag(n,γ)^{110m}Ag	3.44E+02	
^{113}Sn	115.1	^{112Sn}(n,γ)^{113}Sn	1.14E+03	
^{122}Sb	2.8	^{121}Sb(n,γ)^{122}Sb	3.73E+04	
^{124}Sb	60.2	^{123}Sb(n,γ)^{124}Sb	2.11E+04	
^{125}Sb	1007	^{124}Sn(n,γ)^{125}Sn(β$^-$)^{125}Sb	1.87E+02	
^{152}Eu	4944	^{151}Eu(n,γ)^{152}Eu	4.44E+02	
^{181}Hf	42.39	^{180}Hf(n,γ)^{181}Hf	9.50E+02	
^{187}W	0.988	^{186}W(n,γ)^{186}W	7.70E+04	
^{239}Np	2.36	^{238}U(n,γ)^{239}U(β$^-$)^{239}Np	8.82E+03	1.703

The theoretical values of volume mass of source nuclides ^{235}U and ^{238}U were calculated from individual radionuclide activities by ORIGEN 2.1 code. The calculation was made for the following conditions: the effective fluence rate is 2.1×10^{16} m^{-2}s^{-1} and all fission products and ^{239}Np are released into the water.

The mean values of volume mass of ^{235}U and ^{238}U under these conditions calculated for 3 samples are 1.09 μg/l and 1.70 μg/l respectively, which correspond to enrichment of 39 %.

To estimate the total mass of ^{235}U in primary circuit water with volume of 40 m^3, two cases can be considered:

a) All this ^{235}U is homogeneously dissolved in primary circuit water (effective fluence rate of $2.1x10^{16}$ $m^{-2}s^{-1}$). For this case the total mass would be 44 mg.
b) All this ^{235}U is situated in the reactor core (effective fluence rate of $1.7x10^{18}$ $m^{-2}s^{-1}$) and all fission products are dissolved in primary circuit water. For this case the total mass would be 0.54 mg.

5. Alpha activity measurement

Alpha measurement is performed for shorter time, since 2005. Example of the results is in the Table 2.

Table 2. The example of alpha radionuclide activities in the sample taken on 5. 11. 2005

Radionuclide	Volume Activity (Bq/l)	Volume activity error (%)
^{238}Pu	0.034	10.95
^{239}Pu	0.072	5.41
^{240}Pu	0.074	5.3
^{241}Am	0.05	38.32
^{242}Cm	0.026	18.99
^{244}Cm	0.012	13.83

6. Conclusion

During 10 years of measurement, the activities of fission products in primary circuit water have been decreasing, in average. From comparison of theoretical results and measured values of volume activities of fission products and ^{239}Np the enrichment of the irradiated uranium have been estimated. The resulted 39 % enrichment has high uncertainty due to complicated chemical and physical processes inside of the reactor. Despite of this uncertainty (estimated of factor 2 to 5) the enrichment is much closer to value of fuel enrichment (36 %) than for natural Uranium (0.72 %). The origin of the uranium can be contamination of fuel cladding with uranium or residuum from the damage of fuel assembly in 1996. The presence of alpha radionuclides is probably also connected with this event.

Acknowledgments

The work was supported by Research Project MSM 267 224 4501 of Research Centre of NRI Rez Ltd.

DEVELOPMENT OF INTEGRATED MANAGEMENT SYSTEM FOR THE RESEARCH REACTOR IN SOFIA

A. S. STOYANOVA, K. T. ILIEVA

Institute for Nuclear Research and Nuclear Energy,
Bulgarian Academy of Sciences
Tzarigradsko Shossee 72, 1784 Sofia, Bulgaria

ABSTRACT

The main purpose in establishment of Integrated Management System (IMS) is to guarantee safety operation of the nuclear facilities as well as to increase their exploitation effectiveness. To ensure the safety operation of the nuclear facilities the Bulgarian Nuclear Regulatory Agency has created requirements and norms to prevent potential nuclear incidents, overdose irradiation or terrorist attacks opportunities. The IMS of the Institute for Nuclear Research and Nuclear Energy has been developed in a way to create an environment which to guarantee the ways and means for: quality management according with ISO 9001:2000, environmental management according with ISO 14001:2004, management of safety requirements of the Bulgarian Nuclear Regulatory Agency, security and physical protection, management of the safe and health working conditions for the employees. The IMS is based on the concepts recommended by the IAEA: the entirety of work can be structured and interpreted as a set of interacting processes that can be planned, performed, measured, assessed and improved, and, those performing assessing work, all contribute in achieving quality and ensuring safety. The IMS has been developed in the way to be continuously refreshable and additive. The IMS will be added with new instructions, procedures and others, which will correspond to new activities arising during the reactor reconstruction. The IMS was developed on the base of state-of-the-art software ARIS in the way to achieve ease in communication, visualization, possibilities for assessment and continues improvement of the IMS.

I. Introduction

The Institute for Nuclear Research and Nuclear Energy (INRNE), Bulgarian Academy of Science, with its Research Reactor IRT is the biggest complex in Republic of Bulgaria for conducting research in the field of nuclear science, nuclear technology and energy and in the field of the monitoring of the radioactive influence on the environment.

The INRNE is the host and an operator of this institutes research reactor complex which is situated in Sofia city, and it is responsible for reactor systems maintenance and controls the permanently shutdown Research Reactor. INRNE is responsible also for the reconstruction activities, which include:

- Planning and preparation for partial dismantling of the Research Reactor equipment;
- Supply of equipment for the IRT Reconstruction;
- Planning of activities and responsibility for reactor modernization;
- Spent fuel control and management;
- IRT radiation monitoring for all implemented activities;
- Radioactive waste (RAW) management and control, for the RAW generated during the reconstruction process.

An Integrated Management System has been elaborated on ISO 9001:2000 requirements for quality management [1], ISO 14001:2004 for environmental management [2], and safety requirements of the Bulgarian Nuclear Regulatory Agency [3], governmental requirements for occupational health and safety and security. The IMS application guarantees the safety of activities as well as reduces of the radiation influence on the environment within the governmental norms. It helps to achieve maximal effectiveness and quality of the performed activities.

II. Processes

The processes, going along with various activities performed on the institute's Research Reactor are described in so called procedures. This procedures are developed in the way to give you an opportunity for simple process control following the Deming's cycle trough plan, do, check, action stages. [4] For each activity there is a responsible personal, delegated with peculiar obligations and competence.
The job instructions for each activity have been developed and different formularies to inscribe the results are applied. The regulatory body can control safety requirements performance according to these records, and there are documents in case of audit, or to give evidence to civil interest.
Here are shown some of most important and specific processes and procedures for our reactor as: "The IRT nuclear and irradiation safety insurance"; "IRT Research Reactor reconstruction management"; "The radiation monitoring insurance on the Nuclear Scientific and Experimental Centre (NSEC) site"; "Radioactive waste management"; "Preparation of documentation for licence and permissions".
For the process "The IRT nuclear and irradiation safety insurance" corresponded to procedure with instructions attached to, for example "Instruction for distillate water full up in reactor pool and water pool spent nuclear fuel (SNF) storage", "Instruction for the water technology control in water pool spent nuclear storage", "Instruction for activity on duty for the mechanic when IRT special sewage is used" etc. The performance of these activities is documented in the records, which proved the IRT safety assurance.
Other basic process is "The Research Reactor reconstruction management". The realisation of that process is graphically shown on fig. 1 and it is developed in following basic procedures:

- "Management of "Investigations, analysis and design of the Research Reactor with 200 kW power"";
- "The reactor equipment partial dismantling management";
- "The IRT reconstruction work project implementation management";

All processes, that are carried out on the NSEC site are accompanied with permanent radiation control and monitoring. These activities are described in the procedures "Securing the radiation monitoring on NSEC site" and "Providing safety radiation conditions for the personal, working with radioactivity sources, on the NSEC site". The monitoring programs and instructions strict implementation is documented by the records in appropriate formularies.
The „Radioactive waste management" process includes: RAW generation, collecting, sorting, minimization, and storage up to final transportation from the NSEC site. These activities control is realized according to Bulgarian legislation requirements, which are reflected in the procedure "RAW management". The responsible for RAW person makes the records, which give an account about the RAW quantity and the movement.
To make easier the realization of the system process as well as to evaluate it and to apply continuing improvement principle on IMS (in agreement with ISO standards) the ARIS software has been used. [5]

III. Results

From general point of view the good practice is the approach were we plane and conduct training to achieve qualification level. To perform this we can conduct training courses not only concerning nuclear technology and energy knowledge but conducting seminars on IMS also. The necessity, to conduct education courses, is documented in the form – "Training Application". After the end of the education course, the trained person has to write down report.
At daily work we ran into difficulties, connected with establishment and documentation of the suggestions for improvements in separate processes. That's why periodically we are refreshing our courses by the ISO standards requirements.

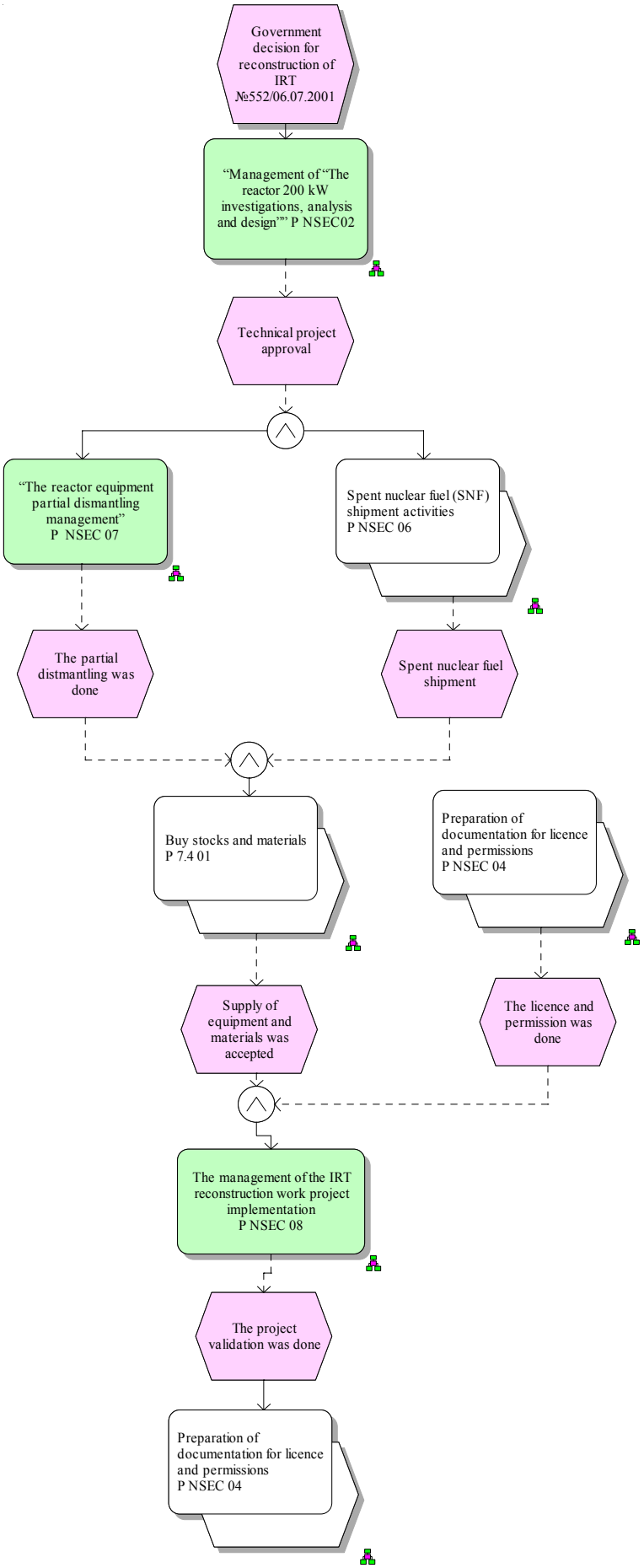

Fig.1. The process chart "The IRT Research Reactor reconstruction management"

The INRNE management policy is directed to guarantee high quality developments implementation, which are in agreement with modern world trends of continuously refreshing knowledge, of long standing experience and cooperation with leading European and International institutions. INRNE have a purpose to satisfy the community needs for development and maintenance of the nuclear science, to create necessary knowledge and skills for development of applied methods and research in the area of nuclear technology medical physics and nuclear industry.

IV. Conclusion

The IMS is based on the concepts recommended by ISO standards and the IAEA prescriptions: the entirety of work can be structured and interpreted as a set of interacting processes that can be planned, performed, measured, assessed and improved, and, those performing assessing work, all contribute in achieving quality and ensuring safety. The IMS has been developed in the way to be continuously refreshable and additive. That's why IMS will be added with new instructions, procedures and others, which will correspond to new activities arising during the reactor reconstruction.
The IMS gives strong level of certainty in the Research Reactor safety assurance, environmental protection, reactor physical protection and secure the normal personal working conditions.

V. References

1. Standard EN ISO 9001:2000, 2000
2. Standard EN ISO 14001:2004, 2004
3. Act on the safe use of nuclear energy, Promulgated in the State Gazette No. 63 of June 28, 2002.
4. Kaoru Ishikava, Introduction in quality control, 1989
5. ARIS – software product ARIS toolset, 1997 – 2005, IDS Scheer AG

HOMOGENEOUS SOLUTION REACTOR ANALYSIS FOR ^{99}Mo PRODUCTION

A. WEIR, E. LOPASSO, C. GHO
Nuclear Engineering Dept. Argentine Atomic Energy Commission
Av. Bustillo 9500 Centro Atómico Bariloche, 8400 - Argentina

ABSTRACT

The neutronic behavior of a homogeneous solution reactor for ^{99}Mo was analyzed. The aim of the research is to study the neutronic characteristics in order to assess important parameters for reactor design and to set the main calculation options. All calculations show very safe neutronic behaviors with large negative reactivity coefficients and good ^{99}Mo production.

1. Introduction

The most widely used radioisotope in medicine is ^{99m}Tc, used on 80% of nuclear medicine procedures in the world. It is used because of its ideal features for diagnosis. ^{99m}Tc is the ^{99}Mo daughter which can be obtained irradiating ^{98}Mo enriched targets or, as a fission product, irradiating uranium targets or by homogenous solution reactors [1].
In this work, an uranyl nitrate homogeneous solution reactor for ^{99}Mo production was analyzed, establishing a neutronic processing chain for calculations related to this kind of reactor. The uranyl nitrate solution fuel (20% enriched in ^{235}U) is contained in a cylindrical stainless steel tank, surrounded with light water as neutronic reflector [2]. The reactor has 6 cadmium rods as control system.
Argentina is one of the six ^{99}Mo producer countries and the first using low enrichment targets. ^{99}Mo is produced in RA-3 reactor by uranium target irradiation and the radiochemical processing is performed at Fission ^{99}Mo Production Plant.
The only purpose of this homogeneous solution reactor is radioisotope production at lower costs. As compared to other radioisotope production options, it gives several advantages like a small burnup to produce large quantities of ^{99}Mo operating at low power.

2. Reactor model description

The analyzed reactor model has liquid fuel consisting of uranyl nitrate in a water solution with extra nitric acid. The solution is contained in a cylindrical stainless steel tank reflected by light water [3].
The reactor is refrigerated by a helicoidal heat exchanger immersed into the solution. The heat is removed from the fuel by natural convection, while water circulation inside the exchanger is forced. The secondary loop coolant is light water.
The reactor control system consists of 6 independent cadmium control rods with light water followers. An auxiliary control system is also possible by changing the solution level, but it was not included in the present modeling.
A schematic drawing of reactor core is shown in Figure 1 and main reactor characteristics in Table 1. It can be seen that the tank is not completely filled with fuel solution, and therefore the upper plenum must be filled with a inert gas (nitrogen for example) to avoid hydrogen accumulation due to water radiolysis and hence chemical explosion risk.

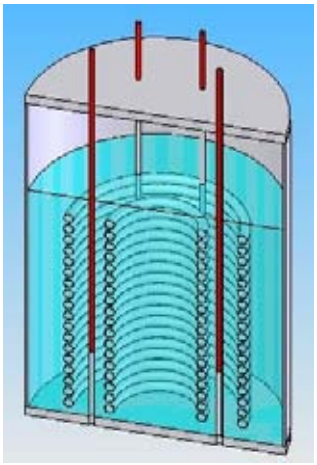

Figure 1. Homogeneous solution reactor nucleus simple model used in neutronic calculations.

Fuel	$(NO_3)_2$-UO_2
Volume	90 l
U concentration	200 g/l
U enrichment	20 %
Nitric Acid	1mol/l
Power	50 kW
Control rods	6 Cd

Table 1. Main homogeneous solution reactor features.

The ^{99}Mo production during one-day full power operation with a fresh nucleus is over 500 Ci. The ^{99}Mo activity during full power operation is shown in Figure 2 [4].

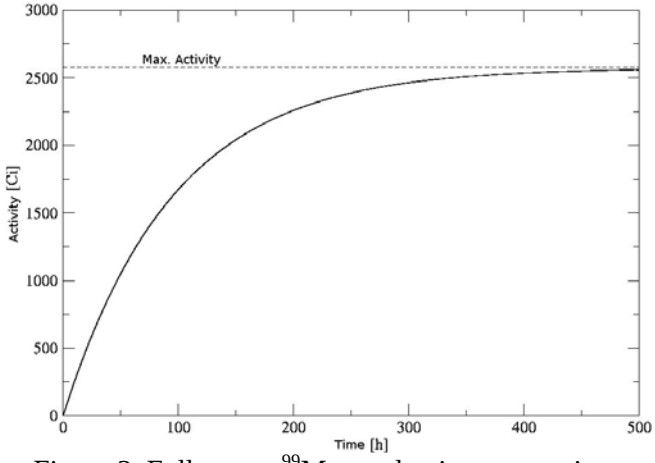

Figure 2. Full power ^{99}Mo production versus time.

3. Reactivity effects in normal operation

The system reactivity change due to several phenomena was studied. One important factor during normal operation is reactor temperature variation, leading to volumetric expansion and spectral effects [4]. Reactivity change due to fuel volumetric expansion is shown in Figure 3. This change could be as large as 600 pcm. In this case, calculation was performed with MCNP code. To study spectral effects in fuel cross sections, MCNP, SCALE/TORT and WIMS codes were used. The results are in Table 2, showing an average change of 1000 pcm for 100ºC fuel temperature variation.

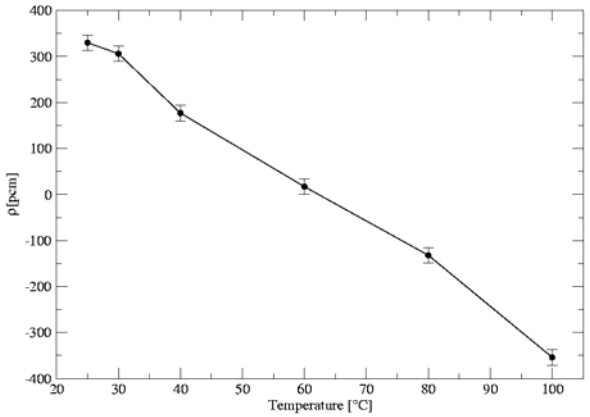

Figure 3. Solution dilatation effect over system reactivity due to increase in fuel temperature

Code	Δρ [pcm]
TORT	-800
MCNP	-1000
WIMS	-1200

Table 2. Reactivity change due to spectral effects in fuel cross sections for 100ºC temperature increase.

Another phenomenon inserting changes in system reactivity is uranium concentration variation in fuel (due to burnup and/or chemical processing, for example). Reactivity versus uranium concentration in fuel solution, for a nearly critical system, was calculated with MCNP [5] and results are shown in Figure 4. The slope is about 150 pcm per uranium gram per solution liter. Moreover, the fuel burnup after one year full power operation was calculated with WIMS and analytically (Figure 5), showing a 220 mg/l change in uranium concentration. This leads to a small change in reactivity (about 30 pcm) comparing to temperature effects.

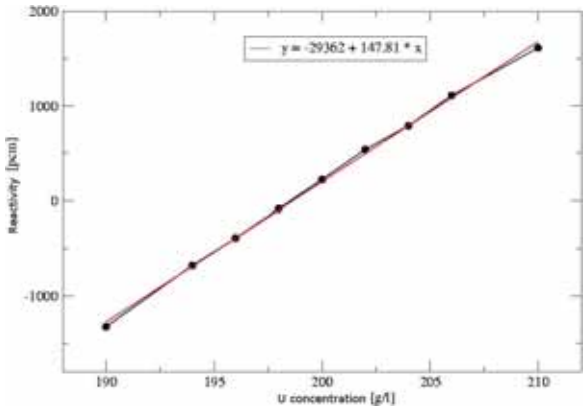

Figure 4. Reactivity versus uranium concentration variation in liquid fuel solution.

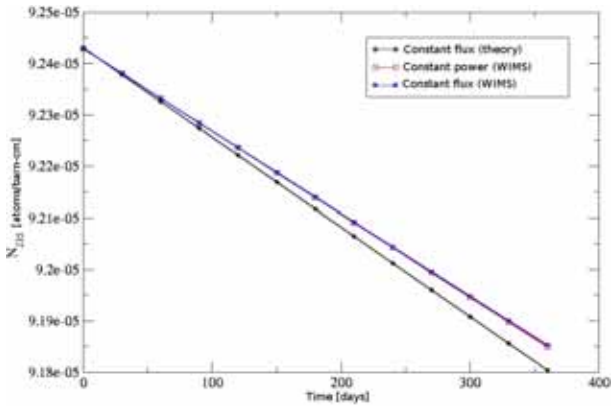

Figure 5. ^{235}U burnup in one year full power operation.

Another situation in normal operation could be fuel solution height variation reaching the critical volume. Other possible case is exceeding the critical height leading to a supercritical system. For these reasons the reactivity variation with solution height was studied. The results are in Figure 6, were the slope is around 330 pcm per cm increased near criticality.

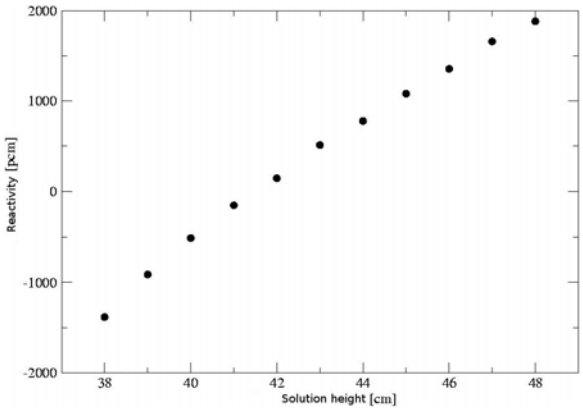

Figure 6. Reactivity variation by solution height.

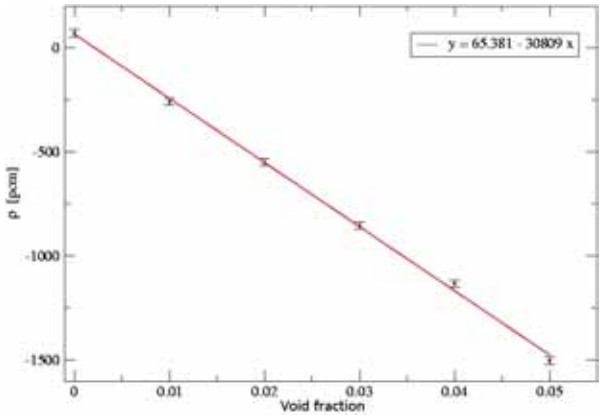

Figure 7. Reactivity function of void fraction in liquid fuel solution.

An important phenomenon in this type of reactors is a considerable void fraction in liquid fuel solution. Boiling water due to temperature and water radiolysis are the main contributors in this case. In Figure 7 can be seen that negative reactivity effect could be important depending on the void fraction value.

4. Reactivity effects in modelling and abnormal operation

As first approximation, the helicoidal heat exchanger was not modeled. It was homogenized with the uranyl nitrate solution as a model simplification. After that, four different heat exchanger models were studied (Figure 8) keeping some specifications of previous thermohydraulic calculations [2], like total tube length and tube diameter.

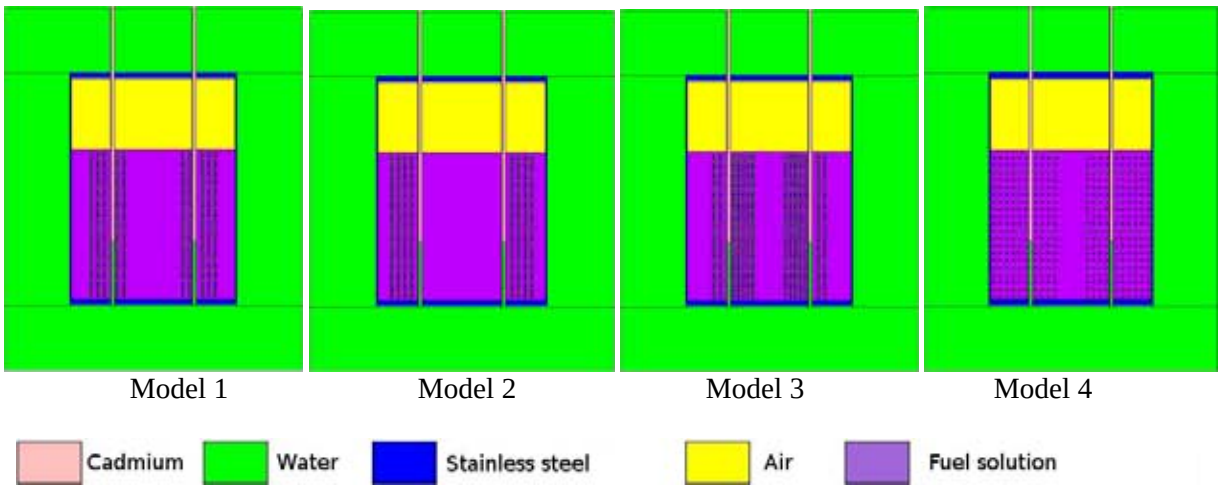

Figure 8. Different helicoidal heat exchanger models used in calculations.

Possible cases of abnormal operation were studied. In the case of loss of coolant in the secondary loop, several heat exchanger models were calculated. In all cases the results shown in Table 3 point out a large negative effect in reactivity system, keeping the reactor behavior from the safety side for this case.

Model	Δρ [pcm]
1	-1000
2	2500
3	-4800
4	1470
Homogeneous	70

Table 3. Reactivity variation due to changes in heat exchanger model.

Model	Δρ [pcm]
1	-1180
2	-850
3	-1000
4	-1240
Homogeneous	-1480

Table 4. Loss of coolant effect on reactivity for different heat exchanger models

As the fuel containment tank is surrounded by water used as reflector, any break could lead to a water insertion in fuel solution. This event produces a more diluted fuel solution and, as is shown in Figure 9, a negative reactivity insertion. On the other hand, a decrease in solution water (due to evaporation for example) leads to a positive reactivity insertion. In the last case, it is supposed that there is not uranium precipitation. Near criticality the slope is about -200 pcm per cm increased, taking into account that 1 cm equals about 2 fuel solution liters.

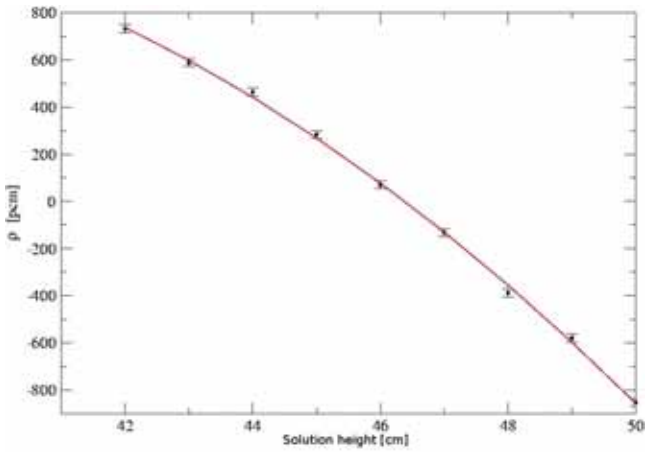

Figure 9. System reactivity versus fuel solution height change due to solution water mass variation.

5. Conclusions

Reactivity variations in normal and abnormal operation due to several phenomena were studied with MCNP, WIMS and TORT codes. A neutronic processing chain for calculations related to homogenous solution reactors was established integrating stochastic and deterministic codes.
All calculations show very safe neutronic behaviors with large negative reactivity coefficients. The fuel burnup and its reactivity effects are low with a considerable molybdenum production leading to a good production efficiency. As reactivity has a strong dependence on the heat exchanger geometry, a detailed thermohydraulic calculation is needed.

6. References

[1] Glenn, D., Heger, S., Hladik, W.: *Comparison and Characteristics of Solution and Conventional Reactors for Mo-99 Production*, Nuclear Technology, **118** (1997)

[2] H. Blaumann et al.: *Nuevo método de producción de radioisótopos de fisión de interés comercial mediante el empleo de un reactor homogéneo*. Programa de Radioisótopos y Radiaciones, CNEA, Marzo 2004
[3] A. Weir, E. Lopasso, *Analysis of an Homogeneous Solution Reactor for ^{99}Mo Production*, Advance Reactor Physics Division, Bariloche Atomic Center – INIS 36110972 (2005).
[4] A. Weir, E. Lopasso, C. Gho, *Homogeneous Solution Reactor Analysis for ^{99}Mo Production*, Advance Reactor Physics Division, Bariloche Atomic Center – AATN (2005).
[5] A. Weir, E. Lopasso, C. Gho, *Homogeneous Solution Reactor Analysis for ^{99}Mo Production*, Advance Reactor Physics Division, Bariloche Atomic Center – AATN (2006).

UPGRADING OF JRR-3/JRR-4 NEUTRON BEAM UTILITIES - FOR COLD NEUTRON BEAM AND BNCT -

K. YAMAMOTO, I. TAMURA, H. KUMADA, T. MARUO
Department of Research Reactor and Tandem Accelerator, Japan Atomic Energy Agency, 2-4 Shirakata-shirane, Ibaraki-mura, Naka-gun, Ibaraki, 319-1195, Japan

ABSTRACT

To response to their requests, we proposed two plans. One is the enhancement of cold neutron beam intensity for Japan Research Reactor No.3 (JRR-3) and the other one is the progress of Boron Neutron Capture Therapy (BNCT) for JRR-4. We are expecting to achieve 10 times the present intensity in our maximum extent so that the good complementary relation with J-PARC in one site can be established with JRR-3. The various medical irradiation technologies in BNCT at JRR-4 should be established in order to promote the medical application of nuclear energy. Although BNCT in JRR-4 has been mainly applied to therapy against brain tumor so far, technical developments to expand its application to therapy against the other cancers such as lung cancer, head and neck cancer are carried out as the needs are increasing these days.

1. Introduction

The JRR-3 of the Japan Atomic Energy Agency (JAEA) was re-constructed in 1990 with a cold neutron source and five neutron guide tubes in order to meet with the neutron beam experiments those that increased rapidly [1]. JSNS (Japanese Spoliation Neutron Source) of high intensity pulsed neutron source at the Material and Life Science Facility in the Japan Proton Accelerator Complex (J-PARC) will be constructed by 2008. The time-integrated neutron intensity at 10 m from the coupled moderator of JSNS is estimated to be 4.6 x 10^8 n/cm^{2}s with a peak wavelength of 3 Å. On the other hand, it is 2.3 x 10^8 n/cm^{2}s with a characteristic wavelength of 4 Å in a C2-1 beam port at 30 m from the cold moderator of JRR-3. That is to say, it is expected roughly that the steady cold neutron intensity of JRR-3 is half of that of JSNS with a power of 1MW so far. Of course, it is not easily compared with each other. JSNS is desired to exceed the steady beam intensity of the reactor source in the experiments that requires the time-integrated intensity such as spin echo experiment, small angle scattering, neutron radiography, prompt gamma ray analysis. Because of above Japanese neutron supply situation the target of JRR-3 upgrade plan was focused in 10 times of cold neutron intensity for continuous neutron requirement. In this plan, the cold neutron source and the neutron guide tubes should be upgraded without the increase of reactor power because of the budget.

The various medical irradiation technologies in BNCT at JRR-4 should be established in order to promote the medical application of nuclear energy. Although BNCT in JRR-4 has been mainly applied to therapy against brain tumor so far, technical developments to expand its application to therapy against the other cancers such as lung cancer, head and neck cancer are carried out as the needs are increasing these days. In this situation, a collimator and a setting-system to enable BNCT at a seated position were developed and used in practice.

2. Upgrading of JRR-3 Cold Neutron Beams

2.1 Design of Moderator and Neutron Guides

In cold neutron source (CNS) moderator vessel shapes, the spherical, cylindrical annulus or crescent shape with neutron trap such as NIST [2], ORPHEE [3] and CARR [4] are used recently. The JRR-3 liquid hydrogen moderator vessel for CNS is made of stainless steel and is flat shape which is the same type as old ORPHEE vessel [5]. The neutron intensity could be increased by optimizing the shape and material of the vessel. In a condition of our design of a new vessel, we should consider spatial limit and thermal limit to use an existing cooling system and an existing pipe, which the vessel

is inserted in. We also aim to increase the cold neutron beam intensity by replacing the current nickel mirror to Ni/Ti super-mirror in neutron guide tubes

The neutron gain of upgraded JRR-3 CNS was evaluated with the MCNP-X[6]. In addition, the McStats[7] code, which is the ray trace Monte-Carlo code, was used to design the neutron guide. Figure 1 shows the arrangement of cold neutron beam tube. In the MCNP-X simulation model, the core is defined as the homogeneous cylindrical fission source where the vertical fission distribution was determined by experimental results. The new vessel is designed as a boat-bottom shape and made of aluminum. The vessel outline dimensions are outer height 25 cm, outer width 118 cm and vessel wall thickness 2 mm, body radius 6.5 cm in outside / 3.1-4.1 cm inside, body annular arc with a central angle of 146 degrees, outer diameter 2.6 cm / inner 2.2cm in the neck. A 3-D imaging view of the vessel is shown in Figure 2. The horizontal space the body expands to 2.5cm from 2cm in consideration with decreasing by vapor void fraction, and an upper part and a bottom part have ellipsoidal inner face. The new vessel would be cooled by natural circulating saturated hydrogen at near atmospheric pressure. Therefore, the radiation heating of the vessel should be lower than cooling capacity of the existing system. The ortho-para hydrogen ratio with the reactor full power operation also was assumed 65%.

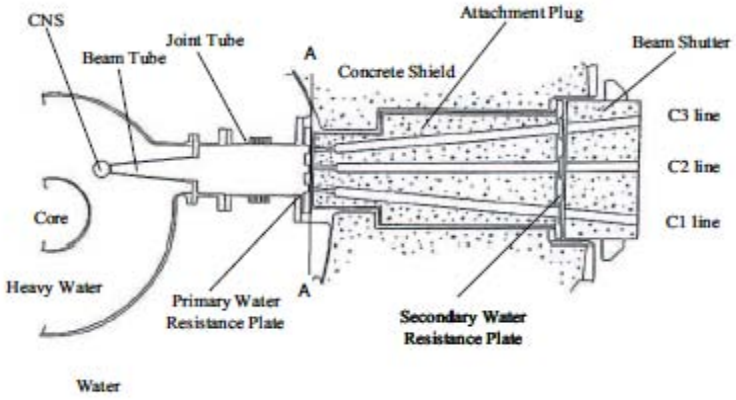

Fig.1 Arrangement of cold neutron beam tube at

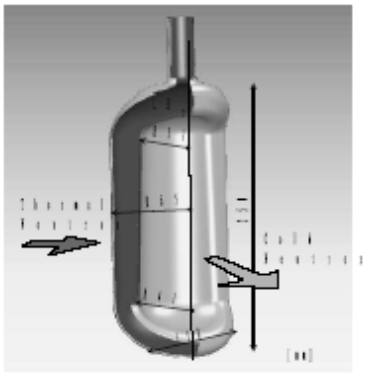

Fig.2 Three dimensions CAD imaging view of new vessel, which is called the boat-bottom shape vessel.

The neutron spectra for existing flat shape stainless steel vessel and boat-bottom shape aluminum vessel were used to connect the MNCP-X results to the McStas simulation. The joint is shown in an A-A line in Figure 1. The idealized mirrors on simulations in the neutron beam guides were arranged with actual positioning data measured during installation of current guides. The mirror optical properties are defined by the experimental neutron refraction data. The inside dimension of a guide tube element is 80cm in length, 12cm in height and 2cm width which is considered not to peep at the core side directly by using the curved guide. The neutron guides are placed after the beam shutter in each line. However, the optimization of neutron guides should be decided on the performance of connected experiment instruments, and should be achieved on the basis of ready-made technology.

2.2 Performance of Cold Neutron Beams

The neutron spectra at the joint of the current vessel and the new vessel are shown in Figure 3. The closed circles show the neutron flux of the new vessel with 0 % void fraction, and open circles show that of the current vessel. The neutron intensity of new vessel was 1.7-2.6 times for current vessel in the energy range from 3.5×10^{-4} eV to 0.1 eV. It has been known as reentry cavity effect in the geometry in hydrogen moderator such as the ORNL, NIST and ILL that the neutron gain is improved. The flux distribution of neutron beam on a plane between the beam tube and the joint tube also was checked in uniformity. It was observed that distribution in cold region (above 0.01 eV) was uniformly flat but that distribution in thermal region (0.01 - 0.1 eV) became low to moderate insufficiently at core side. In consideration of installation condition, this shape was selected from some of other geometries such as a horizontal cross-section into a hollow annulus, a half opened hollow annulus and

a crescent shape. The radiation heating of the new vessel was 211W that is 75% of the current vessel, because gamma heating of aluminum is lower than that of stainless steel by material density. It was shown that the cooling condition also was excellent with advantage of twice neutron gain in relative.

The neutron spectra at C2-1 port were calculated for 1Qc mirror as current mirror, 2Qc and 3Qc performance mirror with industrial specifications. The neutron source was assumed to be uniform spatial distribution and spectra, which was edited from MCNP result. The calculation source became rational approximation because it is difficult to improve statistics accuracy on the joint source distribution. We impose ourselves on a limiting condition that the gain factors for each guide should be controlled in a little impact on the distribution in comparison with current condition. Neutron transport efficiency at 4Å could be improved dramatically 4.4 times if the current 1Qc mirror could be replaced with the 3Qc mirror. Also, the characteristic wavelength would be shifted from 4 Å to 2.4 Å. The divergence of neutron beam increased with the Qc value of mirror in comparison with same wavelength, but the divergence amplification factor decreased with the Qc value. In case of 4 Å required a Low-energy Triple-Axis Spectrometer (LTAS) at C2-1 port, half bandwidth in beam divergence of 1Qc, 2Qc and 3Qc were 0.6, 0.9 and 1.1 degrees in horizontal direction (see Figure 4) respectively, and were 0.8, 1.4 and 1.7 degrees in vertical direction respectively. The gross neutron intensity would be increased 5.2 times in 3Qc case. These results indicated that the cold neutron beam intensity could be improved about 10 times for the current intensity by two modifications.

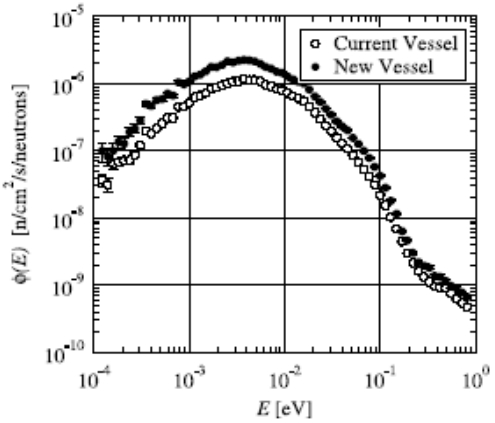

Fig.3 Neutron spectra on the joint point for the flask shape vessel and the boat-bottom shape vessel.

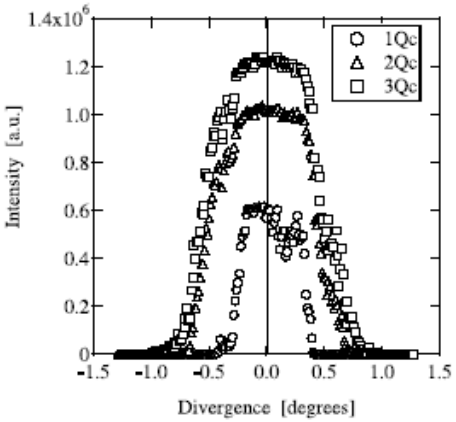

Fig.4 Horizontal neutron beam divergences with 4 Å at the LTAS beam port for 1Qc, 2Qc and 3Qc mirror.

3. Development of Irradiation technology for expanding BNCT applicability

Though BNCT clinical studies for head and neck malignancies were started recently at Kyoto University Research Reactor [8], it is difficult to carry it out in JRR-4. The reason being that positioning to keep an affected part such as the mumps in a irradiation field in case of BNCT for head and neck cancer because the shoulder of patient touches to a wall of irradiation room. So we developed a new collimator, which has a circular opening of 12cm in diameter, for head and neck cancer. The long collimator jutting out from the wall to 15cm was very necessary to apply the BNCT for the head and neck cancer.

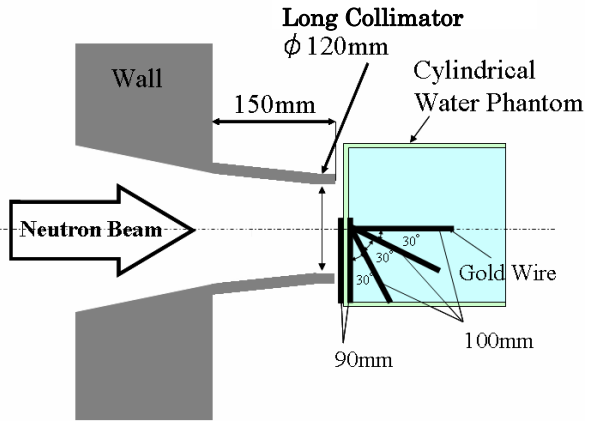

Fig.5. Arrangement of cylindrical water phantom to long Collimator.

The performance of the special collimator were compared with a circular opening collimator of 12cm in diameter, which is usually used for the brain tumor, in the thermal neutron flux

distributions in a cylindrical water phantom. The thermal neutron fluxes in the phantom for the long collimator and for the standard collimator were measured with two beam conditions of Thermal Neutron Beam mode 1 (TNB-1) and Epithermal Neutron Beam mode (ENB). The measurement results are shown in Figure 6. Positions of thermal neutron peak, which is generated around the phantom surface, of the long collimator for two beams were a little deeper than that of the standard collimator. However irradiation time doubled because the maximum values for each mode were reduced by half of the standard collimator value. The simulated value with MCNP in thermal neutron flux as shown in Figure 6 shows a good agreement compared with measured values. These results show the propriety of MCNP joining sources that used for dose evaluation calculations for patients.

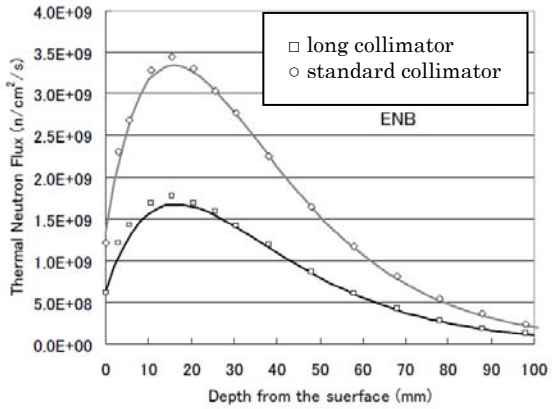

Fig.6-(a) Thermal neutron flux in water phantom for epithermal neutron beam mode

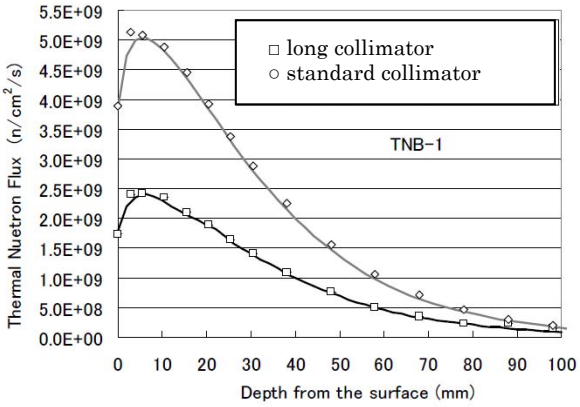

Fig.6-(b) Thermal neutron flux in water phantom for Thermal neutron beam mode 1

We developed a new collimator for head and neck cancer. It is difficult in positioning to keep an affected part such as the mumps on an irradiation field in case of BNCT for head and neck cancer because the shoulder of patient touches to a wall of irradiation room. The long collimator jutting out from the wall to 15cm was very necessary to apply the BNCT for the head and neck cancer.

4. Conclusion

Through the conceptual design for upgrading JRR-3 in cold neutron beam, it has been shown that the intensity of cold neutron beam may enhance 10 times as the current intensity. More specifically optimization of the CNS vessel could increase the intensity twice, and neutron guides replacement with high efficiency 3Qc mirror could increase about 5 times. We developed the long collimator jutting out from the wall to 15cm for head and neck cancer. The long collimator has been already applied effectively as the special collimator for 11 times of clinical trials of head and neck cancer. We will advance the development of irradiation technology for expanding BNCT applicability against the other cancers such as lung cancer.

[1]F. Sakurai, Y. Horiguchi, S. Kobayashi, M. Takayanagi, Physica B, 311, (2002) 7.
[2]R. E. Williams and J. M. Rowe, Physica B. 311 1-2, (2002) 117.
[3]B. Farnoux, B. and M. Maziere, Proceedings of the fourth meeting of the International Group On Research Reactors, Tennessee, USA, May 1995 (1995) 84.
[4]Q. Yu, Q. Feng, T. Kawai, F. Shen, L. Yuan, L. Cheng, Proceedings of the International Symposium on Research Reactor and Neutron Science, Daejeon, Korea, April 2005(2005) 638.
[5]P. Breant, International Group on Research Reactors Conference, Knoxvill, TN (USA), 28 Feb.-2 Mar., 1990, (1990) 117.
[6]Laurie S. Waters, ed., MCNPX User's Manual, Version 2.4.0, Los Alamos National Laboratory report LA-CP-02-408 (2002).
[7]K. Lefmann and K. Nilesen, Neutron News 10, (1999) 20.
[8] T. Aihara, J. Hiratsuka, N. Morita, M. Uno, Y. Sakurai, A. Maruhashi, K. Ono, T. Harada, Head & Neck, 28[9], (2006) 850.

$U(AL,SI)_3$ STABILIZATION BY ZR ADDITION

L. M. PIZARRO, P. R. ALONSO AND G. H. RUBIOLO

Unidad de Actividad Materiales, Unidad de Energía Nuclear, CAC, CNEA
Avda Gral Paz CP Argentina

ABSTRACT

Four alloys were made within the quaternary system U-Al-Si-Zr in order to assert the minimum Zr content for fixed 0.1 wt. % Si content that could stabilize $(U,Zr)(Al,Si)_3$ against $U(Al,Si)_4$ formation. Heat treatments at 600 °C were undertaken and samples analyzed by means of XRD, EMPA and EDS techniques. Evidence was found of both Zr solubility in UAl_3 and presence of UAl_4 phase for a maximum of 6 wt. % Zr content in the alloy. A remarkable conclusion is that Zr was only found in the primary solidified phase $(U,Zr)(Al,Si)_3$, which does not even partially transform to $U(Al,Si)_4$ under heat treatment.

1. Introduction

As a means of reducing high porosity formation in the interlayer between uranium alloy solution and aluminum matrix in dispersed fuel, it has been proposed that UAl_3 (cP4, space group 221) compound should be stabilized against UAl_4 (oI20, space group 74) formation. Promising results have already been obtained showing that Si addition to the aluminum matrix is able to inhibit UAl_4 formation [1,2,3]. However, it was also noticed that minor silicium quantities should be required in the presence of fourth element collaboration [4]. An already suggested candidate is Zr, as a theoretical construction based on semi empirical Miedema formation energies predicts [4]. Experimental evidence [5] shows that 14% zirconium third element addition is enough to inhibit UAl_4 formation. No experimental results have been found showing simultaneous behavior of both silicon and zirconium when added to U-Al alloys. We thus decided to determine $U(Al,Si)_3$ phase stability for constant Si concentration as a function of zirconium content. We performed stabilization experiments in 50U 49.9Al 0.1Si alloys with 0, 1, 3 and 6% Zr addition (weight percentages). Heat treatments at 600°C (100h and 1000h) were undertaken and results were analyzed by x-Ray diffraction, metallographic and composition measurement techniques. UAl_4 was not suppressed with Si and Zr contents evaluated in this work, as a slight evidence of UAl_4 presence was still found in heat treated samples with 6%Zr content. Although, it can be observed that UAl_4 related x-Ray peaks intensities diminish with higher Zr contents. Thus, our efforts served to gain some knowledge about the possibilities of retarding the peritectic reaction that leads to UAl_4 formation.

2. Experimental techniques

Four alloys were made from uranium 99.975 %, aluminum 99,9 %, silicon 99,999 % and zirconium 99,7 % (alloys labeled 0, 1, 3 and 6, Table 1). Alloys compositions were designed taking into account the U-Al binary liquidus, as a base for quaternary solidification path estimation. In this way, we sought for UAl_3 as primary phase avoiding the formation of UAl_2. Figure 1 shows our alloys global composition in a binary U-Al phase diagram. Si content was determined following Boucher work [1] were he established that a content of 0.1 till 0.6 w% Si in a U-Al alloy is not enough to inhibit UAl_4 formation, though time required for transformation increases with Si content. We thus decided to try increasing amounts of Zr addition in order to suppress the reaction between Al and primary $(U,Zr)(Al.Si)_3$ to give

$U(Al,Si)_4$. Si content was chosen as 0.1 wt % in order to obtain a result evident for short heat treatment times.

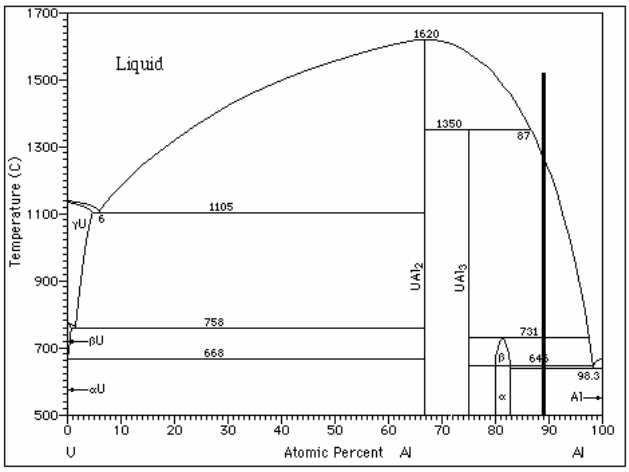

Figure 1. U-Al phase diagram [6]. The vertical line stands for our alloy composition design.

A non-consumable tungsten electrode arc furnace was employed to melt the pure components and produce the alloys under a controlled argon atmosphere using a water refrigerated copper crucible and an oxygen titanium getter. The alloys were melted and remelted at least four times to ensure homogeneity.

Heat treatments at 600 °C were made during 100 hours and 1000 hours. The interest in 100 hours experiments was focused in determining whether Boucher result was reproduced with Zr added at the same temperature and duration he experimented. In 1000 hours experiments we expected equilibria had been reached. Heat-treated specimens were wrapped in tantalum foils and sealed in silica tubes under argon atmosphere to protect them from contamination during heat treatments. Finally, they were water-quenched to room temperature without breaking the containers.

Metallographic techniques and composition measurements were employed to identify the different phases. The alloys were examined by optical microscopy and by scanning electron microscopy (SEM) in a PHILIPS PSEM-500 apparatus. They were also analyzed by Energy Dispersive Spectroscopy (EDS) in the same equipment and electron-probe microanalysis (EPMA) in a Cameca SX50 equipment at 20 KV, fitted with a wavelength-dispersive spectrometer; and by X-ray diffraction (XRD) in a PW3710 BASED PHILIPS equipment employing Cu-Kα_1 and Kα_2 radiation at room temperature.

Prior to optical, SEM and EPMA analysis, the samples were grounded on silicon carbide paper, polished with diamond paste (1 μm) and electrolitically polished at 20 volts during 10s using a solution of phosphoric acid, ethylic alcohol, distilled water and 2-n-butoxiethanol at volume ratio 54: 21.6: 2.8: 21.6. XRD samples were free from electrolitic polishing in order to exhibit a plane surface.

Sample (label)	U (wt.%)	Al (wt.%)	Si (wt.%)	Zr (wt.%)
0	50.00	49.90	0.1	0.0
1	49.47	49.43	0.1	1.0
3	48.48	48.42	0.1	3.0
6	47.00	46.90	0.1	6.0

Tab 1. Alloys compositions.

3. Results and Discussion

a) Morfological evolution with heat treatment al 600 °C

Metallographic examination of 0, 1 and 3 as cast alloys revealed a primary phase surrounded by an eutectic component (Fig 2). The same primary phase is observed in alloy 6, while the eutectic is not quite evident.

After heat treatments, a broadening with time is observed in eutectic precipitates, remaining the distinction between primary phase and eutectic components (Fig 4).

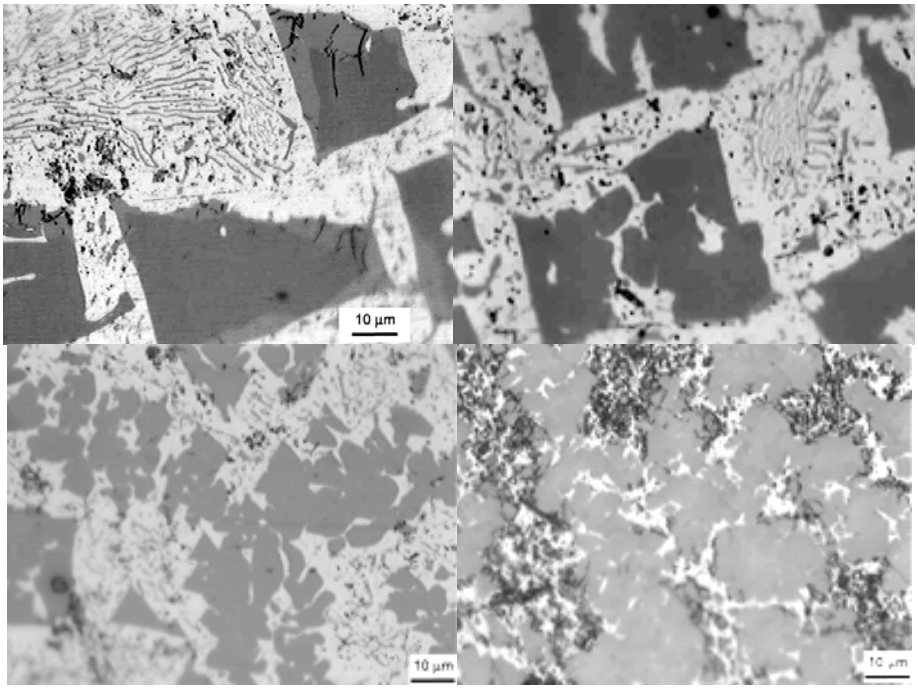

Figure 2. From left to right, as cast metallographies of samples 0, 1, 3 and 6.

b) $U(Al,Si)_4$ formation

Analyses of XRD patterns revealed the presence of UAl_3, UAl_4 and Al phases in alloys 0, 1 and 3 in as cast samples, and in heat treated samples from all alloys. However, in the as cast sample from alloy 6 only UAl_3 and Al phases were detected. In Table 2 we resume intensities belonging to (013) peak characteristic of UAl_4 phase. Heat treated samples evidence smaller quantities of UAl_4 phase with increasing zirconium content. Though this analysis would not be accurate concerning as cast samples, peaks intensities serve so as to assert UAl_4 presence.

	0	**1**	**3**	**6**
As cast	2.80	7.40	1.40	Not detected
100h 600°C	28.2	53.3	4.80	2.5
1000h 600°C	No pattern	40.2	13.8	7.6

Table 2. Intensities of UAl_4 (013) peak relative to more intensive peak in the sample (in %), denoting UAl_4 presence in samples from all alloys with different heat treatments.

c) Solubility of Zr in ternary phases

A first analysis was made from XRD patterns. In both as cast and heat treated samples, lattice parameter of UAl_3 phase shows a tendency to diminish with increasing zirconium content, while lattice parameters belonging to Al phase are invariant (Table 3). This fact is seen as an evidence of solubility in the UAl_3 phase and not in Al. Variations are also evident in UAl_4 lattice parameters with increasing Zr content. These could arise from the small size of UAl_4 particles, which are expected to render smaller as Zr content is increased, thus leading to

broader peaks and more uncertainty in the line assessment. Possible microstrains between this phase and surrounding UAl_3 or Al phases could also contribute to uncertainty.

Sample	Lattice parameter (Å) (± 5 $10^{(-2)}$ Å)		
	Al_3U	Al_4U	Al
As cast			
0	4.27	a=4.40 b=6.25 c=13.73	4.05
1	4.26	a=4.40 b=6.25 c=13.73	4.05
3	4.25	a=4.42 b=6.25 c=13.90	4.05
6	4,22	-	4.05
HT 1000h 600°C			
1	4.25	a=4.39 b=6.22 c=13.67	4.05
3	4.25	a=4.40 b=6.25 c=13.73	4.05
6	4.23	a=4.40 b=6.25 c=13.74	4.05

Table 3. Lattice parameters calculated from experimental diffraction patterns.

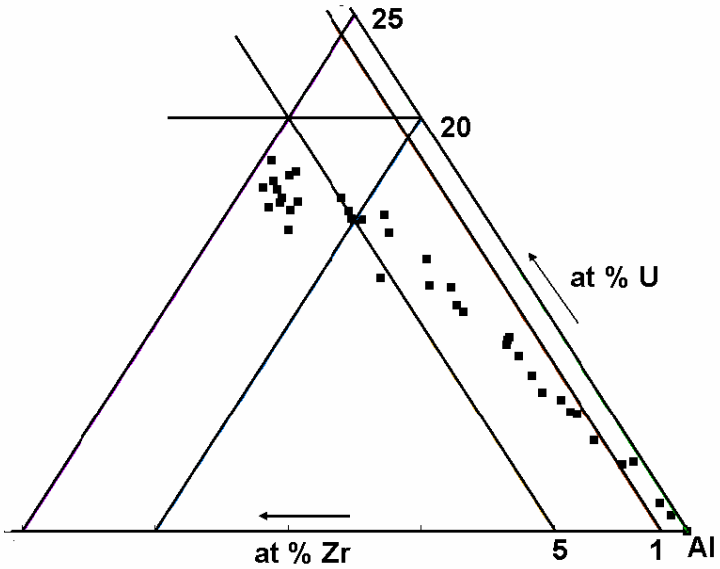

Figure 3. EPMA composition measurements in sample 6 heat treated at 600°C during 1000h.

Composition measurements were undertaken both by EPMA and EDS techniques in samples heat treated during 1000 h at 600°C. Tendencies from EPMA are shown in Figure 3 while Figure 4 shows a typical backscattered electron image obtained by EDS in sample 6. Figure 3 shows composition tendencies in the ternary phase diagram U-Al-Zr. We consider it is representative of the quaternary diagram as all samples have the same Si content and this content is small enough to consider that the ternary diagram is not quite modified. EPMA

data was measured on the primary phase and on the Al matrix. Analysis reveals that the primary phase is (U,Zr)Al_3 and the matrix is Al, measurements in between the two corresponding compositions serve as to depict a segregation path. In agreement with this, EDS measurements showed the presence of Zr throughout the primary phase, but the small precipitates in the matrix (Fig 4) turned out to content 0 % Zr. As XRD demonstrated the presence of UAl_4 phase, and the primary phase is UAl_3 after EPMA, we conclude that the small precipitates in the matrix, forming with it the eutectic component, are UAl_4 particles. And thus, after EDS measurements, we can assert that Zr is not found in solution in UAl_4 but only in UAl_3.

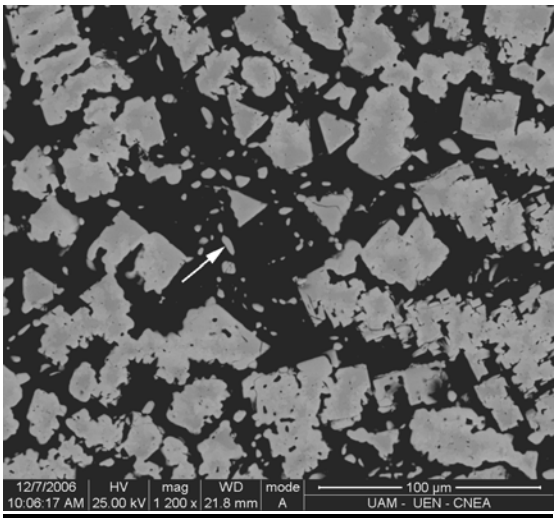

Figure 4. EDS backscattered electron image of sample 6 heat treated at 600°C during 1000 h. The arrow indicates a typical particle that resulted free from Zr.

Conclusions

- The alloys with 0.1wt.%Si studied in this work show a primary phase consisting in (U,Zr)$(Al,Si)_3$ and a eutectic component consisting in an Al matrix with $U(Al,Si)_4$ particles. $U(Al,Si)_4$ grew with heat treatments, as it was demonstrated by XRD patterns from sample 6 stabilized for 1000 h at 600°C. Nevertheless, (U,Zr)$(Al,Si)_3$ phase forming the primary phase did not transform to $U(Al,Si)_4$ as it was demonstrated by composition measurements.
- The addition of Zr in amounts till 6 wt. % to 50U 49.9Al 0.1Si alloys does not inhibit UAl_4 formation. Higher Si contents should be tried. Moreover, attention should be payed to solidification path in order to avoid the eutectic formation.

Aknowledgements

This work was partially supported by the Secretaría de Ciencia y Tecnología del Gobierno Argentino under grant BID 1201/OC-AR, PICT Nº 12-11186 (program 2004-2006).

References

[1] Boucher R, J. Nucl. Mater., 1 (1959) 13-27
[2] Thurber W.C. and Beaver R.J., Oak Ridge (USA) Report, ORNL-2602 (1959)
[3] Picklesimer M.L. and Thurber W.C.,US Patent 2950188, USPO (1960)
[4] Kim Y. S., Hofman G.L., Ryu H.J. and Rest J., 27th RERTR meeting, Boston-USA, 2005, paper S14-3
[5] Chakraborty A.K., Crouse R.S. and Martin W.R., J. Nucl. Mater., 38 (1971) 93-104.
[6] Massalski, T.B., et al.,Binary Alloy Phase Diagrams. 2 ed. 1990, ASM Int.: Materials Park, OH.

A STUDY ON POSSIBILITY OF USE OF LEU MR-6 TYPE FUEL FOR ADS DESIGN

M. P. PEŠIĆ
Centre for nuclear technologies and research, VINCA Institute of nuclear sciences
P. O. Box 522, NTI-150, 11001 Belgrade - Serbia

ABSTRACT

Recent studies are carried out at the VINCA Institute for possibility of use of Russian future low-enriched uranium-dioxide fuel (dispersed in an aluminium matrix) of TVS or MR-6 type, assuming that such fuel will be available in Russian Federation soon, due to development of new fuel within RERTR Program. Here are shown initial results for neutron yield and spectrum for interaction of proton beam with idealized cylindrical long target obtained by MCNPX2.4.0 code and results of criticality calculations and neutron spectra obtained by MCNP5 code for a case of the ADSRF with LEU MR-6 type fuel assemblies in lead matrix. The proposed ADSRF, beside its usage as a valuable research machine, may contribute to following and developing contemporary nuclear technologies in the country useful for eventual future nuclear power option.

1. Introduction

The idea of the ADS project is based on the fact that the construction of the TESLA Accelerator Installation in the Vinča Institute will be finished within few years. In addition, a rich experience in design, construction, operation and maintenance of both research reactors (RR) in the Institute, gained in the last 40 years, will be used. Proposal for a conceptual design of an accelerator driven subcritical research reactor was based initially on the stock of available fresh HEU TVR-S type fuel elements (FE) of Russian origin at both Vinča's RR. The basic design request for the ADSRR features is that it should simulate neutron characteristics of high-power ADS with intermediate neutron spectrum. Such ADSRR could respond to worldwide requests for experimental needs for validation of various nuclear parameters of the proposed ADS. Characteristics of such type ADS with HEU (ADSRR-H.) were studied in period 1999 – 2002 [1 – 4].

In compliance with the RRRFR Program, the Vinča Institute has returned fresh HEU FEs back to the Russian Federation [5] in August 2002, As a usage of HEU FEs in research reactors is not further recommended, a new study of ADS facility design was initiated in last few years, based on usage of a modern Monte Carlo particles transport codes and assumed commercial availability of LEU FEs of Russian origin. This conceptual design of the proposed ADSRR with TVR-S type FEs was studied in period 2002 – 2004 and is designated as ADSRR-L. Recent feasibility studies are related to possibility of usage of LEU MR-6 type FAs in ADS and this facility is designated as ADSRF-MR6. Purpose of this paper is to show initial results of neutronic designed parameters of the proposed ADSRF-MR6 and compare them to the basic requirements and spectrum characteristics of the previous ADSRR-H.

2. TESLA Accelerator Installation

The TESLA Accelerator Installation (TAI) in the Vinča Institute is a multi-purpose facility for production, acceleration and use of ions. Construction of the installation began in 1989 and comprises a compact isochronous cyclotron - the VINCY Cyclotron; an electron cyclotron resonance heavy ion source the - mVINIS Ion Source (in operation from 1994); a volume light ion source - the pVINIS Ion Source (in operation from 1994), and several low and high-energy experimental channels. Due to interruptions, from various reasons, in providing funding for the construction, the first beam extraction from the VINCY cyclotron is foreseen at the end of 2008.

The VINCY cyclotron, optimised for extraction of deuteron beam, can deliver either protons with maximum energy of 73 MeV and current of 5 μA, or deuterons with maximum energy of 67 MeV and current of 50 μA. These parameters are not favourable for design of an ADS for energy production or transmutation of trans-uranium nuclides. Thus, one of the main tasks in the ADSRF project is examination of interaction of the beam particles with different target materials in order to choose and design an optimal target in respect to escaping neutron spectrum and neutron yield.

3. MR-6 Fuel Design

The MR type of FAs are produced, among other research reactors' FA types, at the Novosibirsk Chemical Concentrate Plant (NCCP), Novosibirsk, Russian Federation produces [6] These FAs may have different number (four to six) concentric fuel element tubes. Fuel meat is UO_2, dispersed in aluminium matrix. Uranium is enriched to 36 % or 80 %. Numerical neutron multiplication and spectrum studies with LEU (19.7 % ^{235}U) MR-6 fuel assembly (FA) were already carried out for possibly conversion of HEU to LEU fuel at Poland's MARIA reactor [7]. For feasibility study in this paper, MR LEU FAs with six concentric fuel tubes (MR-6) were selected. It is assumed that uranium is enriched to 19.7 % ^{235}U and UO_2 is dispersed in aluminium alloy powder (PA-4) matrix [8]. Mass of 450 g of ^{235}U per FA is assumed [7]. Cross-section of MR-6 type FA is given in Figure 1.

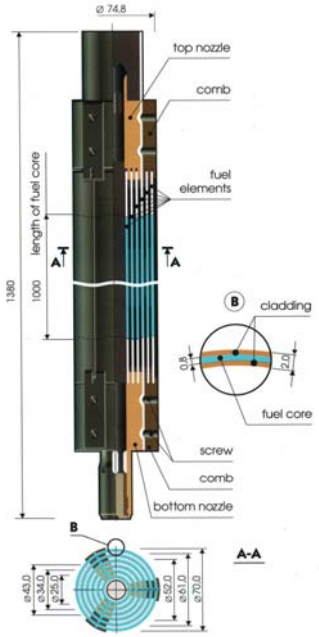

Fig. 1. MR-6 type fuel element (dimension in mm) [6]

The fuel layer of each tube of MR-6 FA is 0.8 mm thick and covered by 0.6 mm thick aluminium cladding [6] that is assumed to be made from Russian aluminium alloy AMSN2 [8]. Inner and outer diameters of fuel tubes are shown in the Figure 1. Gaps between tubes and central axial hole are supposed to be used by moderator (water). Length of the fuel layer is 1000 mm.

4. Conceptual design of ADSRF-MR6

In ADSRF with LEU MR-6 FA, gaps among fuel tubes in the MR-6 are filed by water, except in the central FA, in which axial hole is used for a target position. Total of 21 FAs (supporting external tubes OD 76 mm) are placed in holes (ID 78 mm) drilled in a lead matrix of the subcritical reactor core. The holes form a regular square lattice (5 x 5 matrix) with 110 mm pitch. Water is selected again for the primary moderator inside the FAs in aim to achieve dominant thermal energy neutron fission rate, while lead matrix is used in the subcritical core with the aim to achieve an intermediate energy neutron spectrum. Radial lead reflector is designed with average thickness of about 260 mm. There are also axial lead reflectors, above and bellow stainless steel grids, mounted at top and bottom of the core,

used to fix FAs at positions in the lattice. Height of the ADSRF-MR6 core is 1380 mm. The total mass of ^{235}U nuclide in the core is 9.45 kg, while total mass of U is five times higher: 47 kg.

The subcritical core is designed in a cylindrical stainless steel (SS) vessel (ID/OD 100/105 cm). The total mass of the whole facility is about 10 tons. Beam of charged particles is introduced to the subcritical core (through the top surface along central axis) by a separate SS tube (ID/OD 12/14 mm) under high vacuum. An idealised target, a solid metal lead cylinder (25 mm high and 10 mm diameter), is placed at the end of the beam tube, near the centre of the central FA in the core. Cross sections of designed ADSRF-MR6 core are shown in Figure 2.

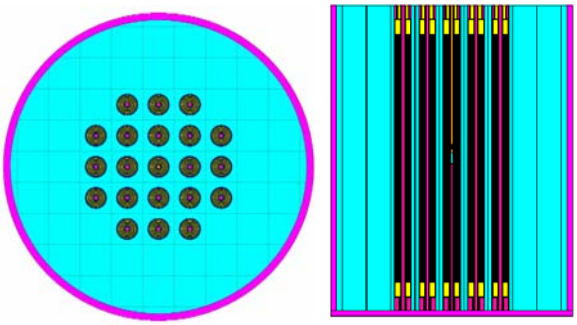

Fig. 2. Horizontal and vertical cross-sections of ADSRF-MR6

In aim to estimate escape neutron spectrum and neutron yield from the target surfaces, a 73 MeV proton parallel beam with circular cross section is assumed to hit the top surface of the lead cylindrical target along the cylinder axis. Neutron spectrum, obtained from calculation of interaction of the beam with the target material in idealized conditions (target surrounded by vacuum) by the MCNPX2.4.0 code [9] with the LA150 [10] continuous energy data library, is used as a neutron source in the subcritical system in this study. Escaping neutron and proton spectra are shown in Figure 3 for beam radius equal to zero and equal to the target radius (0.5 cm). Range of 73 MeV protons in lead is 0.90 cm, and as a consequence, only small percent of incoming protons escape the target. Energy deposited by protons in the target is shown in Figure 4. The total yield of escaping neutrons from all target's surfaces is calculated with the SHIELD [11] and MCNPX codes at 0.143 ± 0.003 neutrons per one 73 MeV proton, regardless the beam diameter. Less than 3.5 % of escaping neutrons have energy higher than 20 MeV. Peak of the escaping neutron spectrum is in energy range from 0.2 MeV to 0.8 MeV. There are no neutrons with energies bellow 1 keV, i.e., there is no thermalisation of neutrons within the target material. Fraction of protons escaping target surfaces is 14.5% in the case of 1 cm diameter beam and only 0.09 % in the case of infinite thin beam.

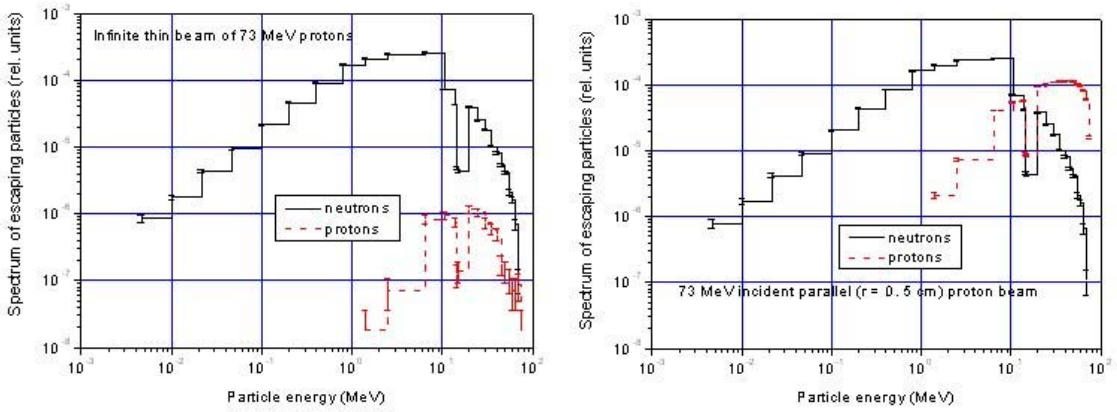

Fig. 3. Escaping neutrons and protons from the lead target

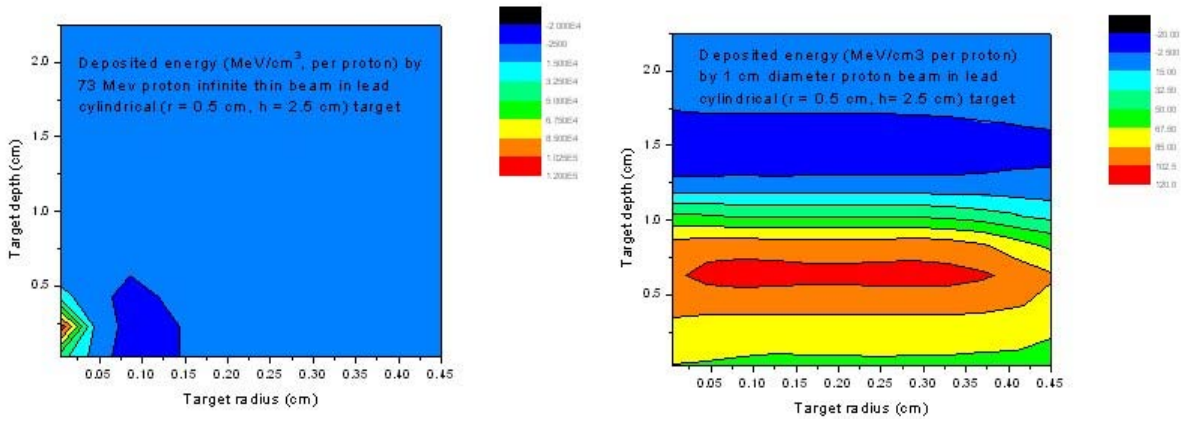

Fig. 4. Energy deposited by proton beam in the lead target

5. Results of neutronic study

The MCNP5 code [12] is used for criticality calculations of the ADSRF-MR6 with combination of the LA150 (neutron E_{max} = 150 MeV) and ENDL92 (neutron E_{max} = 30 MeV) neutron cross-sections data libraries. Only for few nuclides (impurities in the ADSRF materials) ENDF-B/VI.8 (neutron E_{max} = 20 MeV) data are used. Scattering of thermal neutrons at hydrogen atoms connected in light water molecules is encountered by application of the $S(\alpha,\beta)$ scattering law, according to the TMCCS library. Three-dimensional (3D) model of real MR-6 FA and 3D model of ADSRF-MR6 for the MCNPX/MCNP codes are developed and used.

To specify a neutron source (SDEF option) for the MCNP5 code, in the first step of the calculations, neutrons escaping the target volume with group spectra obtained in the MCNP5 code are used. The code is run for 200 000 neutron histories and the five-group spatial distribution of neutron flux and fission rate source in ADSRF-MR6 core are determined with (1σ) error less than 10%. Such spatial distribution of fission neutron source is used for the subsequent MCNP5 calculations of the neutron effective multiplication factor (KCODE option) in the ADSRF-MR6. In this step of calculation by the MCNP5 code, 2000 neutron active cycles are run with 5000 neutrons per cycle, after 100 initial ones. Simultaneously, 56-energy groups neutron spectra in various cells of the ADSRF-MR6 lattice are calculated (Figure 5). Average effective neutron multiplication factor (k_{eff}) of (0.9574 ± 0.0003) and prompt removal neutron lifetime (l_p) of (65.77 ± 0.04) μs for standard (1σ) statistical uncertainty valid for 0.67 probability are calculated. Average neutron energy producing fission is 33.255 keV.

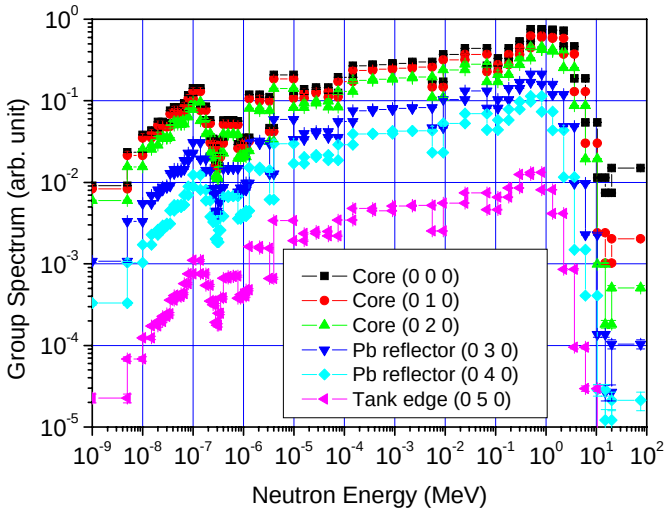

Fig. 5. Neutron spectra in cell zones of the ADSRF-MR6

Figure 5 shows that stationary neutron spectrum in the ADSRF cells is dominantly intermediate. Average neutron flux in lattice cells with LEU FAs is dominantly fast and about from 3 to 7 times higher than the thermal one. Total epithermal and fast energy neutron flux is about one order higher than thermal one at the core-reflector and the reflector-tank edge of the unshielded system. The MCNP5 calculations show that neutrons in the system are generated dominantly (83.78 %) by thermal fission ($E_n < 0.625$ eV) in ^{235}U nuclide. In three group representation, fraction of intermediate fission (0.625 eV $< E_n < 100$ keV) is only about 14.43 % of total number of fission, and only 1.79 % of all fissions are generated by fast neutrons ($E_n > 100$ keV).

6. Conclusion

The basic aim of the ADSRF-MR6 research is to study the physics and development of the technologies necessary to design a small subcritical low neutron flux research facility driven by an accelerator medium energy proton beam. Russian origin research reactor's LEU fuel elements of existing construction are assumed to be available. Initial results of the neutronic study have shown that it is possible to design such ADSRF with dominant intermediate neutron spectrum using fresh low-enriched uranium MR-6 type fuel elements and light water as primary moderator in lead matrix. That system is driven by a neutron source generated in a lead target by interaction of proton or deuteron beam, extracted from the TESLA Accelerator Installation.

7. References

[1] PEŠIĆ, M., NEŠKOVIĆ, N., PLEĆAŠ, I., "ADS project in the Vinča Institute", Proceedings of the International Conference on SubCritical Accelerator Driven Systems, SSC RF ITEP, pp. 27-33, Moscow, Russia (October 11-15, 1999)

[2] PEŠIĆ, M. P., "Research on ADS in Vinča Institute", Proceedings of the International Conference on 'Back-End of the Fuel Cycle: From Research to Solution' - GLOBAL 2001, CD ROM, pp. 1-8, Paris, France (September 9-13, 2001)

[3] PEŠIĆ, M., SOBOLEVSKY, N., "ADS with HEU in the Vinča Institute", Proceedings of the 10th International Conference on Emerging of Nuclear Energy Systems - ICENES 2000, paper no. 067, pp. 420-428, Petten, The Netherlands (September 24-28, 2000)

[4] PEŠIĆ, M., "Neutronic design of an accelerator driven subcritical research reactor", Proceedings of the International Conference on New Frontiers of Nuclear Technology: Reactor Physics, Safety and High - Performance Computing, PHYSOR 2002, paper I0106, Seoul, Korea (October 7-10, 2002)

[5] PEŠIĆ, M., ŠOTIĆ, O., SUBOTIĆ, K., HOPWOOD JR., W., MOSES, S., WANDER, T., SMIRNOV, A., KANASHOV, B., ESHCHERKIN, A., EFAROV, S., OLIVIERI, S., LOGHIN N-E., "Return of 80% HEU fresh fuel from Yugoslavia back to Russia", International Journal of Radioactive Materials Transport, Vol. **14**(3-4), pp. 173-179, NTP (2003)

[6] Catalogue "Nuclear fuel for research reactors", MINATOM, Novosibirsk Chemical Concentrates Plant (NCCP), Inc., Novosibirsk, Russian Federation (2000)

[7] BRETCHER, M. M., HANAN, N. A., MATOS, J. E., ANDRZEJEWSKI, K., KULIKOWSKA, T., "Neutronic safety parameters and transient analyses for Poland's MARIA research reactor", Proceedings of the 1999 RERTR International Meeting, pp. 1 - 14, October 3-9 (1999) Budapest, Hungary, ANL-TD-CP-100104 (1999)

[8] ROZHKOV, V. V., (NCCP), A letter no. 53-20/10080, dated 30-12-1999 to M. Pešić, the Nuclear Engineering Laboratory, the Vinča Institute, Belgrade, Yugoslavia (1999)

[9] ***"MCNPX user's manual, version 2.4.0", LA-CP- 02-408, LANL, USA (September 2002)

[10] CHADWICK, M. B., YOUNG, P. G., CHIBA, S., FRANKLE, S. C., HALE, G. M., HUGHES, H. G., KONING, A. J., LITTLE, R. C., MACFARLANE, R. E., PRAEL, R. E., and WATERS, L. S., "Cross section evaluations to 150 MeV for Accelerator-Driven Systems and implementation in MCNPX," Nuclear Science and Engineering **131** (3), p. 293 (1999).

[11] DEMENTYEV, A. V., SOBOLEVSKY, N. M., "SHIELD - Universal Monte Carlo hadron transport code: Scope and applications", Radiation Measurements, **30**, p. 553 (1999)

[12] BRIESMEISTER, J. F. (ed.), "MCNP™ – A general Monte Carlo N-particle transport code, version 5", Vol. **I-III**, LANL, Los Alamos, NM, USA (2003).

THERMAL CONDUCTIVITY OF HEAVY-ION-BOMBARDED U-MO/AL DISPERSION FUEL

R. JUNGWIRTH, N. WIESCHALLA, W. SCHMID, A. RÖHRMOSER, W. PETRY

Technische Universität München, Forschungsneutronenquelle Heinz-Maier-Leibnitz (FRM-II)
Lichtenbergstraße 1, 85747 Garching - Germany

CHR. PFLEIDERER

Technische Universität München, Physik Department E21
James-Franck-Straße, 85747 Garching - Germany

ABSTRACT

Changes of thermal conductivity during in-pile irradiation are of central importance for the large-scale use of U-Mo/Al dispersion fuel. Recently it was shown [1], that heavy ion bombardment of U-Mo/Al dispersion fuel allows to simulate the effects of radiation damage during in-pile irradiation. Heavy ion bombardment avoids (strong) activation of the specimens. They may therefore be readily examined in simple laboratory experiments. We report the development of a new method to determine changes of the thermal conductivity of U-6wt%Mo/Al and U-10wt%Mo/Al dispersion fuel due to ion bombardment. We derive changes of the DC thermal conductivity from a low frequency heat current as tracked by a digital lock-in technique. A comprehensive set of tests has been carried out that establishes the basic feasibility of our method.

1. Introduction

U-Mo alloys dispersed in Al are most promising candidates for high density fuels for research and materials testing reactors. It is most important for the qualification of this fuel for use in reactors to know the development of its thermal conductivity during burn-up. In this paper a method to measure the change in thermal conductivity of U-Mo/Al dispersion fuel caused by bombardment with heavy ions will be presented. The bombardment with heavy ions simulates part of the damages inside the fuel during in-pile irradiation [1-4]. Values will be presented and discussed.

The area that could be exposed to bombardment with swift heavy ions is approximately $3x4mm^2$ of size. Since swift heavy ions of 80 MeV energy can penetrate only the first 10µms of the U-Mo/Al sample, the expected change in thermal conductivity of the whole sample is lower than 5%. The size of the samples bombarded with heavy ions was approximately $3x15mm^2x150µm$. It was a challenging task to resolve such a small change in thermal conductivity inside such a small sample. A new method had to be found since known methods would not provide the needed accuracy.

Common steady-state methods to measure the thermal conductivity of a sample suppose both, bar shaped samples of some 10cm length and big heat currents. However, they can hardly resolve temperature gradients of less than 5K [5].

Known methods that use a heat-wave propagating through the sample to determine the diffusivity κ of the sample suppose partly samples of some 10cm length to give satisfying results [6,7]. Furthermore, the shape of the samples and the position of the temperature measurement on the sample must satisfy strict border conditions [8,9]. The standard laser-flash method to determine the thermal diffusivity of the samples could not be applied since it supposes very homogeneous samples [10]. In our case, the size of the inhomogeneities (the U-Mo/Al particles, diameter <150µm), and the thickness of the samples (<300µm) are in the same order of magnitude. Furthermore it is known, that the laser-flash method leads to inaccuracies due to double inflections when applied to thin dispersion samples [11].

Therefore, we developed a quasi-static method that uses a very low-frequency heat wave to determine the diffusivity of the U-Mo/Al samples. Using this method, one can avoid parasitic voltages that may

appear during the temperature measurement. The method will be described in chapter 2. Additional to the measurement of the change of thermal conductivity of the samples due to bombardment with swift heavy ions, the change in electrical resistivity of the samples was measured with a classical four-point-method. The change in the thermal conductivity and the electrical conductivity of the individual samples can be compared using the Wiedemann-Franz law.

2. Experimental set-up

The basic idea of our method is sending a very low-frequency (in the order of some 10mHz) heat wave lengthwise through the sample. The amplitude and the phase of the heat wave are recorded on two different points lengthwise on the sample. The diffusivity κ of the sample can be calculated from the amplitude and the phase respectively. The wavelength of the heat wave is thereby much bigger than the length of the sample. The temperature along the sample is therefore always nearly constant.
The heat wave is produced with a small electrical heater mounted on top of the sample. The bottom of the sample is mounted in a small copper sample-holder that functions as a heat dumb.
We use the well-known equation of heat conduction:

$$P = \lambda \cdot A \frac{\Delta T}{\Delta x} \tag{2.1}$$

where P is the thermal output of the heater, λ is the thermal conductivity of the sample, A is the cross section perpendicular to the surface, ΔT is the difference of the amplitude of the heat wave inside the sample on two different points lengthwise the sample and Δx is the distance of the two measuring points.
Solving equation (2.1) to determine λ leads to an expression that is proportional to the inverse of the difference of the amplitude of the heat wave. This expression has the dimension of a thermal conductivity [$Wm^{-1}K^{-1}$] and will be called "AC thermal conductivity" λ_{AC} in the future.

$$\lambda_{AC} = \frac{P \cdot \Delta x}{A \cdot \Delta T} \tag{2.2}$$

We use the model of the propagation of a heat wave in a semi-infinite half space derived by Carslaw and Jaeger [12]. The diffusivity κ of the sample can be calculated from the frequency dependant AC thermal conductivity and from the phase difference ΔΦ of the heat wave between the two measuring points.
Using the model of Carslaw and Jaeger [9] the AC thermal conductivity can be best described with

$$\lambda_{AC} = \frac{P_0 \Delta x}{A T_0 (1 - \exp(-\Delta\Phi))} \exp\left(\sqrt{\frac{x_1^2 \pi}{\kappa}} \sqrt{f}\right) \tag{2.3}$$

where f is the frequency of the heat wave and x_1 is the distance from the heater to the first measuring point on the sample.
When plotting the values for the AC thermal conductivity calculated with equation (2.2) over the frequency of the heat wave one can interpolate those with a function of the form $y = P_3 \exp(P_4 \sqrt{x})$.
Comparing this with equation (2.3) leads to an expression for the diffusivity κ of the sample:

$$\kappa = \frac{x_1^2 \pi}{P_4^2} \tag{2.4}$$

For the phase difference of the heat wave on two points x_1 and $x_1+\Delta x$ on the sample one gets after Carslaw [12] the following expression:

$$\Delta\Phi = \Delta x k + \varepsilon_0 = \sqrt{\frac{\Delta x^2 \pi}{\kappa}}\sqrt{f} + \varepsilon_0 \tag{2.5}$$

$$\Delta\Phi = a\sqrt{f} + b \tag{2.6}$$

Taylor expanding (2.5) to f around 1mHz and aborting after the linear term leads to:

$$\Delta\Phi \approx (\frac{1}{2} a\sqrt{1mHz} + b) + \frac{a}{2\sqrt{1mHz}} f \tag{2.7}$$

The phase difference of the heat wave is plotted against the frequency and interpolated with a function of the form $y = P_1 + P_2 x$. One gets for the diffusivity κ:

$$\kappa = \frac{\Delta x^2 \pi}{4P_2^2 \cdot 1mHz} \tag{2.8}$$

All measurements where carried out with two digital lock-in amplifiers that controlled the heat wave created by the heater and recorded both, the amplitude and the phase of the heat wave on two different points on the sample at the same time. The heat wave was detected with two type K thermocouples that where glued onto the sample with a two-component, electrical conducting silver epoxy glue. The distance of the two thermocouples was Δx≅4mm. Figure 1 shows the experimental set-up we used.

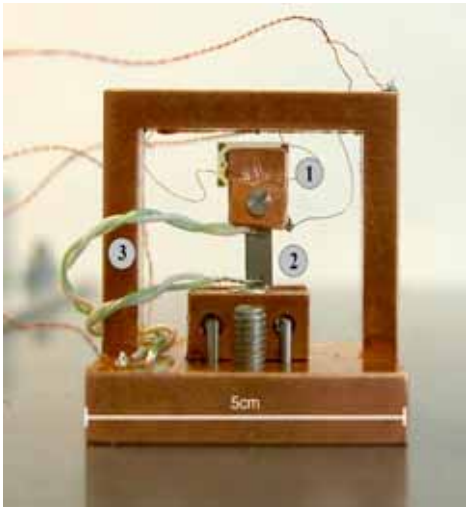

Fig. 1: The experimental set-up we used to determine the amplitude and the phase propagating through the sample (2). A small heater is mounted on top of the sample (1). The heat wave propagates from the heater through the sample into the experimental set-up, which works as a heat sink. The amplitude and the phase of the temperature wave are detected with two thermocouples (3).

Additional to the thermal diffusivity the electrical conductivity of the samples was measured before and after bombardment with heavy ions with a classical four-point-set-up. Furthermore, the specific heat of the U-Mo/Al samples and the silver-epoxy glue was measured with a commercial available device by Quantum Design. Results will be given in chapter 3.

3. Results

There were in total 4 samples irradiated with iodine ^{123}I at 80MeV at the tandem accelerator of the "Maier-Leibnitz Laboratorium" in Garching. All samples were measured before and after bombardment with iodine. The samples were provided by Argonne National Laboratoy (ANL). There were samples with U-10wt%Mo (J8, J9) and U-6wt%Mo (R11, R12) examined. The volume loading of the samples is around 55vol%U-Mo in an aluminium matrix. The preparation for examination was done inside a hot laboratory at the Garching campus. Table 1 shows the specifications of the four samples including the fluency of iodine after bombardment.

Name	***Alloy***	***Dimensions [LxWxT]***	***Distance thermocouples***	***Fluency [Ions/cm^2]***
J8	U-10wt%Mo	15,85x3,1x0,3mm^3	4,9-11,45mm	1,5x10^{17}
J9	U-10wt%Mo	14,65x3,35x0,3mm^3	2,85-10,1mm	2,03x10^{17}
R11	U-6wt%Mo	13,1x3,95x0,27mm^3	3,5-9,3mm	2x10^{17}
R12	U-6wt%Mo	13,7x3,35x0,27mm^3	3,9-9,2mm	1,96x10^{17}

Tab. 1: Summary of the U-Mo/Al samples that were examined.

The AC thermal conductivity was determined according to equation (2.2) and plotted over the frequency (figure 2a). The AC thermal conductivity is perfectly fitted with a function of the form $y = P_3 \exp(P_4 \sqrt{x})$, in agreement with equation (2.3). The phase difference of the heat wave is also plotted over the frequency (figure 2b). It is very well reproduced with a function of the form $y = P_1 + P_2 x$, in agreement with equation (2.7).

Table 2 shows the thermal diffusivity calculated from the AC thermal conductivity compared to the thermal diffusivity calculated from the phase difference and the electrical conductivity of the samples. The single absolute values of $\kappa_{AC,}$ $\kappa_{\Delta\Phi}$ and σ match quite well. Values of the electrical conductivity are in the order of magnitude one would expect [11]. However, values of the thermal diffusivity are about a factor 30 smaller than values of U_3Si/Al dispersion fuel of similar volume loading reported by Kim et.al. [11]. Calculating the thermal conductivity of the samples from the thermal diffusivity (the specific heat of U-10Mo was measured to be ~600µJmg^{-1}K^{-1}, the specific heat of U-6Mo was ~400 µJ mg^{-1}K^{-1}) leads to values also a factor 30 smaller than expected. The most probable explanation for this behaviour is a systematic error due to the model of the semi-infinite half space we used. Relative changes, however, should be unaffected.
Only sample J8 shows an decrease between 2,48% and 6,75% in electrical or thermal conductivity due to irradiation with swift heavy ions. In contrast to sample J8 sample J9 shows an significant increase in thermal and electrical conductivity after bombardment with heavy ions. Sample R11 shows now significant change in thermal or electrical conductivity. Looking at the measured values of sample R12 one notices that the electrical conductivity and $\kappa_{\Delta\Phi}$ show an significant increase. However, κ_{AC} shows an decrease. This behaviour is most likely because of inaccuracies during the measurement. In consequence this measurement is no longer considered.

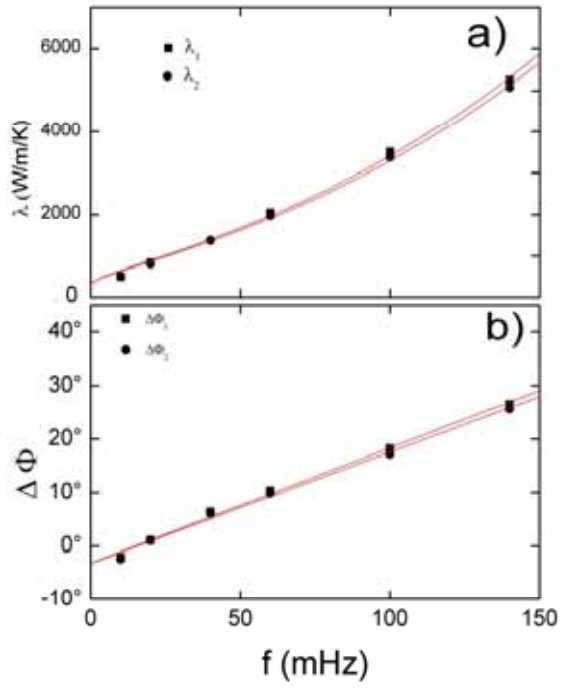

Fig. 2: AC thermal conductivity (a) and phase difference of the heat wave on two points on the sample (b) plotted over the frequency. The amplitude difference (a) is best fitted with a function of the form $y = P_3 \exp(P_4 \sqrt{x})$. The phase difference is best fitted with a function of the form $y = P_1 + P_2 x$ in excellent agreement with literature [12]. Parameters P_2 and P_4 can be used independently from each other to determine the thermal diffusivity κ of the sample.

Sample		$\kappa_{AC}[10^{-3}cm^2s^{-1}]$	$\Delta\kappa_{AC}$	$\kappa_{\Delta\Phi}[10^{-3}cm^2s^{-1}]$	$\Delta\kappa_{\Delta\Phi}$	$\sigma[10^6\Omega^{-1}m^{-1}]$	$\Delta\sigma$
J8	Before	8,595		12,1		9,99	
	After	8,015	-6,75%	11,8	-2,48%	9,53	-4,6%
J9	Before	5,91		40,6		4,88	
	After	6,335	+7,19%	83,4	+105%	6,01	+23,2%
R11	Before	4,87		17,8		9,11	
	After	4,89	+0,4%	16,95	-4,78%	9,14	+-0%
R12	Before	8,65		12,4		9,97	
	After	7,94	-8,2%	16,65	+11,06%	10,4	+4,3%

Tab. 2: Summary of the results of the conductivity measurements. Mean values before and after bombardment with swift heavy ions are displayed. The thermal diffusivity and the electrical conductivity change always in the same direction after bombardment with heavy ions, except sample R12.

4. Discussion

In this chapter a possible explanation for the varying behaviour of the thermal and electrical conductivity of the single samples will be given [13].

It is well known that in principal the conductivity of metals decreases during irradiation due to an increasing number of point defects [14]. In our case we have a complicated mixture of zones of different material combinations. Therefore a combination of different effects on the thermal conductivity has to be considered..

The sample consists of an Al matrix which embeds the U-Mo particles. After irradiation the sample can be divided into two regions: The first region is directly hit by heavy ions which will induce lattice defects in the Al matrix as well as in the U-Mo grains. Furthermore an interdiffusion layer between the aluminium and the U-Mo is created during irradiation [1]. The volume of the irradiated region is small compared to the total volume of the sample. In the first instance the thermal and electrical conductivity of the matrix will decrease due to the increasing concentration of lattice defects. However, if the temperature of the sample during irradiation exceeds ~250°C the lattice defects will possibly anneal immediately [14]. No or only a little effect will be measurable in this case. It is generally accepted that the electrical and thermal conductivity of the interdiffusion layer is quite low [18]. The U-Mo particles in the irradiated region are initially mainly in the γ-phase. In [4] it has been shown, that under the irradiation conditions of this experiment the remaining α–U-Mo transforms into γ–U-Mo – see also [2,17,19,20]. Furthermore it was shown by Bleiberg 1956 that γ-U-Mo transforms into a slightly more ordered phase which he called γ'. The electrical conductivity of γ'-U-Mo is about 3% higher than of γ-U-Mo [17].

The second region is the rest of the sample. Since this region is not hit by swift heavy ions only the increased temperature during irradiation can cause effects. No interdiffusion layer is expected to grow in this region [2]. Point defects inside of the Al matrix will anneal due to the increased temperature. A slight increase in electrical and thermal conductivity of the matrix would be the consequence. Most U-Mo particles exist in the γ-phase inside the non-irradiated part of the sample. This phase transforms to the α-phase when exposed to temperatures greater than 400°C [16]. The electrical conductivity of the U-Mo α–Phase is approximately 10% higher than the conductivity of the γ-Phase [17]. In case that the temperature during irradiation was to high it is possible that a phase change from γ– to α–phase inside the U-Mo particles took place. As a consequence there would be a significant increase in electrical conductivity of the U-Mo particles. With it comes an increase in electrical conductivity of the whole non-irradiated region.

During the bombardment with heavy ions competing effects on the conductivity of the samples occur. Thermal annealing and phase changes from γ– to α-U-Mo increase thermal conductivity, whereas irradiation creates point defects which principally decreases thermal conductivity. We conclude that at the here used total fluence and complex sample composition the net thermal conductivity can either increase or decrease.

The here used total fluence roughly simulates 1/10 of a typical burn-up of fuel in a research reactor. Future irradiations have to accumulate larger total fluences while controlling more precisely the temperature within the sample. It is expected to detect under these conditions a clear tendency in the changes of the thermal conductivity.

Acknowledgement

We would like to thank G.L. Hofman and C.R. Clark from Argonne National Lab for the provision with samples

References

[1] N. Wieschalla et.al., *Heavy ion irradiation of U–Mo/Al dispersion fuel*, Journal of Nuclear Materials, 357(1-3):191-197, 2006

[2] H. Palancher et.al, *Heavy ion irradiation as a method to discriminate research rector fuels*, Transactions of the RRFM 2006 – Sophia, 2006

[3] D.G. Walker, *The simulation of fission damage in U_3Si*, Journal of Nuclear Materials, 37:48-58, 1970

[4] N. Wieschalla, *Heavy ion irradiation of U-Mo/Al dispersion fue*l, dissertation at the TU-München, 2006

[5] R.P. Tye, *Thermal conductivity 1+2*, Academic Press London, 1969

[6] T.Z. Harmathy, *Variable-state methods of measuring the thermal properties of solids*, Journal of applied physics, 35(4):1190-1200, 1964

[7] P.H. Sidles and G.C. Danielson, *Thermal diffusivity of metals at high temperatures*, Journal of applied physics, 25(1):58-66, 1954

[8] V. Calzona et.al., *Fully automated apparatus for thermal diffusivity measurements on HTSC in high magnetic field*, Review of scientific instruments, 64(3);766-773, 1993

[9] V. Calzona et.al., *A new technique to obtain a fast thermocouple sensor for thermal diffusivity measurements in an extended temperature range*, Review of scientific instruments , 64(12):3612-3616, 1993

[10] W.J. Parker et.al., *Flash method of determining thermal diffusivity, heat capacity and thermal conductivity*, Journal of applied physics, 32(9):1679-1684, 1961

[11] C.K. Kim et.al., *Effect of particle shape and distribution on thermal and electrical conductivity in U_3Si-Al dispersion fuels*, Journal of nuclear materials, 209:315-320, 1994

[12] H.S. Carslaw and J.C. Jaeger, *Coduction of heat in solids*, Oxford Science Publications, 1959

[13] Rainer Jungwirth, *Thermische und elektrische Leitfähigkeit von hochdichten Uran-Molybdän-Kernbrennstoffen*, Diploma Thesis at the TU-München, 2006

[14] B.T. Kelly, *Irradiation damage to solids*, 1st edition, Pergamon Press, London, 1966

[15] T. Massalski, *Binary alloy phase diagrams*, ASM International, Ohio, 1996

[16] M.I. Mirandou et.al., *Rection layer in U-7wt%Mo/Al diffusion couples*, RERTR 2003, Chicago, 2003

[17] M.L. Bleiberg et.al., *Phase changes in pile-irradiated uranium-base alloys*, Journal of applied physics, 27(11):1270-1283, 1956

[18] S.L. Hayes et.al., *Modelling of high density U-Mo dispersion fuel plate performance*,RERTR 2002, San Carlos de Bariloche, 2002

[19] S.T. Konobevsky et.al., *Effects of irradiation on structure materials and properties of fissionable materials*, In Proceedings of the international conference on the peaceful uses of atomic energy/7, United Nations, New York, 1956

[20] K.T. Conlon et.al., *Neutron Powder diffraction of irradiated low-enriched Uranium-Molybdenum dispersion fuel*, RRFM 2006 – Sophia, 2006

CHARACTERIZATION OF MONOLITHIC FUEL FOIL PROPERTIES AND BOND STRENGTH*

D. E. BURKES, D. D. KEISER, D. M. WACHS, J. S. LARSON AND M. D. CHAPPLE

Nuclear Fuels and Materials Division, Idaho National Laboratory
P. O. Box 1625, Idaho Falls, ID, U. S. A. 83415-6188

ABSTRACT

Understanding fuel foil mechanical properties and fuel / cladding bond quality and strength in monolithic plates is an important area of investigation and quantification. Specifically, what constitutes an acceptable monolithic fuel – cladding bond, how are the properties of the bond measured and determined, and what is the impact of fabrication process or change in parameters on the level of bonding? Currently, non-bond areas are quantified employing ultrasonic determinations that are challenging to interpret and understand in terms of irradiation impact. Thus, determining mechanical properties of the fuel foil and what constitutes fuel / cladding non-bonds is essential to successful qualification of plate-type monolithic fuel. Capabilities and tests related to determination of these properties have been implemented and are discussed, along with preliminary results.

1. Introduction

Monolithic fuel forms are necessary to convert high power nuclear reactors that could not otherwise be converted by low density dispersion fuels. Development of these fuel forms is essential to the success of the Reduced Enrichment for Research and Test Reactors (RERTR) program. Based on the success of initial irradiations of monolithic fuel plates, an aggressive campaign to further fabricate, irradiate and qualify monolithic fuel has been developed [1]. However, challenges associated with the planar interface introduced by a monolithic fuel form still remain, in particular bonding between the fuel and cladding across the interface. Therefore, understanding bond quality and strength in monolithic fuel plates is an important area of investigation and quantification. Specifically, what constitutes an acceptable monolithic fuel – cladding bond, how are the properties of the bond measured and determined, and what is the impact of the fabrication process or change in fabrication parameters on the level of bonding?

1.1 Approach

Currently, potential non-bond areas can be identified by employing ultrasonic determinations. Determination of what constitutes an unbound area and to what degree this constitution is acceptable with high confidence is challenging and somewhat unknown. This challenge creates difficulties in drawing correlations observed in post-irradiation examinations (PIE) with pre-irradiation fabrication observations. A series of tests aimed at addressing the challenges associated with acceptable bonding behaviour determination in monolithic fuel plates is underway at the Idaho National Laboratory. Understanding the bond 'quality' in monolithic fuel is essential to the successful qualification of monolithic fuel plates. Two approaches have been identified and are being investigated to determine the level and quality of bonding in the monolithic fuel plates. The first approach is through characterization of the bond layer that is fabrication technique specific, i.e. friction stir welding (FSW), transient liquid phase bonding (TLPB) and/or hot isostatic pressing (HIPing). The second approach is through determining the irradiation performance of the fuel plates, allowing correlations between fabrication processes and post-irradiation examinations to be drawn.

* Work supported by the U.S. Department of Energy, Office of National Nuclear Security Administration (NNSA), under DOE Idaho Operations Office Contract DE-AC07-05ID14517.

1.2 Characterization

Ultrasonic testing (UT) has shown some promise in determining the location and degree of non-bond areas. UT is highly desirable in the fact that the technique is non-destructive and provides information on bond quality in an efficient manner. On the other hand, mechanical testing is desirable in the fact that the technique provides quantitative information on bond strength. There are two different types of mechanical testing that can be carried out: a non-destructive technique such as a proof test, or a destructive technique such as an instrumented tensile test and/or shear test. A non-destructive proof test is coupled with UT and consists of applying a known torsional force at the ends of the fuel plate with a defined cycle, analyzing the fuel plate for non-bond areas from UT, and repeating the proof test over until a defined size of non-bond defect appears. This type of testing would demand an extremely high confidence in the UT method. A destructive instrumented tensile or shear test is carried out on both well-bonded areas and suspected non-bond areas determined by UT, and is the subject of the current paper. Changes to fabrication process parameters or conditions, e.g. addition of a secondary interface such as a diffusion barrier, lower HIPing temperatures, etc., and the impact these have on bond strength will be more easily identified and understood prior to irradiation. Microstructural characterization is carried out in a similar manner as that defined for the destructive mechanical tests. Both suspected well-bonded and non-bonded areas are sectioned creating a metallographic specimen that is mounted, prepared and examined with optical microscopy and scanning electron microscopy (SEM). Any reaction layer existing between the monolithic fuel and the cladding is clearly visible and quantified in terms of thickness and composition (employing a semi-qualitative technique such as energy dispersive spectroscopy). The microstructural method is carried out in conjunction with the ultrasonic testing and mechanical testing, creating an ensemble of information relating to bond strength and integrity.

1.3 Irradiation Performance

The general irradiation performance evaluation of bonding in monolithic fuel plates is carried out in two basic areas: modelling and post-irradiation examination (PIE). Although the modelling approach is not discussed at this time, the approach consists of finite element analysis and analytical solutions relating to both thermal and thermo-mechanical aspects of the fuel-clad interface. Specifically, these models investigate the impact of a debond on the fuel meat temperature and stress behaviour, ultimately supporting determination of an acceptable debond size and geometry. The post-irradiation examination (PIE) approach involves examination of plates previously characterized by UT scans, pull tests and/or microstructural analysis after irradiation. Specific results on PIE of the latest monolithic fuel campaign (RERTR-6) may be found in Ref. [2]. Combination of these two approaches allows observations from irradiation to be fed back into fabrication to improve subsequent irradiation experiments, utilizing characterization as an effective means to understand how and what has changed in terms of bond strength and integrity.

2. Experimental Methods

Sample plates were fabricated employing one of three processing methods, hot-isostatic pressing (HIP), transient liquid phase bonding (TLPB) or friction stir welding (FSW). An updated description of each process can be found in Ref. [3]. All of the sample plates contained a DU-10Mo (nominal wt.%) foil approximately 8.26 cm long by 1.91 cm wide with aluminium-6061-T6 used as the cladding. HIP sample plates were subjected to 580^{o}C for ninety minutes at 103 MPa pressure. TLPB sample plates were subjected to 590^{o}C for fifteen minutes at 6.89 MPa pressure. FSW sample plates were welded with an approximate load of 17.8 kN and an unknown temperature, although the processing temperature is believed to be in the range of 400-500 C. Sample plates were subjected to ultrasonic testing to determine whether or not debonds were present. Regions of interest (ROI's) were determined from the UT scans and marked. Test specimens (ROI's) were sectioned from the sample plates using a low-speed saw. Each test specimen was a square approximately 0.876 cm on edge. One test specimen for each fabrication method was bound to aluminium test platens using a high strength epoxy. Bonding of the epoxy involves a heat treatment of 165^{o}C for ninety minutes after application. The low temperature heat treatment does not affect reaction kinetics or growth of an interfacial layer in a significant manner. Pull testing was carried out on the test specimens, similar to that used in determination of bond strength between thermally sprayed coatings and a substrate [4]. An in-house

test rig, shown in Fig. 1 along with a photograph of a mounted sample, was employed to carry out the pull tests. A constant crosshead rate was applied to pull the test while monitoring induced load with a tensile link load cell. A second sample from each fabrication method was cold mounted, polished using SiC paper and examined under a scanning electron microscope (SEM).

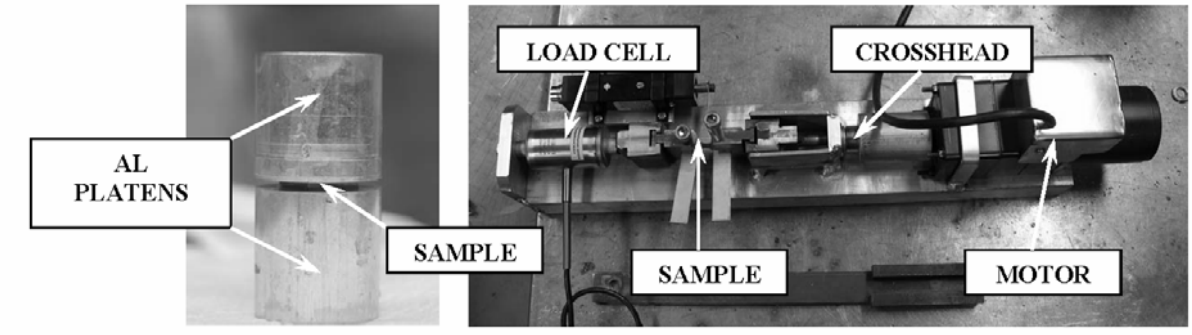

Fig. 1. Photograph of test rig employed to carry out pull tests. Pertinent features of the rig are pointed out

3. Results and Discussion

Ultrasonic testing scans of each sample plate are provided in Fig. 2. Regions of light [white] areas suggest acceptable bonding between the aluminium-aluminium cladding. Regions of light [grey] areas suggest acceptable bonding between the aluminium-fuel interfaces. Regions that appear dark in colour would suggest either a debond or inclusion/impurity in the fuel foil. However, observation of Fig. 2 reveals that this is clearly not the case for each of the sample plates fabricated using HIP, TLPB or FSW, and that each plate, based on this technique, has bonding between the fuel and cladding. Examples of SEM photomicrographs of the fuel-clad interface for each fabrication technique investigated are presented in Fig. 3. Observation of the photomicrograph for a HIP fabricated fuel plate reveals a relatively thin, uniform reaction layer, approximately 6 μm thick. The TLPB fabricated fuel plate contains a thicker (38 μm thick), non-uniform reaction layer that consists of multiple phases visible on the photomicrograph, i.e. regions A, B, C and D. Finally, the FSW fabricated fuel plate shows relatively no reaction layer at all.

Stress-time plots for each sample pull tested are provided in Fig. 4. The dashed line in the figure indicates the approximate limit (20 MPa) of the test rig, above which the crosshead is turned manually employing a wrench until failure of the interface or epoxy occurs. Observation of these plots show a steady increase in stress until catastrophic failure occurs. Samples are pulled normal to the fuel-clad interface. The HIP specimen profile reveals that the sample has bond strength of 60.3 MPa. However, failure of the epoxy occurred before that of the fuel clad interface, so that the actual bond strength, although unrealized in this plot, is greater than 60.3 MPa. An alternative test method, such as a peel test, will be used to quantify the bond strength of samples with strength greater than that of the epoxy. Currently, 60 MPa is established as acceptable bond strength, since no failures after irradiation have been observed with plates fabricated in this manner, at this time. The TLPB specimen has the second highest strength at 15.4 MPa, while the FSW specimen has the lowest bond strength at 6.42 MPa. Also observed from the stress-time plots is the significant difference in stress rate between the TLPB specimen and the HIP and FSW specimens. Since specimens are subjected to a constant rate up to the approximate limit of the test rig, variations in stress rate can provide some initial insight into the integrity of the as-fabrication reaction layer at the fuel-clad interface. The TLPB specimen has an approximate stress rate of 0.04 MPa•sec^{-1}, while the HIP and FSW specimens have approximate stress

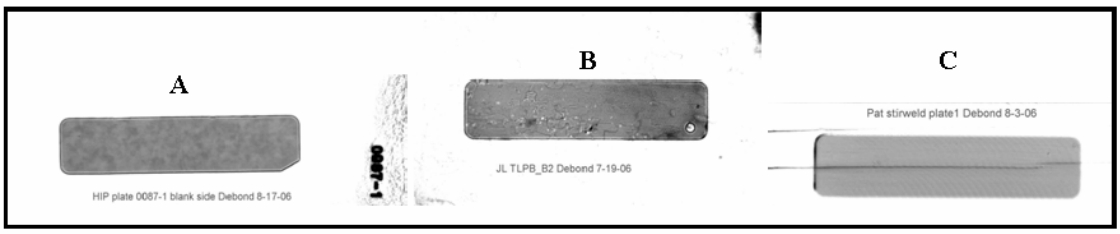

Fig. 2. Ultrasonic testing scans of (A.) HIP fabricated fuel plate, (B.) TLPB fabricated fuel plate and (C.) FSW fabricated fuel plate

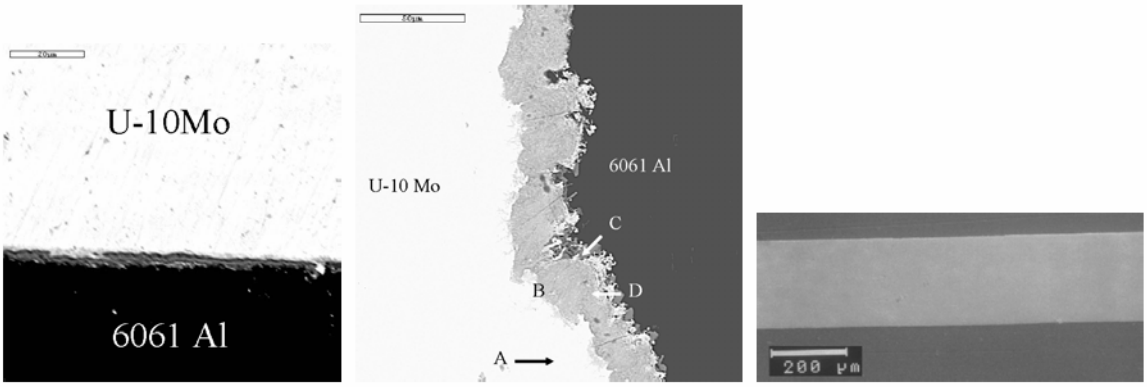

Fig. 3. SEM micrographs of the reaction layer formed from (left) HIP fabrication process, (middle) TLPB fabrication process and (right) FSW fabrication process

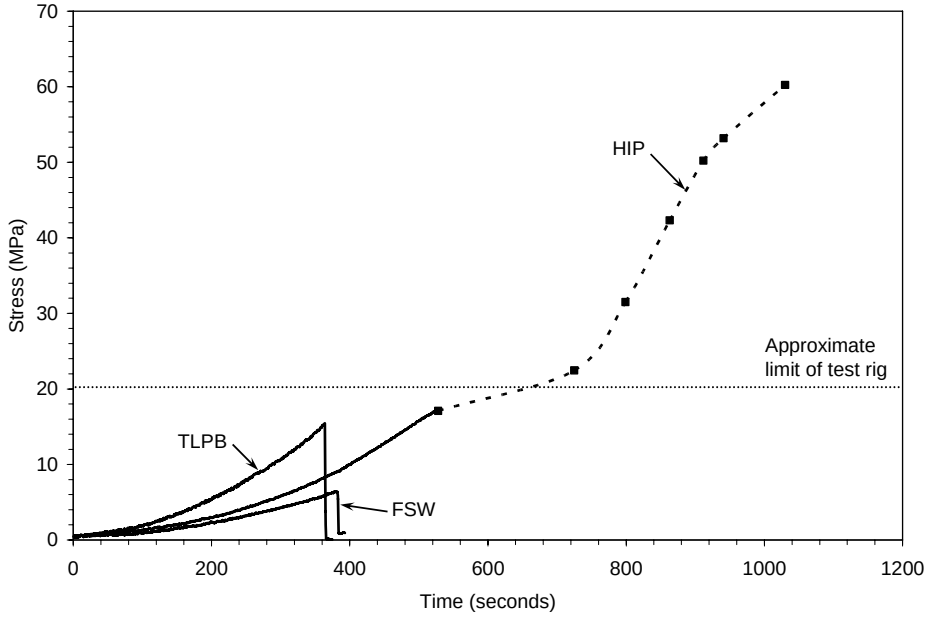

Fig. 4. Stress-time plots for test specimens obtained from pull test fabricated by each [HIP,TLPB,FSW] method

rates of 0.031 and 0.016 MPa•sec^{-1}, respectively. Hence, a hypothesis may be drawn that the eutectic formation of Al-12Si for the TLPB process behaves in a manner expected of a brittle intermetallic, i.e. high stress rate with sudden failure. In addition, this result appears to suggest that diffusion of aluminium into the foil is significant and results in a thick reaction layer, ultimately lowering the bond strength. Conversely, the FSW specimen has a low stress rate and low bond strength, suggesting that the bond is more mechanical than diffusional. This also seems intuitive since the weld tool has a low thermal conductivity compared to aluminium. Thus, as the FSW process progresses along the plate,

lower loads are applied in order to compensate for the increased temperature, i.e. heat builds up in the plate and is not conducted away from the weld face. Further increases in temperature would ultimately result in increased aluminium plasticity and promote void formation or disturbance of the monolithic fuel foil. The weld surface temperature can additionally be controlled by modifying the weld tool alloy. Increasing the thermal conductivity of the tool face has been shown to significantly increase the bond strength [5]. Finally, the HIP specimen shows the ideal trade-off between fabrication temperature and pressure, promoting diffusion of atoms across the fuel-clad interface resulting in bonding, but not to a degree where the brittle intermetallic nature of the bond dominates the behaviour.

4. Conclusions

The first series of mechanical characterization tests on monolithic fuel plates fabricated by hot isostatic pressing, transient liquid phase bonding and friction stir welding has been carried out. These tests allow a greater understanding of bond strength characteristics and performance prior to irradiation, so that improved correlations between fabrication processes, foil microstructure characteristics and post-irradiation properties can be determined, enhancing the success of the RERTR fuel development campaign. Initial results show that HIPed samples provide the highest bond strength while FSW samples, fabricated in the current manner, provide the lowest bond strength.

5. References

1. M. K. Meyer, “Status and Progress of the U. S. RERTR Fuel Development Program,” Proceedings of the 2005 International Meeting on Reduced Enrichment for Research and Test Reactors, Boston, USA (2005).
2. M. R. Finlay, D. M. Wachs, G. L. Hofman, “Post Irradiation Examination of Monolithic Mini Fuel Plates From RERTR-6,” Proceedings of the 2006 International Meeting on Reduced Enrichment for Research and Test Reactors, Cape Town, RSA (2006).
3. C. R. Clark, J. F. Jue, G. A. Moore, N. P. Hallinan and B. H. Park, “Update on Monolithic Fuel Fabrication Methods,” Proceedings of the 2006 International Meeting on Reduced Enrichment for Research and Test Reactors, Cape Town, RSA (2006).
4. ASTM Designation: C 633 – 01, “Standard Test Method for Adhesion or Cohesion Strength of Thermal Spray Coatings,” West Conshohocken, USA (2006).
5. D. D. Keiser, J.-F. Jue and D. E. Burkes, “Characterization and Testing of Monolithic RERTR Fuel Plates,” these proceedings, Lyon, FRA (2007).

SAFETY ANALYSIS OF A 1-MW POOL-TYPE RESEARCH REACTOR

T. Hamidouche[1], H. Mazrou[1], K. Ibrahim[1] & A. Bousbia-Salah[2]

[1] Laboratoire des Analyses de Sûreté, Centre de Recherche Nucléaire d'Alger, 02 Boulevard Frantz – Fanon, B.P. 399, 16000 Alger, Algérie.
thamidouche@comena-dz.org ; mazrou_h@comena-dz.org

[2] Dipartimento di Ingegneria Meccanica, Nucleare e della Produzione – Facoltà di Ingegneria, Università degli studi di Pisa. Via Diotisalvi, 2 - 56100, Pisa – Italy.
b.salah@ing.unipi.it

ABSTRACT

The following work is performed in view of gathering a better understanding of the behaviour of MTR pool type nuclear research reactors and in particular to present the results of the safety analysis of the 1-MW pool-type research reactor. The process followed passes through the determination of the inherent characteristics of the reactor core and by the analysis of some postulated initiating events considered in the safety analysis report (SAR) of this reactor.
The inherent parameters of interest which are: effective multiplication factor, kinetic parameters, feedback effects, power peaking factors and power defect, are calculated following two major steps. In a first step, cell calculations that consist of detailed models applied to different cell materials identified in the core, are performed by the commonly widely used ***WIMS/D4*** code. In a second step, core calculations consisting of global core model in two dimensional geometry are performed by ***MUDICO-2D*** diffusion code.
The accident analysis considered is related to the simulation of some postulated initiating events in two different core configurations of the same reactor. The purpose is to assess the dynamic response of the core and to investigate whether the cladding failure (melting) could be induced. To reach this goal, the in-house coupled thermal-hydraulic-point kinetic **RETRAC-PC** computer code was applied. The results obtained showed that the clad melting threshold is not reached over a wide range of transient situations even when the scram is disabled (unprotected transient). The importance of the inherent safety parameters of a reactor core under different configurations has been emphasized.
The ongoing is word is now oriented on the utilisation of **MCNP5** for criticality calculations and validation of the diffusion calculations performed so far and **RELAP5** code for transients and accidents analysis. The validation process of the codes as performed will be also presented in this paper.

1 Introduction :

The degree of consequences for any event postulated in safety analysis of a research reactor is determined by the response characteristics of the reactor system, which is a combination of non nuclear characteristics (like control systems) and inherent or intrinsic characteristics which are strongly nuclear.

In case of severe accidents, the sequence of events could be too rapid for effective control by external means and the course of the response will be firstly fully determined by the inherent characteristics also known as the self-limiting characteristics of the system. Therefore, in case of a power excursion event, the following observable parameters such as the power history shape, the self-limiting behaviour, the peak power, and the released energy should be checked.
In order to perform such a checking, certain intrinsic key parameters namely Prompt neutron lifetime Λ, Delayed neutron fraction β, Reactivity feedback coefficients, and Reactor control

systems, are important to understand the dynamic behaviour of the reactor core during any transient situation [1]. However, most of these key parameters are highly dependant upon the core configuration such as the lattice dimensions, the disposition of the fuel and control assemblies, the control systems, the reflector elements in the grid matrix …etc; Indeed, all these related configuration's data are used to determine the well known inherent core intrinsic parameters.

The first part of this work concerns the determination of some inherent characteristics of two different configurations of an MTR pool type research reactor: one configuration contains 16-fuel elements (C-16) and the other, 25-fuel elements (C-25) [2] and the second part of the work concern the analysis of some postulated initiating event using the key parameters calculated in the previous step and the importance of such inherent parameters are emphasized by considering the response of the two different core configurations during similar protected postulated initiating events. Furthermore unprotected cases as well as transients without feedback are also considered.

2 Key parameters of the core

2.1. Modelisation of the core:

The determination of the inherent characteristics of any given nuclear system passes throughout the use of some validated computer tools and techniques. For this purpose, a computer code package namely COMPACK-LHW [3, 4] has been developed for MTR research reactor applications. The individual modules of the package and the overall computational strategy along with the techniques of modeling used have been already assessed and qualified in a previous international benchmark problem [5-9].

In the following, the process of determination of the inherent characteristics of a 1 MW MTR (Material Testing reactor) pool type research reactor is outlined.

The computational procedure for the criticality analysis is performed in two main steps and is based mainly on two modules of the computer code system COMPACK-LHW. An adapted cell calculation version of *WIMS-D/4* code [10] provided with an updated 69-group LWR cross sections library and a locally developed diffusion MUDICO-2D computer code [11].

The first step, require a rigorous analysis of the reactor component by an identification of the different types of cells, which may represent physically any region of the core configuration taking into account the fuelled and non-fuelled regions of the core loading, along with the grid plate and the reflector assembly. Thus, in present case, cell calculations are performed using the WIMS-D/4 code for five (05) different identified and homogenized unit cell types of fuel and non-fuel elements present in the core.

In the second step, global core calculations with the locally two dimensional multigroup diffusion code MUDICO-2D are performed. Effective multiplication factor, reactivity feedback coefficients (Fuel temperature, moderator temperature and density/void coefficients), power peaking factors, power defect are then obtained. Perturbation calculations module of the code is used to evaluate kinetic parameters, like effective delayed neutron fraction and prompt neutron life time. The calculations of macroscopic cross sections for the fuel and non-fuel cells were carried out using 69 energy groups with collapsing procedures version. A 5-energy groups cut-off was adopted (See Table 1) for the following materials identified in the core:

1. Fresh fuel element;
2. H_2O – water reflector;
3. Graphite reflector;
4. Al+H_2O for the external region;
5. Stainless steel + H_2O for the external region in the control blade without absorber.

The broad group cross sections were also generated for different fuel temperatures ranging from 20°C to 150°C and for water temperature ranging from 20°C to 100°C and for change in water density. These cross sections were used to calculate the isothermal feedback reactivity coefficients. In addition, the excess reactivity values for the fresh core considered were also computed at different times of full power operating reactor using the diffusion theory model.

Table 1: Energy boundary for collapsed calculation

Group Energy	Energy range	WIMS - Groups
1	10.0 MeV – 0.821 MeV	1 – 5
2	821 KeV – 5.530 KeV	6 – 15
3	5.530 KeV – 0.625 eV	16 – 45
4	0.625 eV – 0.080 eV	46 – 55
5	0.080 eV – 0 eV	56 – 69

Fuel Element Model:

Fig. 1 shows the dimensions of the standard (SFE) and control fuel elements (CFE). Detailed specifications of the reactor are reported in the following reference [12]. The geometrical fuel model used in the following calculations is represented in Fig.2. Each standard fuel element is made of 19 fuel plates which is represented by two regions :

- The first region of dimensions (6.0 cm × 8.01 cm) represent the active zone of the fuel element;
- The second region with dimensions of (0.95 cm × 8.09 cm) represent two non-fuel (inert) region which consists of an Aluminium side plates and their associated water channels.

Fig. 3 shows the representative unit cell adopted and the associated dimensions used in WIMS-D/4 calculations for cross section generation of the fuel and non-fueled materials present in the reactor. The non-fueled region is represented by an "extra-region" which contains calculated volume fractions of Al and H_2O associated with each fuel plate, together with the water outside the assembly. The thickness of this extra-region was chosen to preserve the water volume fraction in the physical unit cell of each fuel assembly.

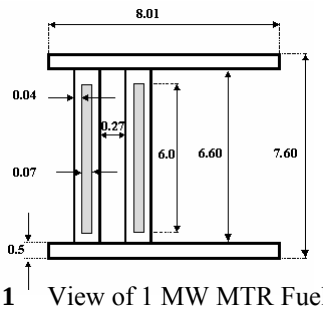

Fig. 1 View of 1 MW MTR Fuel Element (SFE and CFE)
(All dimensions are in cm).

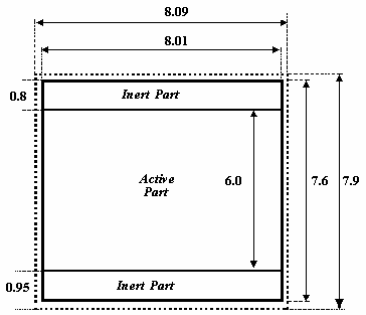

Fig. 2 Model of Standard Fuel Element (SFE).
(All dimensions are in cm).

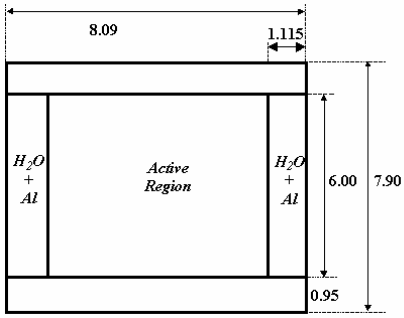

Fig. 3 Model of Control Fuel Element (CFE), without absorber.
(All dimensions are in cm).

CORE model

To evaluate the neutronics and safety parameters of the pool type reactor, and due to the geometrical asymmetry of the core configurations [13], a whole core simulation was performed using the MUDICO-2D two-dimensional multigroup diffusion code. The control rod channels were represented as H_2O + Al zones at both sides of the corresponding fuel elements. A total of 15 and 14 mesh intervals was used in the x and y directions respectively. The axial direction was represented with buckling of 1.64E-3 corresponding to a chopped cosine axial flux distribution with 8 cm reflector savings ($H_{extr.}$ = 77.5 cm). The following parameters were determined for the concerned configuration: Excess reactivity, prompt neutron generation time and effective delayed neutron fraction, fuel and coolant temperature, density feedback coefficient, void coefficient, power defect, and power peaking factors.

2.2 RESULTS

2.2.1. Excess reactivity :

The diffusion calculations for the supercritical core with the buckling of ($1.64\ 10^{-3}$) gave a k_{eff} value of ~ 1.05075, the experimental value of k_{eff} is 1.04302 [14].

The results should gradually be improved with adequate value of buckling. Thus, some additional and needed sensitivity studies should be performed in the future in order to decrease the difference between calculated and experimental k_{eff}.

2.2.2. Basic kinetic Parameters: (Λ, β)

The perturbation calculation module of the MUDICO-2D [11] code is used to evaluate basic kinetic parameters, namely effective delayed neutron fraction (β_{eff}) and prompt neutron generation time (Λ). The results obtained are as follow:

β_{eff} = 0.00765

Λ = 46.8 μ sec

2.2.3. Isothermal reactivity feedback coefficients :

- **Change of fuel temperature only:**

In order to determine the reactivity coefficient for fuel temperature, values of k_{eff} were computed for a fresh fuel at temperature **(T_F)** of 20°C, 50°C, 75°C, 100°C and 150°C. The deviations of the reactivity to a reference value at 20°C are given by equation (1):

$$\Delta\rho = \rho\ (T_F) - \rho\ (20°C) \qquad (1)$$

The best polynomial fit of the reactivity variation Δρ (in pcm=10^{-5}) for the studied case is given in terms of fuel temperature ($\mathbf{T_F}$) by:

$$\Delta\rho \text{ (pcm)} = 45.870 - 2.064\ T_F \qquad (3)$$

It's interesting to note that for the normal operating range of the reactor, this coefficient remains negative.

- **Change of water temperature only:**

Values of k_{eff} were computed for water temperature **(T_W)** of 20°C, 30°C, 40°C, 60°C and 80°C. Cross sections libraries at these different temperatures are obtained from WIMS-D4 cell calculations and are used by MUDICO-2D to calculate k_{eff} corresponding to each of these temperatures. The best polynomial fit of the reactivity variation Δρ (in pcm) for the studied case is given by:

$$\Delta\rho \text{ (pcm)} = 159.890 - 7.970\ T_W \qquad (4)$$

- **Change of Water Density only :**

Values of k_{eff} are computed for water densities of 0.998, 0.996, 0.992, 0.983, 0.969 and 0.958 g/cm^3, which correspond to water temperature of 20°C, 30°C, 40°C, 60°C, 80°C and 100°C. The reactivity changes are calculated to reference reactivity at 20°C.
The best polynomial fit representing this variation for the studied core is given by:

$$\Delta\rho \text{ (pcm)} = 125.297 - 5.611\ T_W - 0.087\ T_W^{\,2} \qquad (5)$$

- **Core Void Coefficients:**

To obtain core void coefficients **(α_v)**, the water concentration change was considered in both moderator and extra-region of the unit cell. The reactivity changes are calculated to reference reactivity at 20°C and for void conditions of 5%, 10%, 15% et 20%. This case, which seems to be a realistic one, is represented by the best polynomial fit obtained as:

$$\Delta\rho \text{ (pcm)} = -17.52 - 294.5\ \alpha_v - 4.79\ \alpha_v^2 \qquad (6)$$

The global results obtained for the temperature coefficient of reactivity for the studied critical core configuration over the temperature range of 20 – 80 °C are summarized in table 2. Also is shown in this table, the core void coefficient of reactivity due to change in water density from 0.948 – 0.80 g/cm^3 and from 0.998 – 0.948 g/cm^3.

- **Power Defect of Reactivity :**

The power defect of reactivity which is an important parameter for reactor operation is defined as the total of all reactivity effects induced by bringing the reactor from cold zero-power conditions to normal operating conditions. Thus, taking into account the different temperature conditions, the loss of reactivity between zero and full power is given by:

$$\Delta\rho_{power} = \left(\alpha_{T_W} + \alpha_{D_W}\right)\overline{\Delta T_W} + \alpha_{T_f}\,\overline{\Delta T_f} \qquad (7)$$

α_{Tw}, α_{Dw} and α_{Tf} are the temperature coefficients of reactivity defined in table 2 and $\overline{\Delta T_w}$ and $\overline{\Delta T_f}$ are the mean temperature differences in the water and in the fuel from cold zero-power conditions to normal operating conditions.
In the case of interest with an inlet coolant temperature of 40°C and a flow rate of 220 m3/h, the mean temperature difference between zero power and full power is calculated to be around 3.5°C in the water and about 11.1°C in the fuel meat [15]. Table 3 shows the water, fuel and total reactivity

differences between zero and full power computed using isothermal reactivity coefficient calculated above for the temperature range 20-80°C.

Table 2 : Isothermal Reactivity Coefficients

Effect	LAS*
Temperature Range: 20 – 80 °C ($-\Delta\rho/°C \times 10^{+5}$)	
Fuel Temperature only: α_{Tf}	2.13
Water Temperature only: α_{Tw}	7.93
Water Density only: α_{Dw}	14.52
$\alpha_{Tw} + \alpha_{Dw}$	22.45
Water Density Range: 0.948 – 0.80 g/cm^3 ($-\Delta\rho/\Delta\rho_w$)	
Void Coefficient (%): α_v	41.8
Water Density Range: 0.998 – 0.948 g/cm^3 ($-\Delta\rho/\Delta\rho_w$)	
Void Coefficient (%): α_v	32.8
* LAS: Laboratoire des Analyses de Sûreté, CRNA.	

- **Power Peaking Factors :**

The peaking factor, being the most important safety parameter, was also evaluated. This factor is defined as the product of three factors: radial x local x axial, peaking factors.

The radial power peaking factor is defined as the ratio of the average midplane power in a specified element to the average midplane power in the core.

The local power peaking factor is defined as the ratio of the maximum midplane power to the average midplane power in the specified element.

The axial power peaking factor is defined as the ratio of the maximum axial power to the average axial power in the specified element.

Two-dimensional diffusion calculations were performed by MUDICO-2D for all the fuel elements present in the core. Since the maximum wall or clad temperature is the limiting operational parameter of the core, the peaking factor of greatest importance for steady state operation is the maximum of this product (radial x local). Thus, the results are as follow:

F_{rad} = 1.32

F_{loc} = 1.09

The axial power factor was determined, assuming a chopped cosine flux distribution along the channel. Then, we obtain the following value:

F_{axi} = 1.32

The total peaking factor is the product of these three parameters ($F_{TOT} = F_a \times F_r \times F_l$) :

F_{TOT} (conf.-16) = 1.90

This parameter is very important as well as, for steady state operation and for extreme hypothetical accidents, since it determine the maximum energy released in the hottest fuel element and consequently give us the corresponding peak fuel temperature and the peak cladding temperature which is as outlined before an important limitation safety parameter.

The total peaking factor calculated implies that under extreme conditions, the maximum of heat generation in the hottest fuel element is almost two times higher than that generated in the average fuel element of the core.

Table 3 : Power Defect of Reactivity

$\overline{\Delta T_w}$ **= 3.6 °C** $\overline{\Delta T_f}$ **= 11.1 °C**

Effect	**LAS**
Fuel Temperature (pcm)	23.6
Water Temperature + Density (pcm)	80.8
$\Delta\rho_{\text{ power}}$ (pcm)	104.5
β_{eff} (%)	0.765
$\Delta\rho_{\text{ power}}$, ¢ (cents)	13.7

3 Accident analysis

3.1. Description of scenarios

Two different types of initiating events are considered as fellows

Case 1: Rapid (kinetic) transient initiated by a positive Reactivity Induced Accident (RIA); this postulated event is initiated by an hypothetic control rod withdrawal at start-up when the core power level was at 1W and the coolant inlet temperature at 40°C;

During RIA events a non-equilibrium between the generated and the removed heat takes place. Consequently, the core component's temperature rise up and their integrity could be damaged in absence of appropriate response of the control systems. The transients under consideration herein are initiated by a super prompt insertion of a positive reactivity of \$1.5 in 0.5 seconds. This transient occurs at reactor startup and the reactor power level was assumed to be 1W; the circulating pumps are assumed to assure full upward cooling flow.

In case of the analysis of protected transients, the safety setting overpower trip point is set to 1.2 MW i.e. the scram system is acted when the power level reach the setting trip point above. This shutdown mechanism introduces a negative reactivity of -\$8 in 0.5 sec with a response delay time of 0.025 s.

Case 2: Relatively slow transient cases related to Loss of core coolant Flow Accident (LOFA) as a consequence of main cooling pump failure when the reactor was operating at its nominal power level and the inlet temperature was 40°C.

Both protected (with scram) and unprotected transients (without scram) are considered.

During a loss of flow accident or LOFA, we can expect a core heat up due to malfunction of the cooling system. To simulate this postulated initiating event, the flow decrease is modeled by an exponential decrease function (exp(-t/T)). The period T is set equal to 1 sec in case of a Fast LOFA (FLOFA) and equal to 25 s in case of a Slow LOFA (SLOFA).

These transients are initiated when the reactor was operating at its nominal power level of 1.2 MW with cooling system allowing full downward cooling flow.

For the protected cases, the reactor scrams is set by a trip point that enable a shutdown reactivity insertion when the flow rate is reduced by 15% of its nominal value; the scram is acted with a delay time of 0.2s.

The basic kinetics parameters and isothermal reactivity feedback coefficients for these two configurations (C25 and C16) of the equilibrium cores summarized in Table 4 [2].

Table 4 : Kinetic and reactivity feedback parameters

Parameter	**25 Fuel elements**	**16 Fuel elements**
Effective Delayed neutron fraction β_{eff}	0.00769	0.00765
Generation Time Λ, μs	46.80	46.80
Mean Void reactivity coefficient,$ / %	0.8128	0.512
Mean Fuel Temperature feedback coeff $/°C	$2.773\ 10^{-3}$	$2.58\ 10^{-3}$
Mean Coolant Temperature feedback coeff $/°C	$3.084\ 10^{-2}$	$3.226\ 10^{-3}$

3.2. Reactor Core modeling and computer codes:

In order to simulate the reactor dynamics under the aforementioned initiating events, the reactor is modelled by one unit cell that represents any heated region of the core. Three regions compose this representative cell: fuel-clad and the associated coolant channel.
In this model, a cosine axial power distribution is assumed with a cosine shape set to 1.311; the overall peak/average as calculated above is applied for the hot channel.

3.3. Computer codes used:

- The RETRAC-PC Code [16] is used to perform a numerical simulation of the considered transients. The core power history is derived through the resolution of the point kinetic equations coupled to the thermal hydraulic conservation equations of mass, momentum and energy conservation. In this code feedback contribution due to coolant and fuel temperature changes and void are considered with the possibility to assign separate reactivity coefficients for each component (see Table 4).
- The PARET Code [17] which is similar to RETRAC-PC, is a channel code based on a coupling of kinetic equations, heat conduction and hydrodynamic equations with adjusted feedback. This code has been extensively compared with the SPERT experiments [18]. These comparisons have shown quite good agreement for a wide range of transients including melting of the clad. The PARET code has also been used by the RERTR (Reduced Enrichment for Research and Test Reactors) Program for the safety evaluation of many research reactors candidates for fuel reduced enrichment [19]. According to the good performances shown by PARET, the RETRAC-PC results are compared to PARET ones in order to appreciate the relevant results.

3.4.Results :

3.4.1. RIA Transients:

a. Protected transients:

The power, the clad maximum temperatures and the coolant outlet temperatures histories as obtained by RETRAC-PC and PARET are presented in the fig.s 4 and 5 respectively. The compensated reactivity is also provided in fig. 4. The main transient parameters are summarized in Table 5 for both configurations.
As shown on fig. 4, the power behavior exhibits, as could be expected, an exponential excursion. The trip setting point by power (P_{trip}=1.2 MW) is reached few milliseconds after the initiation of the accident. However, the power increase continues during the lag time before effective action of the scram system (due to time response delay of 25ms); this scram system delay response enable the power to reaches almost 50 MW as shown in Table 5. But, in case of unprotected transients, the power reaches very high levels as could be observed in Table 6.
We can notice quite similar responses of both configurations for protected transients especially during the lag time before peak power is reached (see Fig. 4). Indeed, in this kind of transients, the dynamic response of the core is governed essentially by the prompt neutrons and the inherent

feedback mechanisms do not act significantly during this first stage of the transient. This is confirmed by the delay response of the thermal hydraulic mechanisms that induces a beginning of temperatures rises later after the power trip point (see Fig. 4 for example). As a consequence, the feedback effect begins to act slightly just after the trip point and contribute to reduce the power excursion period. Their effect becomes insignificant after the reactor scram. However, we should mention here that some voids production is predicted to occur around the peak power time occurrence. This phenomenon contributed strongly in reducing the power excursion; the void production begins when the clad temperature exceeds 126°C which correspond to the onset of nucleate boiling temperature threshold as calculated by the Bergles-Rhosenow correlation.

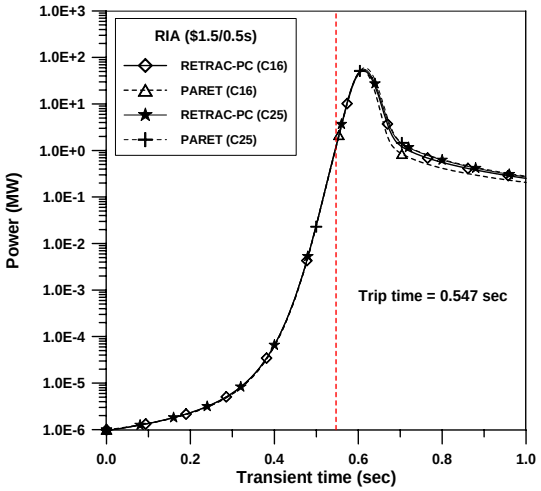

Fig. 4 : Power behavior during RIA transient (C16 and C25 configurations)

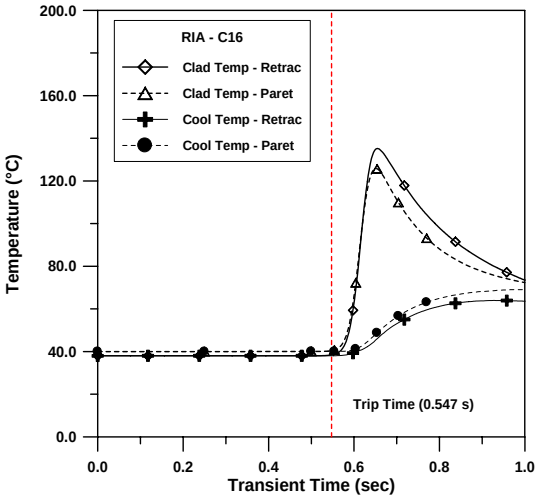

Fig. 5 : Cladding and Coolant Temperature behavior during RIA transient (C16 configuration)

As mentioned above, the PARET code has been also used to simulate the core behavior during protected RIA. As outlined on fig. 4 and Table 5, the two codes showed in general similar results. The observed discrepancies, as well explained in a previous work [20], are essentially due to the feedback model (essentially the void effect) and to the amount of heat directly transferred to coolant without convection.

Table 5. Transient Parameter for protected RIA

Parameter \ Configuration	C 16		C25	
	RETRAC-PC	PARET	RETRAC-PC	PARET
Trip time (sec)	0.547	0.547	0.546	0.547
Peak Power (MW)	51.676 (0.612)	51.756 (0.611)	57.325 (0.613)	60.087 (0.616)
Energy at Peak power (MJ)	1.41	1.37	1.59	1.67
Peak Fuel Temperature (°C)	157.60 (0.640)	150.60 (0.635)	146.86 (0.644)	142.73 (0.643)
Peak Clad Temperature (°C)	135.22 (0.654)	125.83 (0.651)	131.62 (0.661)	120.66 (0.659)
Coolant Temperature (°C)	63.93 (0.928)	63.47 (0.985)	63.97 (0.999)	70.60 (1.170)

()time of occurrence in seconds

b. Unprotected transients:

In order to emphasis the strong effect of feedback mechanism and to outline the key parameters that govern the inherent dynamic response of the cores, similar RIA as above but without scram are considered. The C-16 clad temperature and the power excursion under these conditions (without scram) are shown on fig. 6 and 7 with comparison to the similar parameters corresponding to case with scram.

In case of no scram, the power continues its excursion until it is stopped by the inherent feedback's mechanisms of the reactor. For this case, the power reaches a maximum of 150 MW and quenches due to the strong feedback effect even the scram system is disabled during the course of the accident. No damage of the cladding occurs according to the results shown in Fig. 7. The maximum temperature reached (less than 186°C) is far below the melting point of aluminium that is 600 °C or even from the safety margin of 450°C fixed due to swelling of Aluminium.

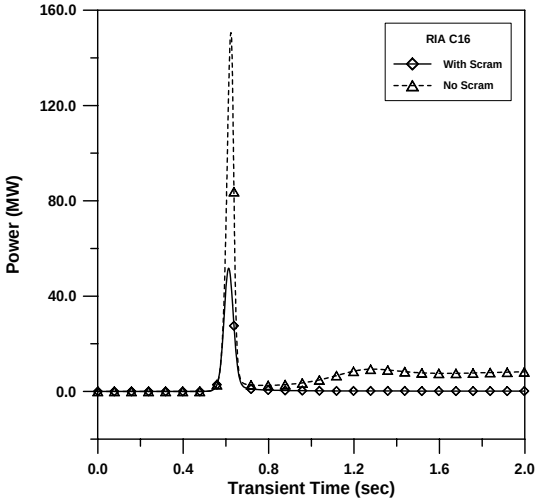

Fig. 6 : Power behavior during RIA transient with and without scram (C16 configuration)

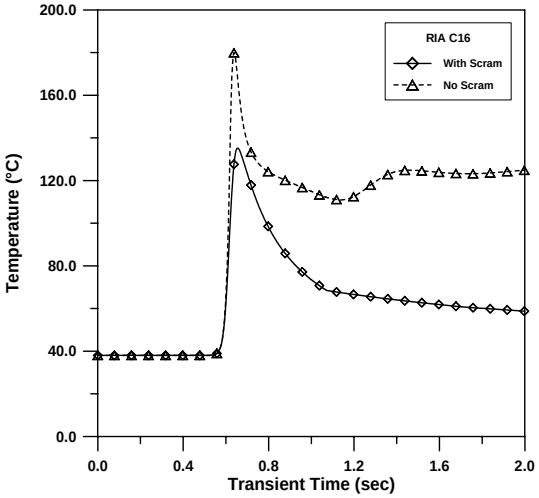

Fig. 7 : Cladding temperature behavior during RIA transient with and without scram (C16 configuration)

Furthermore, the strong influence of the feedback mechanism on the stability of this research reactor are emphasized in the following by investigating the reactor response under protected RIA (with scram) but in absence of any feedback mechanisms. The results obtained in this case are summarized in Table 6 and the power excursion is reproduced on fig. 8 with a comparison to the reference case (in 3.4.1-a). The power excursion for both cases is similar until the trip point (1.2MW) but after this point and under the new assumptions (no feedback), the power continue to increase and reaches 132 MW (instead of 52Mw in previous case) before the control system could stop the excursion. These results emphasize what has been stated in previous sections concerning the strong feedback effects on the excursion runaway before any effective scram. This exercise confirms also the importance of these inherent core parameters for the safety of the considered reactor (self shut-down).
Also, in fig. 8, one can observe a failure of the code after 0.67 seconds because of the limitation of the thermal hydraulic model that can not handle, at this stage of development, the transition from single to two phase convection.

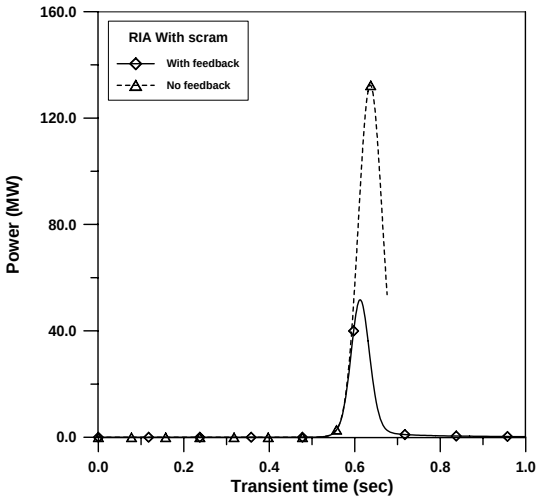

Fig. 8 : C16 response to RIA accident with and without feedback (scram enabled)

Table 6. Transient Parameter for unprotected RIA

Parameter \ Configuration	C 16		C25	
	No scram	No feedback	No scram	No feedback
Trip time (sec)	0.547	0.547	0.546	0.546
Peak Power (MW)	150.64 (0.623)	132.41 (0.636)	182.18 (0.624)	135.65 (0.636)
Energy at Peak power (MJ)	3.69	4.71	4.55	4.80
Peak Fuel Temperature (°C)	308.04 (0.634)	324.91 (0.653)	294.52 (0.635)	284.36 (0.655)
Peak Clad Temperature (°C)	180.01 (0.638)	185.96 (0.658)	181.01 (0.640)	180.93 (0.660)
Coolant Temperature (°C)	106.16 (0.849)	104.58 (0.672)*	104.64 (0.979)	109.17 (0.700)*

*()time of occurrence in seconds * time of end o f calculations*

Conclusion :

Through the present study, the overall strategy followed for the analysis of reactivity accidents in an MTR research reactor was outlined. This process passes through two major steps which are the characterization of the reactor core (key parameters) and the simulations of the postulated events.

However, in order to evaluate the uncertainties of the criticality calculations, an additional assessment of this procedure and the computer tools used will be handled, in a near future, by comparison with analytical results from Monte-Carlo calculations.

From the analysis of the postulated events considered here, it appears that the clad melting threshold is not reached over a wide range of transient situations even when the scram is disabled (unprotected transient).

The importance of the inherent safety parameters of a reactor core under different configurations has been emphasized and the investigation has confirmed the strong influence of the inherent parameters (or key parameters) on the core dynamics under transient or accidental situations. However more detailed simulations should be considered in order to confirm the aforementioned conclusions. This could be done by applying best estimate computational tools that are able to take into account the multidimensional kinetics and thermal-hydraulic effects [22].

REFERENCES:

[1] Duderstadt J.J and Hamilton L. J.: ‘‘Nuclear Reactor Analysis’’, John Willey & Sons, IncPhD Thesis, University of Pisa, Italy, 2004.

[2] Mazrou H. et al, “Calcul neutronique du réacteur de recherche NUR, 1ère Partie : calcul statique’’, Private communication, 1999.

[3] Mazrou H., Hamidouche T., Ibrahim K. and Bousbia-Salah A.: “Development of a system of computer codes for the safety analysis of nuclear research cores”, Progress report, IAEA Contract Research Project CRP-ALG-9758, 1998.

[4] Mazrou H., Ibrahim K. and Hamidouche T. : “Méthodes de calcul neutronique d’un réacteur de recherche du type M.T.R.”, SPRUA’98 CDSE/Ain-Oussara/ 02-04 Novembre 1998.

[5] Baggoura B., Hamidouche T. & Bousbia-Salah A.: "RETRAC-PC: A program for the analysis of Material Test Reactor", Nuclear Science Engineering, vol.118, Sept 1994.

[6] Baggoura B. & Ibrahim K., "CRTA: A computer program for transient analysis in light water research reactors", Nuclear Science Engineering, vol.118, Nov. 1994.

[7] Ibrahim K., Hamidouche T. and Mazrou H.,: "IAEA-10 Mw Benchmark reactor safety analysis with CRTA space time diffusion code " First AFRA Regional Conference on Research Reactor Operation, Safety and Utilization; AFRA IV/12 10-12/04/99. (contributed paper – session 3)

[8] Bousbia-Salah A., Hamidouche T., Mazrou H. & Ibrahim K.: "Dynamical calculations for the IAEA safety related benchmark problem using RETRAC-PC Code", Algerian Review of Nuclear Sciences – ARNS Vol. 4, No. 2 (2002) 95-103.

[9] Mazrou H., Hamidouche T., Ibrahim K. and Bousbia-Salah A., "Computer code package COMPACK-LHW for M.T.R. research reactor core calculations", International Conference on the New Frontiers of Nuclear Technology: Reactor Physics, Safety and high-performance Computing. PHYSOR 2002, October 7-10, 2002, Seoul (Korea), ISBN 0-89448-672-1, CD-ROM.

[10] Askew & al., WIMS/D4 : A general description of the lattice code WIMS, UKAEA, 1967.

[11] Ibrahim K., Mazrou H., Hamidouche T. and Benkharfia H., « MUDICO-2D: A Two-Dimensional Multigroup Diffusion Code for Perturbation Calculation in Light Water Research Reactors ». Proceedings of International Conference on the New Frontiers of Nuclear Technology: Reactor Physics, Safety and High-Performance Computing. PHYSOR 2002 October 7-10, 2002, Seoul, Korea, ISBN 0-89448-672-1, CD-ROM.

[12] International Atomic Energy Agency Technical Document: "Directory of Nuclear Research Reactors", IAEA STI/PUB/983, ISBN 92-0-105494-7, 1995.

[13] Blizak s. and meftah b.: "Nuclear heating analysis in irradiated single silicon ingots at research reactors", Algerian Review of Nuclear Sciences – ARNS Vol. 3, No. 1&2 (2001) 99-110.

[14] Meftah b. et al. : "Evaluation of pertinent safety parameters and transients behavior in the NUR research reactor", Progress report, IAEA Contract Research Project CRP-8786/RB, 1996.

[15] Hamidouche T., Mazrou H., Ibrahim K. and Bousbia-Salah A.: "Analyse d'accidents du réacteur nucléaire de recherche NUR", Internal report, CRNA-2000.

[16] Hamidouche T., Bousbia-Salah A., Mazrou H. & Ibrahim K. "RETRAC-PC: A computer program for safety analysis of research reactors", International Conference on the New Frontiers of Nuclear Technology: Reactor Physics, Safety and high-performance Computing. PHYSOR 2002, October 7-10, 2002, Seoul (Korea), ISBN 0-89448-672-1, CD-ROM, 2002

[17] Woodruff W. L.: "A Kinetics capability for the Analysis of Research Reactors", Nuclear Technology, 64, 196, 1984

[18] Obenchain C. :"PARET: A Program for the Analysis of Reactor Transients", AEC Research and Development Report IDO-17282, Phillips Petroleum Company, 1969.

[19] In Proceedings of "International Meeting on Reduced Enrichment for Research and Test Reactors'', www.rertr.anl.gov

[20] Bousbia-Salah A., Hamidouche T., Mazrou H. & Ibrahim K.: "Dynamical calculations for the IAEA safety related benchmark problem using RETRAC-PC Code", Algerian Review of Nuclear Sciences – ARNS Vol. 4, No. 2 (2002) 95-103.

[21] Lewis E. E.: "Nuclear Power Reactor Safety''; A Wiley Interscience Publication, John Willey & Son, 1977.

[22] Bousbia-Salah A.: ''Overview Of Coupled System Thermal-Hydraulic 3D Neutron Kinetic Code Applications'', PhD Thesis, University of Pisa, Italy, 2004.

OSCAR-3 MCNP INTERFACE (OSMINT5) VERIFICATION AND VALIDATION

M. BELAL, A.L. GRAHAM, DAWID DE VILLIERS
Radiation & Reactor Theory, Necsa
P O Box 528, Pretoria 0001 – South Africa

ABSTRACT

OSMINT5 has been developed to set up a SAFARI-1 MCNP model by detecting the whole core configuration and isotopic inventory from OSCAR-3. Its flexibility allows various models, enabling OSCAR-3 comparisons, OSCAR-3 coupling approximation studies, application to OSCAR-4 (reserved), and an exact model, to be used for predicting neutronic parameters and for design purposes.
Using MCNP-Os3 (MCNP – OSMINT – option 3) to compare with OSCAR-3 has shown a difference on average with OSCAR-3 of 1.316% when the bank position is inside an axial node and .997% when the bank position coincides with an axial mesh. The average difference with measurements is -1.765%; however, MCNP-Os5 (MCNP - OSMINT - option 5) comparisons have shown good agreement (0.10813% on average) with measurements in predicting the critical bank position.
Along within the validation process of MCNP models generated with OSMINT, this paper presents a complete analysis of the global core reactivity variation associated with the modelling, and of the modifications accordingly implemented.

1. Introduction

OSCAR-3 is a nodal diffusion code, used to perform SAFARI-1 reactor core follow and safety analysis. As a result of the approximations of nodal diffusion theory, it was necessary to build an automatic tool to run in parallel with OSCAR-3 to provide comparisons, and by using core snap shots to generate MCNP models as input for measurement comparisons and design purposes.
The first stage of the project was to generate MCNP inputs at different time snap shots with isotopics treated explicitly and with approximate core models (MCNP – Os3) [1], with results referred to in the conclusions. The second stage, which is presented in this paper, is to set up detailed modeling, with the rest of isotopes not available in the current MCNP nuclear data libraries (Sm-148), and detailed geometry (MCNP –Os35 and MCNP – Os5) and to analyze the approximate MCNP-Os3 results; these could be taken into account to build the detailed geometry model MCNP-Os5. A complete verification of OSMINT as a tool capable of fulfilling its purposes was necessitated, and future requirements were formulated. The validation of the MCNP model generated and of the modeling options to represent the SAFARI-1 core, is presented in this paper, as well as the validation of MCNP input generated with different modeling options.
The next stage will be to generate fission products as spatial and burnup dependent lumped fission product (LFP) cross sections, resulting in an MCNP model that is more representative of a burned core; in addition, integrated codes will be developed to perform the parallel core follow, fuel management and the optimization of ^{99}Mo production.
The ability of OSMINT to set up a valid MCNP model of the SAFARI-1 core, for any burnup case as supplied from OSCAR-3 was verified. Once the generated MCNP-SAFARI-1 core model had been verified, the validation process was performed in order to establish the range of uncertainties for predicting the core neutronic parameters.
However, in order to validate the MCNP model for SAFARI-1, MCNP calculation results are compared with validated results from OSCAR-3 to establish relative uncertainty margins, besides ongoing comparisons with measurements.

2. OSMINT Verification

The verification process of OSMINT mechanics includes the following steps:

1. Isotopic transfer.
2. Check the cell volumes and material masses as calculated with OSMINT and MCNP.
3. Visual check of the core layouts by means of horizontal and vertical cuts.
4. Check that all outputs of OSMINT (1.e., MCNP inputs) are executable without any user modifications, in order to meet the requirements of a future upgrade to a parallel Monte Carlo core follow and fuel management system.

3. Additions to OSMINT.061t

The following capabilities and modifications were made to OSMINT test version [1].061t during the verification process:

3.I) In order to verify the mechanics of OSMINT, some additions were implemented, with the result that the verification process will be part of every OSMINT execution.

3.II) As SAFARI-1 is in the process of converting from HEU to LEU, the ability to handle LEU as well was added to OSMINT.

Note: during each execution of OSMINT, a complete verification of geometry volumes, isotopic IDs, isotopic masses per assembly and in the whole core is performed and reflected in OSMINT output file.

3.III) The ability to handle Mo target plate irradiation rigs with different combinations of fuel and/or dummy aluminium plates. In the OSMINT.i input file, the user enters the number of rigs, and for each rig, the combination of fuel/dummy-Al plates.

Shown below is part of the OSMINT input file for target plate specification, where the user enters 1 for fuel and 0 for dummy-Al per rig.

```
Molly Control -
Number of Molly devices          : 6
Insert 1/0 fuel/dummy-Al
combination for each Molly
                                 B8    : 1 0 1 0 0 1 1
                                 C3    : 1 1 0 0 0 1 1
                                 D8    : 1 0 0 1 0 1 1
                                 E3    : 1 1 0 0 1 1 1
                                 F8    : 1 0 0 0 0 1 1
                                 G3    : 1 1 0 1 1 1 1
```

The volume fraction is calculated according to the user-specified fuel/dummy combinations.

3.IV) To set up MCNP models representing the following cases:

1. ver = 3 (MCNP-Os3) , model representing OSCAR-3, with: a. Exact active core length 59.37cm. b.Control follower is not represented beneath the core active length (in reflector). c. Bank positions provided from OSCAR-3 handled. d. Cd section presented above the core in cases where the bank position is more than 0 notches. e. Generic Mo target plate modelling (inside 4 nodes) with the thimble extending above and below the rig up to active core length only.
2. ver = 35 (MCNP-Os35), same as above, but splits the bank positions provided to form the coupling part in order to study its approximation in OSCAR-3, as shown below;

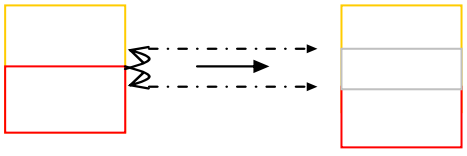

OSCAR-3 MCNP

3. ver = 5 (MCNP-Os5), Exact core model as above, but: a. Control follower extending beneath the core active length. b. Exact models of rig and thimble. c. Bank positions provided are handled as shown below, taking into account that the setting exact models from SAFARI-1 are at the lower tip of the Cd.

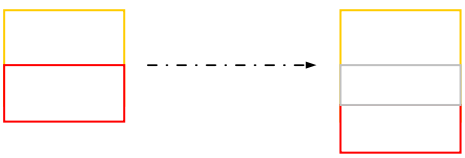

OSCAR-3 MCNP

4. Validation

4.1 Case I (MCNP-Os3)

Case I shows the results of a recent core during the core follow calculations with OSCAR-3. After comparing results from OSCAR-3, MCNP and measured values, a comparison also took place with the same core and different control bank settings, in order to study the effect of control rod modelling. The plate combinations in the Mo production rig were obtained from the Mo Irradiation Planning [4] documentation, where the case study is performed for the core at 15.993 days into the cycle.

4.2. Results and Discussion

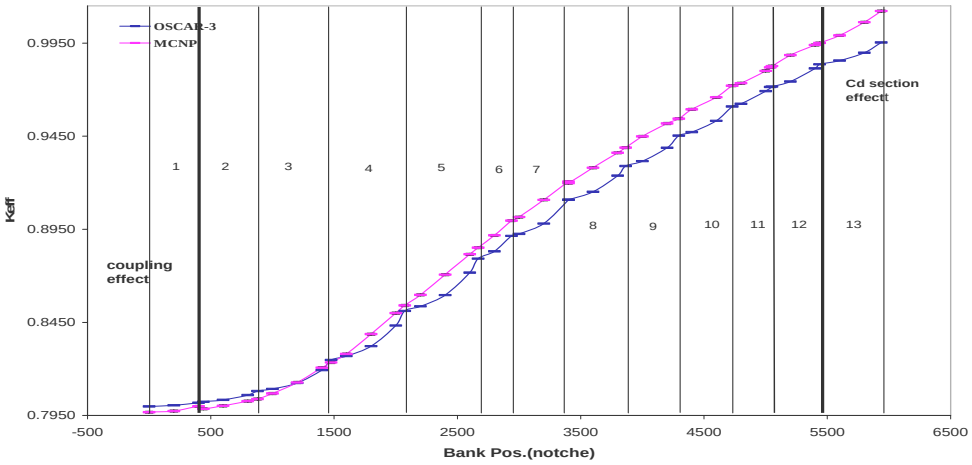

Fig 2. Core reactivity with banks withdrawal position, vertical lines represent the axial nodes tip of nodes numbered from 1 to 13, bottom to top respectively (MCNP-Os3)

Criticality comparisons have been performed, where the difference between OSCAR-3 and MCNP was -1.132%, and the uncertainty in predicting the criticality for cores loaded with Mo target plates is -2.92% for OSCAR-3 and -1.765 for MCNP.

For the core loaded with target plates, criticality calculations have been performed for different bank withdrawal positions, in order to analyze the effect of introducing more or less of the Cd section and fuel follower parts.

Figure 2 shows the global core reactivity with a fine mesh bank withdrawal positions, where positions are taken at the tip of each axial nodes, and few points within each node. OSCAR-3 approximates the cross section presentation of the Cd section and fuel follower inside the node with volume averaged cross sections, resulting in the effect shown by the blue line (cusping effect), whereas the MCNP results show a typical S-curve behavior.

Referring to Figure 3 - the percentage difference between OSCAR-3 and MCNP reactivates - and starting from banks fully inserted, the OSCAR-3 MCNP difference is seen to be 0.392%, the closest representing model of MCNP to OSCAR-3. Withdrawing the banks up to 400 notches (first three points on the curve), the trend is typical. From 400 to the next point, the reactivity jumps down where 0.4 cm Cd is withdrawn, part of Al coupling was replaced by water, and a small amount of fuel is present at the bottom of the core; the global effect to decrease the reactivity by ~100 pcm. Withdrawing the Banks up to 1000 notches, MCNP is still lower and the difference goes from 0.392% (zero withdrawn) to 0.3% (1000 notches); with peaks at the node tips of 0.47% and 0.52%, means 0.1% occurred due to Cd not present above the core. The error increases as the MCNP modelling introduces the first source of deviation from OSCAR-3 model of having Cd section above the core. This decreases the Cd section participating in absorbing neutrons and increases the global core reactivity. This trend will affect the difference with nearly constant value of ~ 1.671% inside the nodes and 1.5564% at the node tips, where 1.671% and 1.5564% are errors ascribed to not modelling the Cd section above the core when the bank position is greater than zero.

Bank withdrawal positions greater than 5552 notches were excluded from the above analysis as it is the second reason of difference between OSCAR-3 and MCNP. The Al-coupling piece is represented in MCNP and approximated with a shift of Cd section and fuel follower to the middle of the coupling

in OSCAR-3; this gives the reason for a jump in core reactivity at the last three points on the MCNP S-curve. Here only fuel follower and coupling are being added and the Cd is no-existent after 5552 notches, as the coupling is 3.85 cm and the MCNP modeling takes the bank position provided as being at the tip of the Cd. Accordingly;

1. MCNP model (MCNP-Os3) representing OSCAR-3 will be modified to introduce Cd above the core when the withdrawal position is greater than fully inserted, and the coupling will be replaced with Cd and fuel follower as in OSCAR-3.
2. A formula will be derived to position the control element with the bank position provided as:
   a. The zero position (fully inserted) of Cd lower tip will be the active core height, subtracting the total Cd section height, and
   b. The top (fully withdrawn) will be the active core height plus the coupling height, to reflect OSCAR-4 and physical modeling.

Regarding the graph, vertical lines representing the axial nodes tip, and between the solid bold vertical lines, show that the MCNP S-curve follows a typical trend, while it deviates outside the bold lines according to bank withdrawal position handling (coupling) on the left side, and Cd section not yet modeled above the core on the right.

Concluding the above analysis, it is to be predicted that after the aforementioned OSMINT modifications, the global core reactivity difference, with all cases and all bank withdrawal positions would be ~400 pcm between the OSCAR-3 and MCNP models, with MCNP being lower.

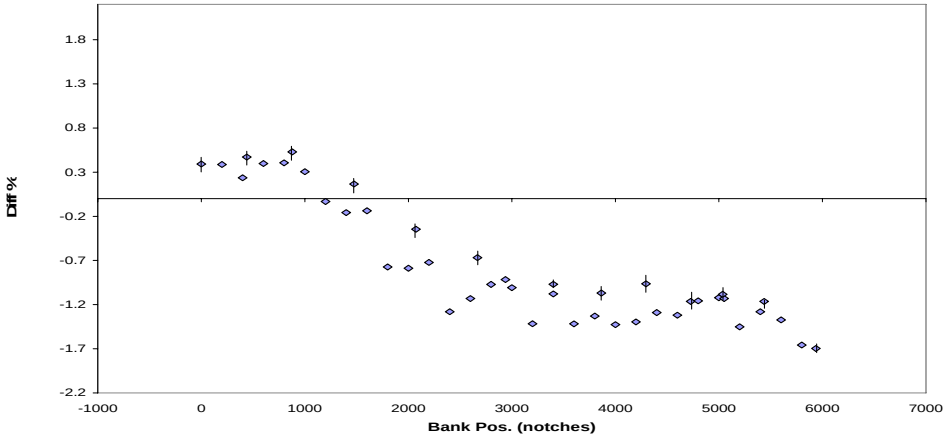

Fig 3. OSCAR-3 vs MCNP reactivity difference with bank withdrawal position
Slashed points are at the node tips, while without slashes are inside the node

4.3 Case I revised (MCNP-Os3r, MCNP-Os5)

Referring to section 3.IV and the analysis of Figure 2, it was clearly necessary to modify the OSMINT MCNP modeling (MCNP-Os3). After modifications to OSMINT following the aforementioned Case I, and referring to section 3.IV of additions to the OSMINT test version , Case I was revised to compare OSCAR-3 with OSMINT ver=3 (MCNP-Os3). The results and discussion are shown below, and figures 4-6 show OSCAR-3 and measurements comparisons with MCNP-Os3, MCNP-Os35 and MCNP-Os5 modeling (see additions to OSMINT, section 3.IV).

4.4 Results and Discussion Revised

Figure 5 shows a difference of 1.316% between OSCAR-3 MCNP-Os3 when the bank position is inside an axial node and 0.997% when the bank position at an axial node tips, on average.

While OSCAR-3, MCNP-Os3r and MCNP-Os5 were compared with measured critical settings, the vertical lines on the graph Figure 4 shows the magnitude of difference between each predicted critical setting and the measured setting as unknown: 5498, 5055 and 5050 for OSCAR-3, MCNP-Os3r and MCNP-Os5 and measurement, respectively.

The exact MCNP-Os5 model showed a good agreement with measured settings, namely 0.10813% average error in predicting the critical pattern (+0.05 cm control rod position).

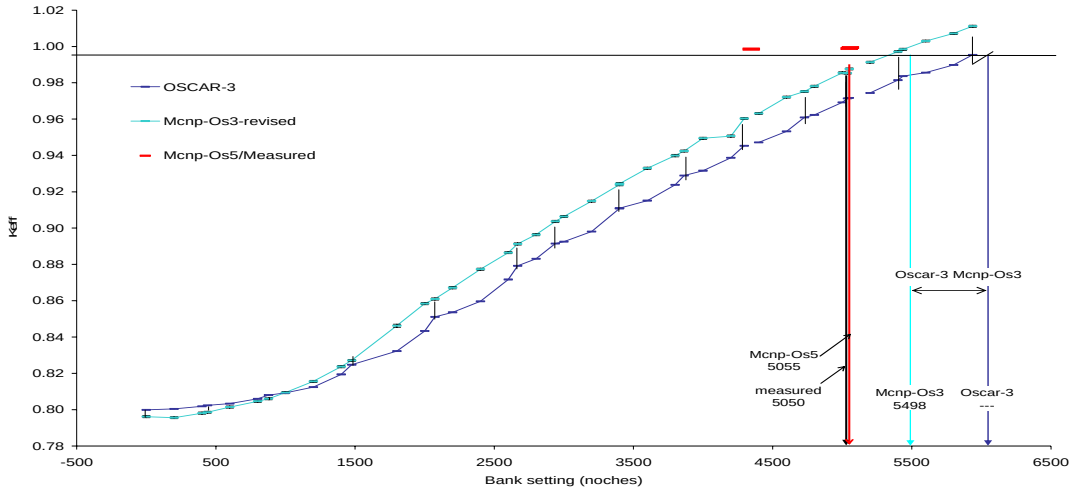

Fig 4. A comparison between OSCAR-3, MCNP-Os3r and MCNP-Os5

In Figure 5, the marked points (in circles) show the effect of coupling at the core bottom and top, and the graph shows a shift of the OSCAR-3 MCNP-Os3r results with some differences in magnitude due to the modifications made in the MCNP-Os3r model during the comparison process. The behavior is about constant after the bank position enters the fifth node from the bottom, the difference being 1.471% on average; the fluctuations of differences inside the nodes is according to the behavior of OSCAR-3 curve, while from first to the fourth node, the behavior is being investigated.

Bank Pos.(noche)	Mcnp-Os5	Std	Error%
4346	0.99854	0.00055	-0.14621
5050	0.99884	0.00056	-0.11613
5058	0.99938	0.00055	-0.06204

Table 1. MCNP-Os5 comparison with measured critical settings

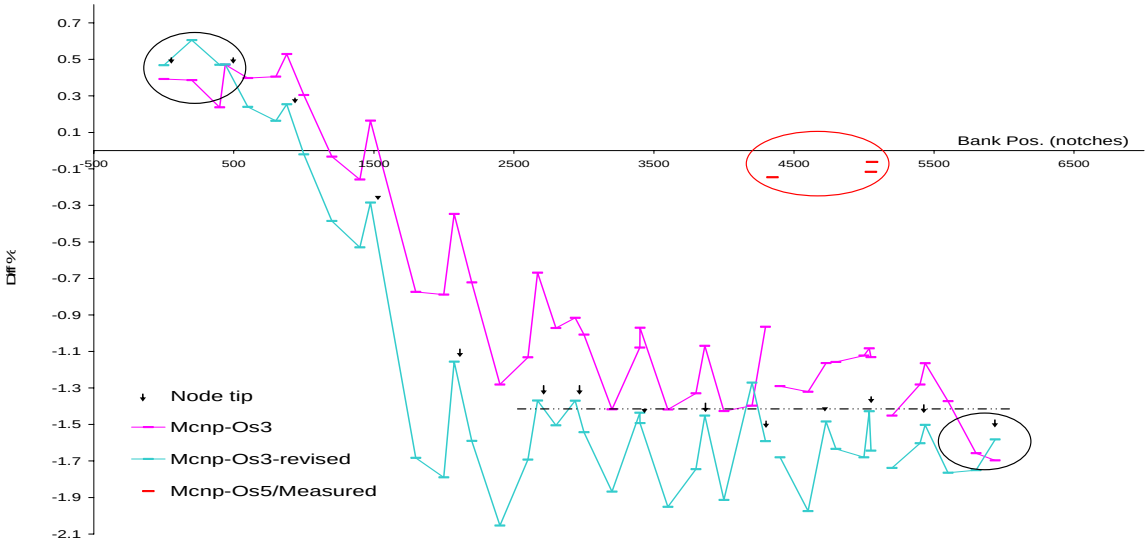

Fig 5. MCNP-Os3 and MCNP-Os3r revised difference relative to OSCAR-3

45. Case III (MCNP-Os5)

Validation against local neutronic parameters has been performed, via foils activation [7], showed a close agreement within the experimental error at the 1/3rd core top and fluctuated overestimations at the bottom 2/3rd, on average, which agree with the abovementioned coupling approximation analysis, and due to isotopic mass distributions prediction, measurements uncertainties, and lack of MCNP LFPs.

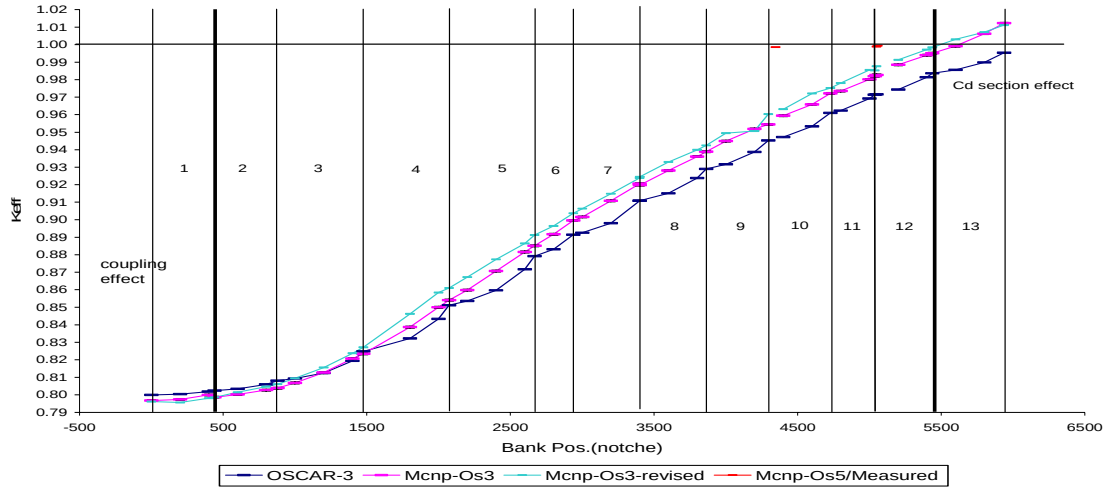

Fig 6. OSCAR-3 MCNP-Os3 and MCNP-Os3r revised comparison. The behavior of Os3 and Os3r are close but for near the bottom and top of the core, and significant differences are being investigated

5. Conclusions

The ability of OSMINT to set up a SAFARI-1 MCNP core model for any case, supplied from OSCAR-3, has been verified, the fuel/control/Mo rigs/peripherals core positions, the isotopic contents per node per plate per assembly and the overall core assembly dimensions. The generated MCNP inputs are ready to run without any modifications, provided the user follows the right process to build the model.

According to the modifications made, the global core reactivity difference between OSCAR-3 and MCNP has been changed, from a wide range of differences, with variation with the control rod withdrawal position and core state, to a very narrow range of max. -1.49% and min. -0.7% regardless of the control rod withdrawal position and/or core state, with no Mo target plates present. The difference for cores loaded with target plates was subjected to farther calculational analysis with fine mesh rod banks movements: the average difference at the node tips is ~-0.625%, and inside the node is -0.833%.

According to the above considerations and during the validation process, MCNP follows the same trend of uncertainty predicting measured values (Keff), where the uncertainty in criticality calculations with OSCAR-3 is ~ -8.2 % and MCNP-Os3 is ~ -6.99 % for cores without target plates, and -2.92% and -1.765% respectively for cores loaded with target plates. The sources of uncertainty are being studied and a decision will be made whether to accept the MCNP model with its underestimation of the global core reactivity.

The target plate modelling capability added to OSMINT, did not affect the OSCAR MCNP agreement trends; the target plate modelling, core position, isotopic contents, and the fuel/dummy-Al plate combinations have been verified.

6. References

[1] M. Belal, OSMINT OSCAR-3 MCNP INTerface, version 061t, June 1st 2006.
[2] SAFARI-1 Reactor Technical Data and Drawings.
[3] MCNP5-1.3 source files.
[4] Molly Irradiation Planning, November 2006.
[5] SAFARI-1 Safety Analysis Report SAR, Augest 2000.
[6] X-5 Monte Carlo team, *MCNP5 version 1.4*. LANL report LA-UR-03-1987, Los Alamos National Lab Los Alamos, New Mexico, April 2003.
[7] D de Villier, A. Graham, "Determination of Safari-1 Neutron Flux By MCNPX Modelling of Foil Experiments ", RRFM 2007.

RRFM200 CONFERENCE
LYON, FRANCE 11-15/3/2007

CONVERSION OF TAJOURA CRITICAL FACILITY FROM HEU TO LEU

A. KH. AJAJ
Reactor division Tajoura Research Center
Tajoura, Libya

O. A. ABULGASEM
Reactor division Tajoura Research Center
Tajoura, Libya
P. O.BOX 30878 Tajoura
E-mail omran_abuzid@yahoo.com

F. A. ABUTWEIRAT
Head of Reactor division Tajoura Research Center
Tajoura, Libya
P. O.BOX 30878 Tajoura
E-mail abutweirat@yahoo.com

ABSTRACT

The Tajoura Critical Facility has been converted from 80% enriched uranium IRT-2M (HEU) fuel to 19.7% enriched uranium IRT-4M (LEU) fuel. using the Russian manufactured IRT-4M fuel assemblies (FA), the compact core containing ten 3-tube and six 4-tube IRT-2M FA has been replaced by ten 6-tube and six 8-tube IRT-4M FA. The loading of the LEU to the critical facility was completed on January 2006. During the approach to criticality and after criticality was reached many measurements were performed. In this paper calculated parameters are presented. Two codes (WIMS and CITATION) are used for the calculations.

1. INTRODUCTION

The Tajoura Research Center operates both a 10 MW pool type research reactor and a Critical Facility. The fuel of the Critical Facility[1,2] has been converted from 80% enriched IRT-2M IRT-2M fuel to a less than 20% enriched uranium IRT-4M[3] fuel. The IRT-4M 8-tube and 6-tube fuel assemblies were loaded to the Critical Facility in January 2006. It is very important to determine all the neutronic parameters of the facility with the new LEU fuel. Most of these parameters such as the system excess reactivity, the shut down margin, and the reactivity worth of the control rods have been reported in anther paper[7]. Cross for core diagram for the critical facility is shown in Figure 1.
In this paper a detailed investigation and comparison of the flux distribution for both HEU and LEU cores are presented. Experimental measurements are underway and they will be compared to these calculated in the near future.

2. DATA AND RESULTS

The results presented in this paper are obtained using the diffusion theory (CITATION[4, 5] code). For the CITATION model the fuel assemblies are homogenized and the cross sections for the homogenized regions are generated using the WIMS[3] code. Two types of cells are used for the models in WIMS[5]; first the straight parts of the elements are taken as slabs while the central ring of the 8-tube and the curved corners of the fuel assembly are modeled using the annulus option. Results of the

comparisons between calculated LEU and HEU flux for a 4 watt critical state and for control rods worth are presented below.
The critical facility is modeled with sixteen fuel assemblies (ten 6-tubes and six 8-tubes IRT-4M FA or ten 3-tubes and six 4-tubes IRT-2M FA). The core has eight shim rods (KC rods in figure 1), two safety rods (AZ rods in figure 1), and one regulating rod (RR in figure 1). The core is surrounded by a Be reflector (20 moveable blocks, and a fixed Be reflector) where experiments can be loaded. If no experiments are present, Be plugs are inserted inside the Be blocks.

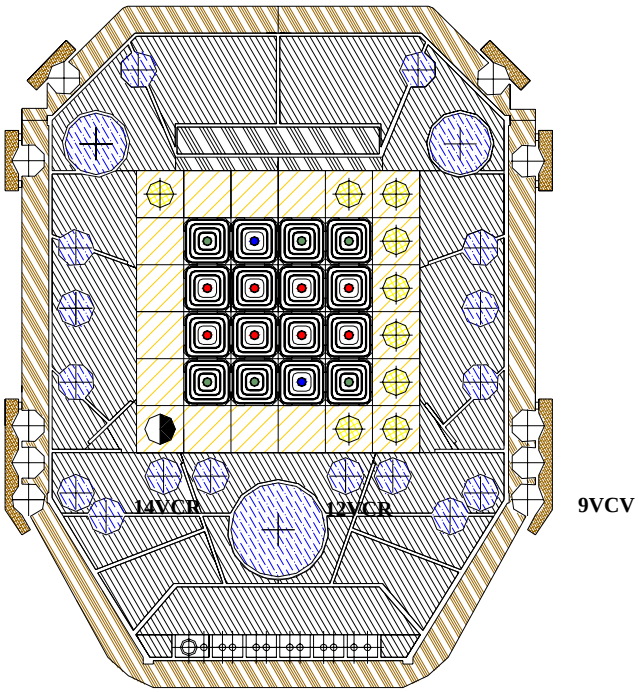

Figure 1 Cross Section of the Critical Facility Core Diagram

The results presented in this paper are obtained using the diffusion theory (CITATION[4, 5] code). For the CITATION model the fuel assemblies are homogenized and the cross sections for the homogenized regions are generated using the WIMS[3] code. Two types of cells are used for the models in WIMS[5]; first the straight parts of the elements are taken as slabs while the central ring of the 8-tube and the curved corners of the fuel assembly are modeled using the annulus option. Results of the comparisons between calculated LEU and HEU flux for a 4 watt critical state and for control rods worth are presented below.
The critical facility is modeled with sixteen fuel assemblies (ten 6-tubes and six 8-tubes IRT-4M FA or ten 3-tubes and six 4-tubes IRT-2M FA). The core has eight shim rods (KC rods in figure 1), two safety rods (AZ rods in figure 1), and one regulating rod (RR in figure 1). The core is surrounded by a Be reflector (20 moveable blocks, and a fixed Be reflector) where experiments can be loaded. If no experiments are present, Be plugs are inserted inside the Be blocks.

2.1 Integral Reactivity Worth of Control Rods

Comparisons between LEU and HEU for the 16 FA core with rods fully withdrawn, all shim rods and regulating rods fully inserted (shutdown state), and all rods (shim, regulating and safety fully inserted) are presented in Table 1. The results in this table show the differences between the two cores.
The reactivity worth of each of the control rods was measured with the 16 FA core configuration with all Be plugs in place. The Be plugs are positioned inside the halls of the Be blocks in the reflector when no experiments are installed. Comparison of the calculated and measured results using CITATION is provided in Table 2 below. The calculated results are essentially within about 10% of the measured results, which are considered to be in a good agreement given that there are some differences in way of calculating and measuring the reactivity worth of the control rods.

Case	Reactivity ($)	
	CITATION (LEU)	CITATION (HEU)
All Rods Out	21.08	17.73
All Shim and Regulating Rods Inserted	-5.05	-10.81
All Rods Inserted	-11.08	-16.797

Table 1 Reactivity for 16 FA Core with Different Sets of Rods Fully Inserted

Rod	*LEU Core* Results (β_{eff})		*HEU Core* Results (β_{eff})	
	Calculated	Experimental Results	Calculated	Experimental Results
Safety Rod AZ1	3.31	3.0	3.16	-
Safety Rod AZ2	2.87	2.5	2.79	-
Regulating R	0.58	0.62	0.446	0.41
Shim Rod KC-1	3.12	3.25	3.02	2.94
Shim Rod KC-2	2.96	3.1	2.87	3.23
Shim Rod KC-3	3.55	3.8	3.78	3.02
Shim Rod KC-4	3.36	3.7	3.61	4.50
Shim Rod KC-5	3.48	3.8	3.73	4.39
Shim Rod KC-6	3.31	3.65	3.57	4.11
Shim Rod KC-7	3.0	3.25	2.94	3.26
Shim Rod KC-8	2.77	2.98	2.74	3.22

Table 2 Control Rods Total Worth for 16 Fuel Assemblies Compact LEU and HEU Cores (With all Be plugs in place**)**

Finally, calculations were carried out to determine the fast and thermal fluxes in different positions in the core and reflector regions. Six locations are chosen for the comparison of fast and thermal flux distributions of the LEU and HEU cores. One locations is inside the core namely in the fuel cells (2-2), two locations are in the removable beryllium reflector namely cells (4-1) and (1-2), two locations are in the stationary beryllium reflector namely cells (12VCR) and (14VCR), and one location is in the aluminium vessel in cell 9VCV. Figures 2 to 7 show the axial flux distributions in these chosen locations. Figure 8 shows the thermal flux across cell (2-2) and figure 9 shows the radial flux distributions in the x-direction of the core passing through the center of cell (2-2). The comparison between HEU core and LEU core results is clear.

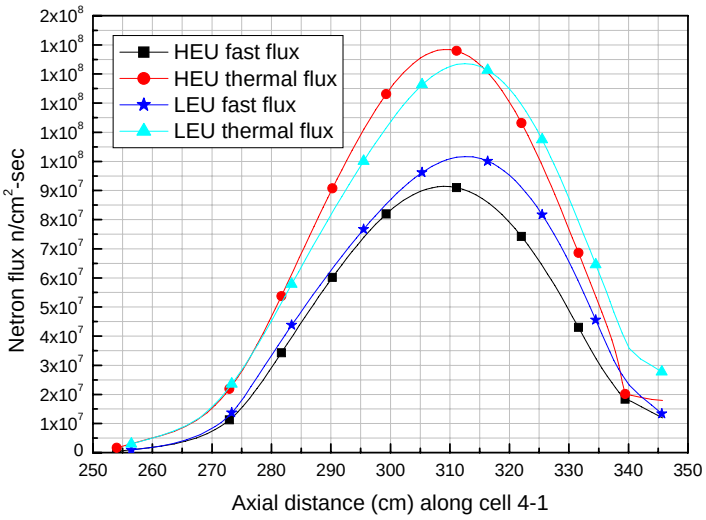

Figure 2 Calculated LEU and HEU fast and thermal flux distributions along cell 4-1

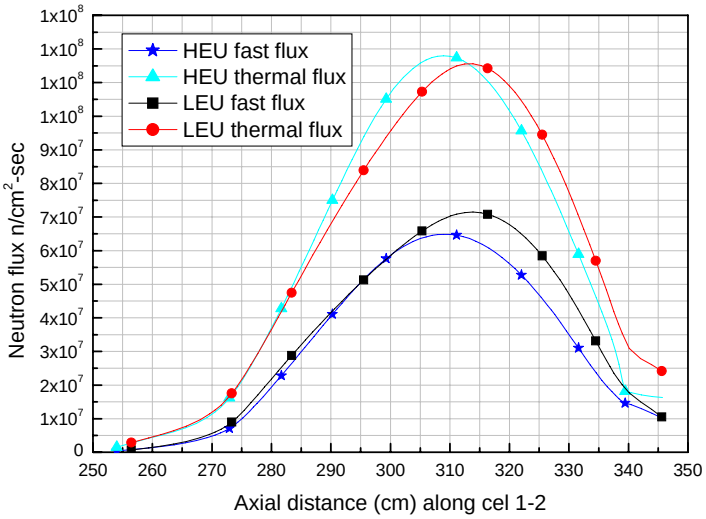

Figure 3 Calculated LEU and HEU fast and thermal flux distributions along cell 1-2

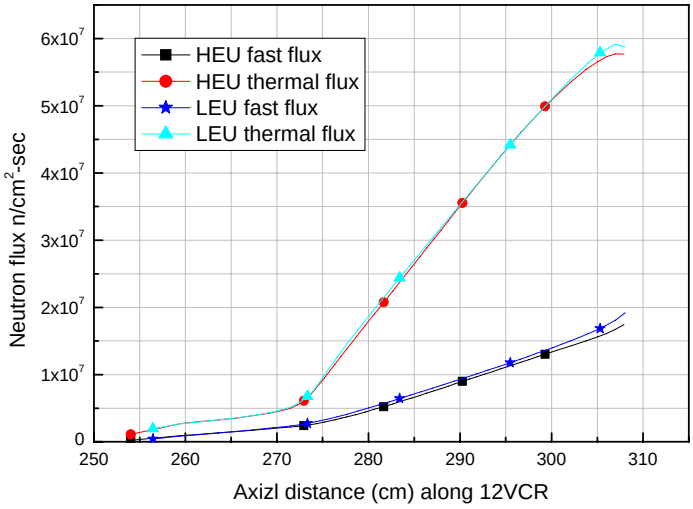

Figure 4 Calculated LEU and HEU fast and thermal flux distributions along 12VCR

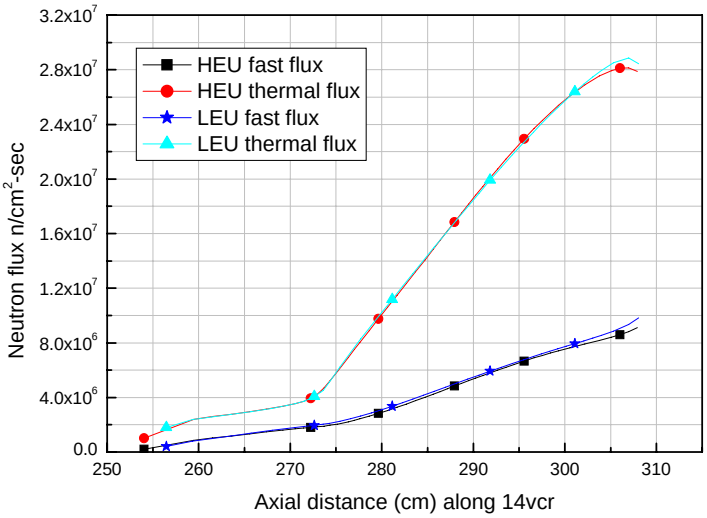

Figure 5 Calculated LEU and HEU fast and thermal flux distributions along 14VCR

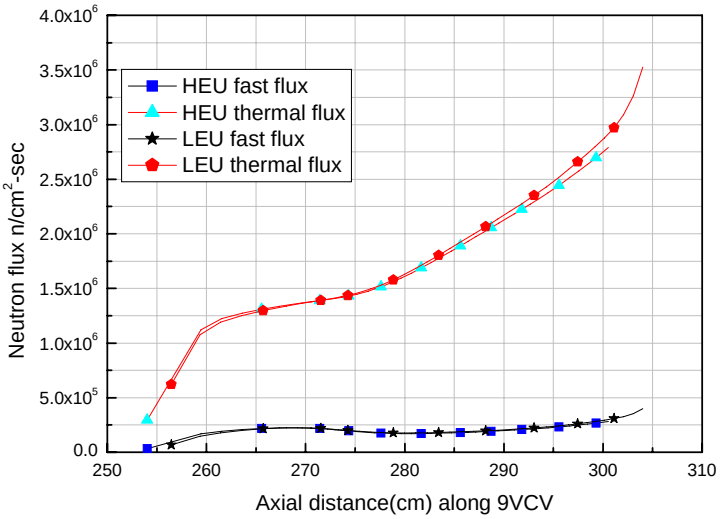

Figure 6 Calculated LEU and HEU fast and thermal flux distributions along 9VCV

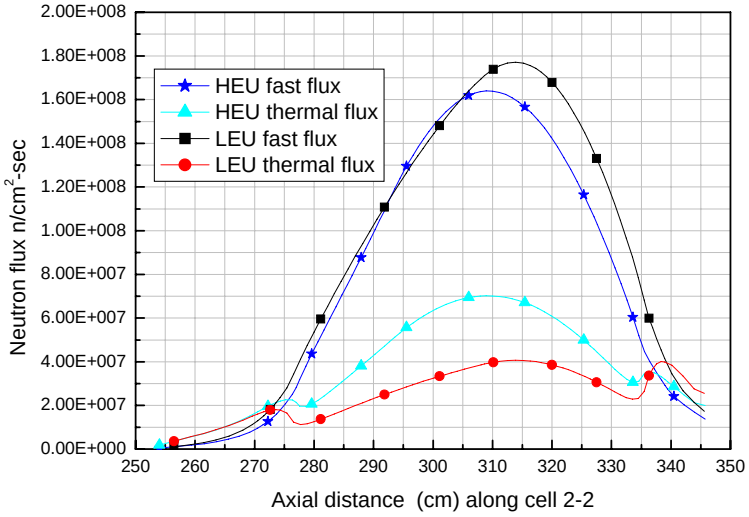

Figure 7 Calculated LEU and HEU fast and thermal flux distributions along cell 2-2

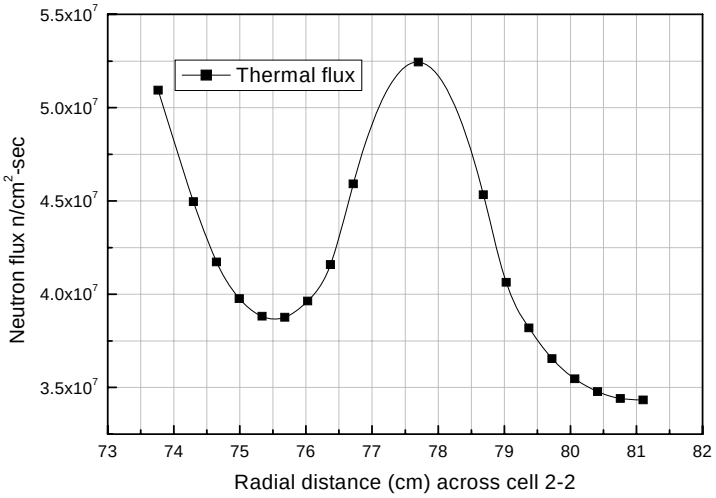

Figure 8 Calculated LEU thermal flux distribution in the x-direction across cell 2-2

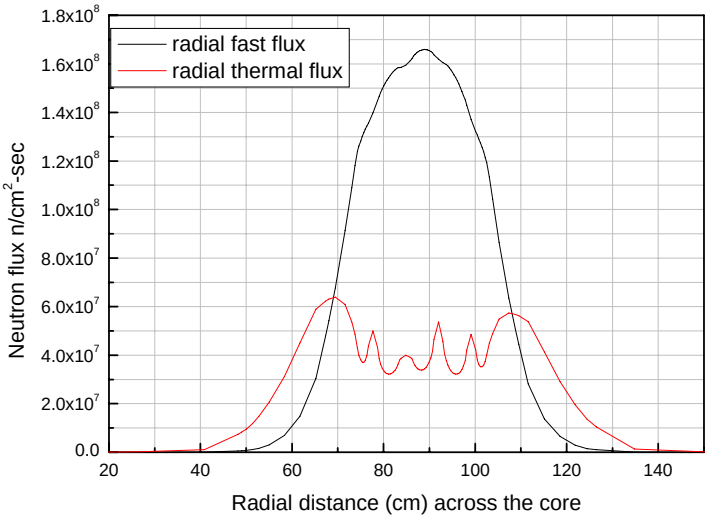

Figure 9 Calculated LEU fast and thermal flux distributions across the core through cell 2-2

3. SUMMARY

The Tajoura critical facility was recently converted from HEU to LEU (Jan/2006) using the Russian-made IRT-4M instead of IRT-2M FA. During the conversion process many calculations and measurements were carried out, and comparisons between measurements and calculated results using diffusion theory (CITATION code) methods were presented. As shown in the figures the fast flux increases and the thermal flux decreases for the LEU core in the fuel cells and in the reflector near to the fuel region. In the reflector away from the fuel and in the vessel both thermal and fast fluxes remain almost the same for both LEU and HEU cores.

4. REFERENCES

1- Tajoura Critical Facility Reactor Documentation.
2- Omran Abuzid Abulgasem, F. Abutweirat, and Abdo_Alhamed k. Ajaj, "Neutronics Parameters of Tajoura Research Reactor Fueled With HEU and LEU," Proceedings of the 2005 International Meeting on Reduced Enrichment for Research and Test Reactors, Boston, MA, USA, November 6-11, 2005.
3- Chernyshov V. M., Ryazantsev E. P., Egorenkov P. M.,Nassonov V. A., Yuldashav B. S., Karabeav Kh, Dosimbeav A. A., Aden V. G., Kartashev E. F, Lukichev V. A., "Results of IRT-4M Type FA's in WWR-CM Reactor (Tashkent)," RERTR San Carlos de Bariloche (Argentina) 3-8 Nov 2002 .
4- CCC-643, "CITATION-II Users Manual," ORNL.
5- MTR-PC V3.0 User's Manual, INVAP S.E., July 1995.
6- G. J. Taubman and J. H. Lawrence, "WIMSD4 User Manual," AEE Winfrith, Dorchester**,** Feb. 1981.
7- Omran Abuzid Abulgasem, H. Nilson, and Abdo_Alhamed k. Ajaj, "CALCULATED AND MEASURED PARAMETRS OF THE TAJOURA CRITICAL FACILITY FUELED WITH LEU" Proceedings of the 2006 International Meeting on Reduced Enrichment for Research and Test Reactors, Cape Town, South Africa, 29 October, 2006.

EFFECTS OF Ti IN THE UMo/Al SYSTEM : PRELIMINARY RESULTS

M. RODIER, X. ILTIS, F. MAZAUDIER, M. CORNEN, S. DUBOIS
CEA-Cadarache, DEN/DEC, F-13108 St Paul Lez Durance Cedex, France

P. LEMOINE
CEA-Saclay, DEN/DSOE, F-91191 Gif sur Yvette Cedex, France

ABSTRACT

Among the elements which could be added to the UMo fissile compound or to the aluminium alloy in order to prevent or reduce the UMo/Al interaction, Ti is a promising one since its affinity for Al is very important. The first results dealing with the effect of Ti on the UMo/Al reactivity are exposed in this poster. The metallurgical aspects of manufacturing the ternary compounds U-Mo-Ti by arc melting are described. Annealing treatments performed at 450°C on diffusion couple are presented and discussed.

1. Introduction

The UMo dispersion fuel is developed to convert the MTR cores currently working with UAl_x and U_3Si_2, with a more dense fuel able to reach the exigencies of the non-proliferation nuclear treaty with no or low modification of initial design. This treaty promotes pacific nuclear issues and gives a value of 20% as the upper allowed value for U^{235} enrichment (Low Enriched Uranium) [1]. In operating conditions, the interaction between UMo and its matrix Al results in a degradation of its performances leading sometimes to the failure of the fuel element. The understanding of the UMo/Al interactions is then a key stage for the research and the development of a UMo-based Low Enriched Uranium (LEU) fuel, behaving in a satisfactory way under irradiation [2-3-4-5].

According to the work performed by Park et al. [6], a promising way to reduce the reactivity of the UMo/Al alloys consists in adding element having both strong interactions (e.g. formation of intermetallics) with the matrix and weak ones with the UMo alloys. This assumption indicates that, as calculated by Y.S. Kim et al [7], among the different elements, tetravalent ones like Ti, Si or even Zr could be interesting candidates. However, zirconium reduces the γ phase stability by forming Mo_2Zr. This is the reason why we decided to choose Ti as a stabilizing element.

The binary U-Ti diagram (figure 1) shows the existence of a high temperature extended cubic solid solution between these two elements.

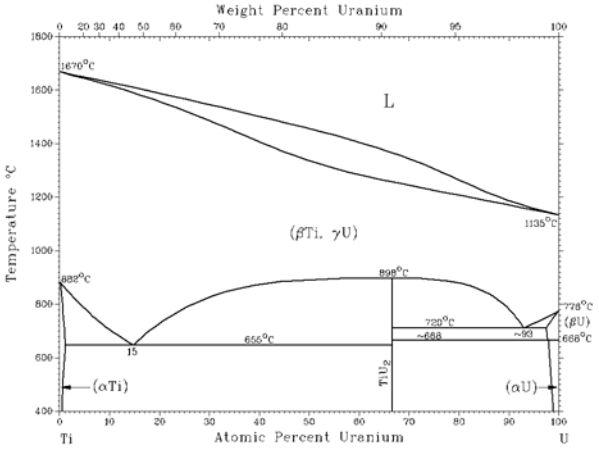

Fig. 1: U-Ti Phase diagram [8]

Compared with the TTT (Time, Temperature, Transformation) curve of the binary UMo8 (wt%) alloy, adding up to 1 %wt of titanium to the alloy does not change the ability of the cubic phase to be retained at room temperature by quenching (figure 2).

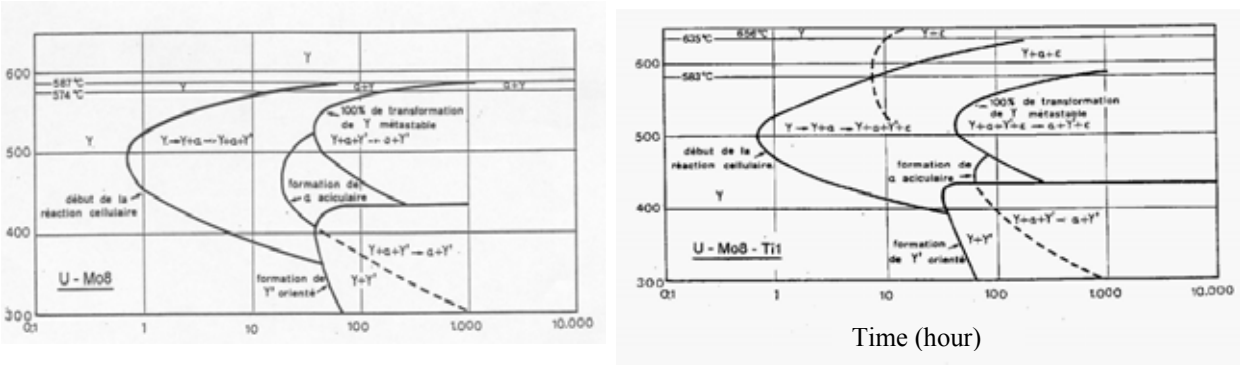

Fig. 2: U-Mo8 and U-Mo8-Ti1 TTT curves

The Ti-Al phase diagram (figure 3) illustrates the great chemical affinity between these two elements. Indeed, several intermetallic compounds can be formed, depending on the Ti/Al ratio. As previously discussed, this affinity could reduce the fuel-matrix interaction process.

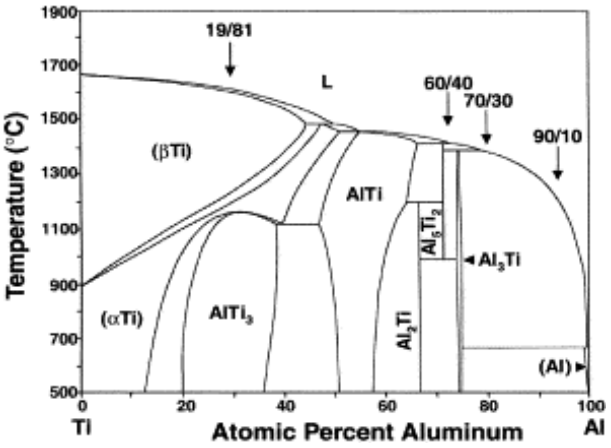

Fig. 3: Al-Ti phase diagram [9]

2. Experimental

2.1. UMoTi alloys

Small arc melted ingots (about 5 mm diameter) of UMo6Ti1 (wt%) were prepared sampling raw UMo5 alloy (11.6 at %) supplied by AREVA-CERCA and wires of pure Ti and Mo.
The metals, weighed in the proportions required for preparing a sample of approximately 1 gram, were molten by arc melting (Mini Arc Melter MAM-1, Bühler Company). To prevent the oxidation during the elaboration, high purity argon is used and Ti oxygen getter is melted before UMoTi alloys. A good homogenisation is expected to be reached carrying out several melting on each ingot, while turning over them each time. No mass loss has been detected during the elaboration process.
Aluminium grade 1050A was used in diffusion experiments : diffusion couples were prepared with samples of approximately 2 x 5 x 5 mm^3, cut out from Al foil and a half of a U-Mo-Ti ingot. These two parts were preliminary polished and etched in nitric acid in order to eliminate any trace of oxide.
Couples were maintained in a specific device loading samples up to 50 MPa approximately.

2.2. Thermal ageing

Following kinetic considerations given by the TTT curve of the alloys (cf. figure 2, despite a slight different composition of the alloy), thermal annealings were performed on UMo6Ti1/Al diffusion couples under a reducing atmosphere (Ar + 5% H_2), at 450°C for 2 hours in order to suppress/limit the influence of an eventual eutectoid transformation.

2.3. Characterization

The raw materials, as well as the aged samples were characterized with a classical XRD device (D8 Advanced Brüker) and by optical and electronic microscopies (FEG-SEM-Philips XL30 / EDAX EDS detector).

3. Results and discussion

3.1. Raw U-Mo-Ti alloys characterization

The XRD pattern (fig. 4) of an UMo6Ti1 ingot after its elaboration (without annealing) shows that the γ-phase of uranium is retained at room temperature and that the sample seems to be homogeneous (no secondary phase detected).

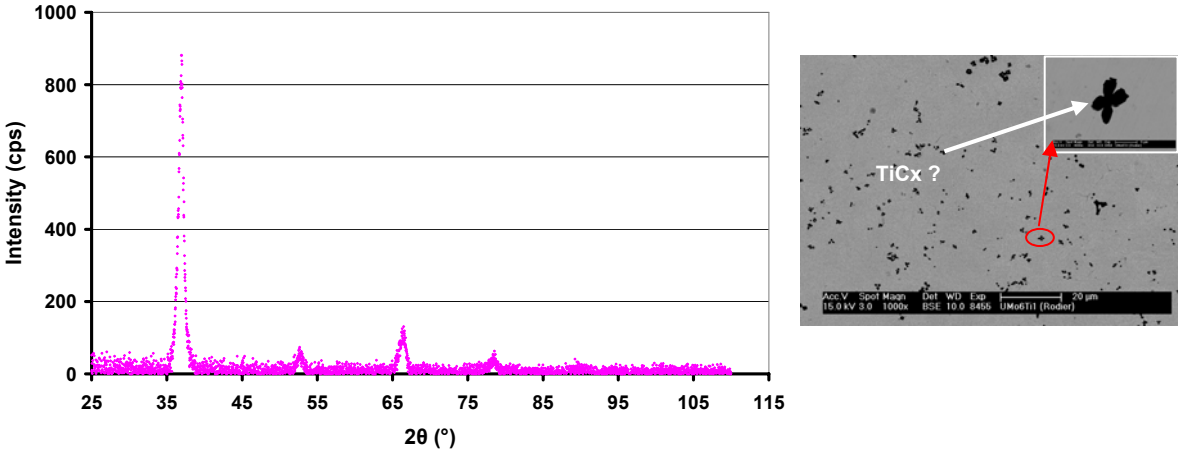

Fig. 4: X-ray diffraction pattern and SEM picture of a raw arc melted UMo6Ti1 ingot

Optical microscopy and SEM examinations showed however that at least a part of the titanium seems to be precipitated, probably as a carbide phase (as starlike carbide in fig. 4). In fact, some UC carbides were initially present in the UMo5 alloy ([C] content ≈ 1000 ppm). One can assume that this carbon should precipitate with Ti, as titanium carbides are at least as stable as uranium ones.

This partial precipitation of titanium leads probably to a smaller available concentration of this element in solid solution in the UMo alloy. We plan to check if an homogenization annealing will permit a resolution of the titanium containing precipitates. If not, a more pure UMo alloy should be used for the arc melting elaborations.

3.2. UMoTi/Al interaction (annealing treatment at 450°C, 2 hours)

Microstructures of an UMo6Ti/Al couple after a diffusion test at 450°C were examined by SEM. The interaction layer (which is not present along the whole interface of the couple) grows inhomogeneously at this temperature. Some UMo6Ti residual islets are also present in the interaction layer (IL). This tends to indicate that a prefered propagation is involved in the interaction process.

The IL's thickness varies from a few micrometers to 150 µm, in the same specimen (see figure 5a). This thickness variation could be due either to a residual oxide thin layer at the fuel-Al interface (especially for some parts where no IL is observed) and/or a poor contact between the samples.

Compositional analyses were performed by energy dispersive X-Ray spectroscopy (EDS). Figure5b shows different zones in the IL with variable compositions of U, Mo and Al, e.g. quoted 1 and 2 on the micrography. The analyses gave the following results (wt% element):

Wt%	U	Mo	Al
Zone1	68	2	30
Zone2	60	4	36

Table 1

In these two areas, titanium was not detected (its concentration is probably below the detection threshold).

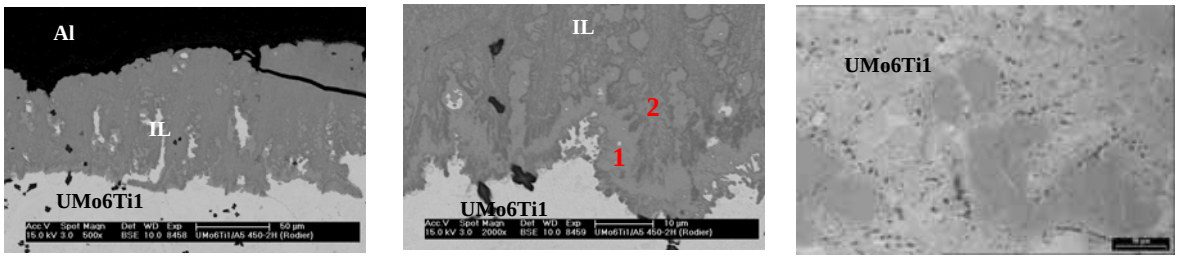

(a) (b) (c)

Fig. 5 : scanning electron micrographs of (a) interaction layer, (b) Al side of the IL and (c) two different compositions in IL

It is interesting to note that, in some areas of the UMo6Ti1 alloy (see figure 5c), a lamellar structure, which is typical of an eutectoide structure, is observed. Further XRD characterizations will be useful.

A compositional profile of U, Mo, Al and Ti concentrations was performed on the interaction layer (fig. 6). We are not able to distinguish different zones in the IL by this measurement method but the variations of concentrations in the first half of the IL are more important than in the part near the aluminium matrix. This phenomenon is explained by the residual islets of UMo6Ti which are present in the IL. A light depletion of Mo in the first part of the IL is also slightly visible on this profile. Next to the aluminium matrix, concentrations seems to stabilize around approximatey 60%U, 35%Al, 5% of Mo in weight. The titanium concentration seems to stay around 0.5% all along the profile, no variation of its concentration can be detected. It should be due, as previously explained, to its low concentration level in the UMo (1 wt%) in comparison with the detection threshold.

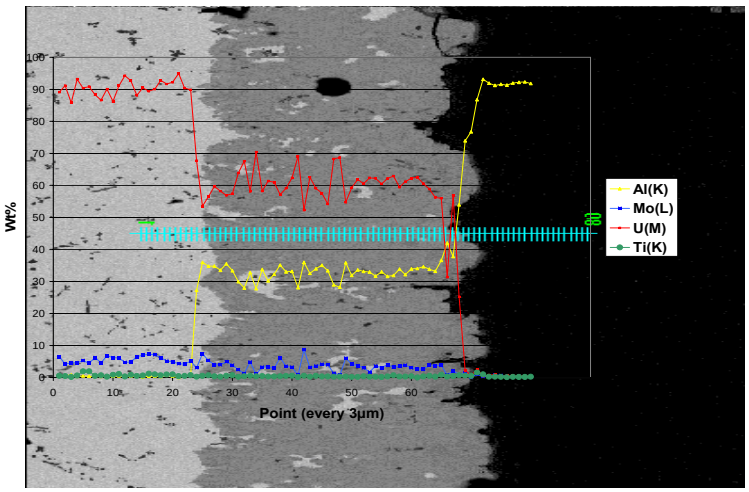

Fig. 6: Compositional profile through the IL in an UMo6Ti/Al diffusion couple annealed at 450°C for 2hours

All along the interface between the IL and Al, there is an accumulation of porosities which could be the result of the Kirkendall effects : to minimize the gradient of concentration between the IL and the Al phase, the aluminium flow generates, in the opposite direction, a flow of vacancies which will agglomerate close to the interface. This accumulation of vacancies forms porosities and then can induce a decohesion between the IL and Al.

4. Conclusions

The addition of Ti in the UMo/Al system is currently studied. We expose the first results, dealing with some metallurgical features of the UMoTi alloys, secondly with the effects of some weight percent of this element in the UMo alloy on the reactivity with aluminium.

Thermodynamic calculations and equilibrium data (i.e. available phase diagrams) show that Ti, acting like silicon, could reduce the interaction between UMo and Al. For this, one may consider its great binding affinity with Al leading to the possible formation of strong bonding intermetallic compounds acting like possible diffusion barriers.

Summarizing, let's point out the first and main results :

- UMo6Ti1 ingots (a few mm diameter, 1 g approx.) have been arc melted elaborated . As cast, the XRD pattern shows only the γ–UMo phase on the ingots. This allows to conclude on the ability of this ternary alloy to be retained in the γ form at room temperature. Nevertheless, Small precipitates of titanium compounds are present in the alloy bulk. Annealing homogenization treatments are planned in our future work.
- The first characterizations of a diffusion couple performed 2 hours at 450°C between 1050A Al alloy and UMo6Ti show:
    - The existence of a cellular decomposition within the U-Mo-Ti alloy, leading to the formation of a classical eutectoid microstructure.
    - The existence of a 150 µm max. thick interaction layer, which is neither regular nor homogenous. BSE imaging and EDS measurement shows the existence of a chemical heterogeneities, with a local Mo depletion near the UMoTi alloy, compared to the Mo content in the center of the IL.
    - The existence of porosities between the Al and the IL, which could be an evidence of the Kirkendall effects, i.e. the consequence of the coalescence of vacancies flowing in the opposite direction to the transport of Al. Due to its mobility and the existence of a chemical potential gradient within the layer, the Al diffusion, possibly more important than that of U or Mo, seems to drive the growth process. Maybe, the diffusion short-circuit of the freshly formed eutectoid microstructure are involved.

This work is still in progress and will focus on :

- The elaboration and characterization of different composition of U-Mo-Ti alloys (with more than 1%wt of Ti), and homogenisation annealing will be performed on every sample to share out Ti.
- New diffusion couples will be tested at an higher temperature and with other aluminium alloys,

Further characterization will be performed.

5. References

[1] J.L. Snelgrove et al., J. Nucl. Eng. and Des., 178 (1997) 119-126.

[2] G. L. Hofman, M. R. Finlay, Y.S. Kim, Trans. Intl. Meeting on Reduced Enrichment for Research and Test Reactors (RERTR), Vienna, Austria, 7-12 November 2004.

[3] A. Leenaers, S. Van den Berghe, E. Koonen, C. Jarousse, F. Huet, M. Trotabas, M. Boyard, S. Guillot, L. Sannen, M. Verwerft, J. Nucl. Mater. 335 (2004) 39-47.

[4] P. Lemoine, J.L. Snelgrove, N. Arkhangelsky, L. Alvarez, 8th Intl. Conf. Research Reactor Fuel Management (RRFM'04), München, Germany, March 21-24, 2004.

[5] S. Dubois, F. Mazaudier, J.P. Piron, P. Martin, J.C. Dumas, F. Huet, H. Noel, O. Tougait, C. Jarousse, P. Lemoine, 9th Intl. Conf. Research Reactor Fuel Management (RRFM'05), Budapest, Hungary, 10-13 April, 2005.

[6] J.M. Park, H.J. Ryu, G.G.Lee, H.S.Kim,Y.S.Lee, C.K.Kim, Y.S.Kim, G.L. Hofman Trans. Intl. Meeting on Reduced Enrichment for Research and Test Reactors (RERTR), Boston, USA, 6-10 November 2005.

[7] Y.S. Kim, G.L. Hofman, H.J. Ryu and J. Rest, Trans. Intl. Meeting on Reduced Enrichment for Research and Test Reactors (RERTR), Boston, USA, 6-10 November 2005.

[8] "Binary Alloy Phase Diagrams", 2nd edition, 1990, ASM International (USA)

[9] http://www.crct.polymtl.ca/FACT/documentation/BINARY/BINARY_Figs.htm

[10] H. Palancher et al., 10th Intl. Conf. Research Reactor Fuel Management (RRFM'06), Sofia, Bulgaria, April 30-May 3, 2006.

FULL CONVERSION OF MATERIALS AND NUCLEAR FUEL – RESEARCH&TEST – TRIGA SSR 14 MW

M. CIOCANESCU, M. PREDA, C. IORGULIS
TRIGA REACTOR, INSTITTUTE FOR NUCLEAR RESEARCH PITESTI
CAMPULUI STREET NO. 1, 115400 - ROMANIA

1. Introduction

The location of the Institute for Nuclear Research is Pitesti, 100 Km Northwest of Bucharest. Our TRIGA reactor was commissioned in 1980 (first criticality has reached on November 17th, 1979). In fact, as it could be seen in the Figure 1, the TRIGA reactor consists in two reactors:

- ✓ A Steady State Reactor, 14MW, initially loaded with HEU fuel (93% enrichment).
- ✓ An Annular Core Pulsing Reactor of 20.000MW.

Figure1 TRIGA reactor pool arrangement

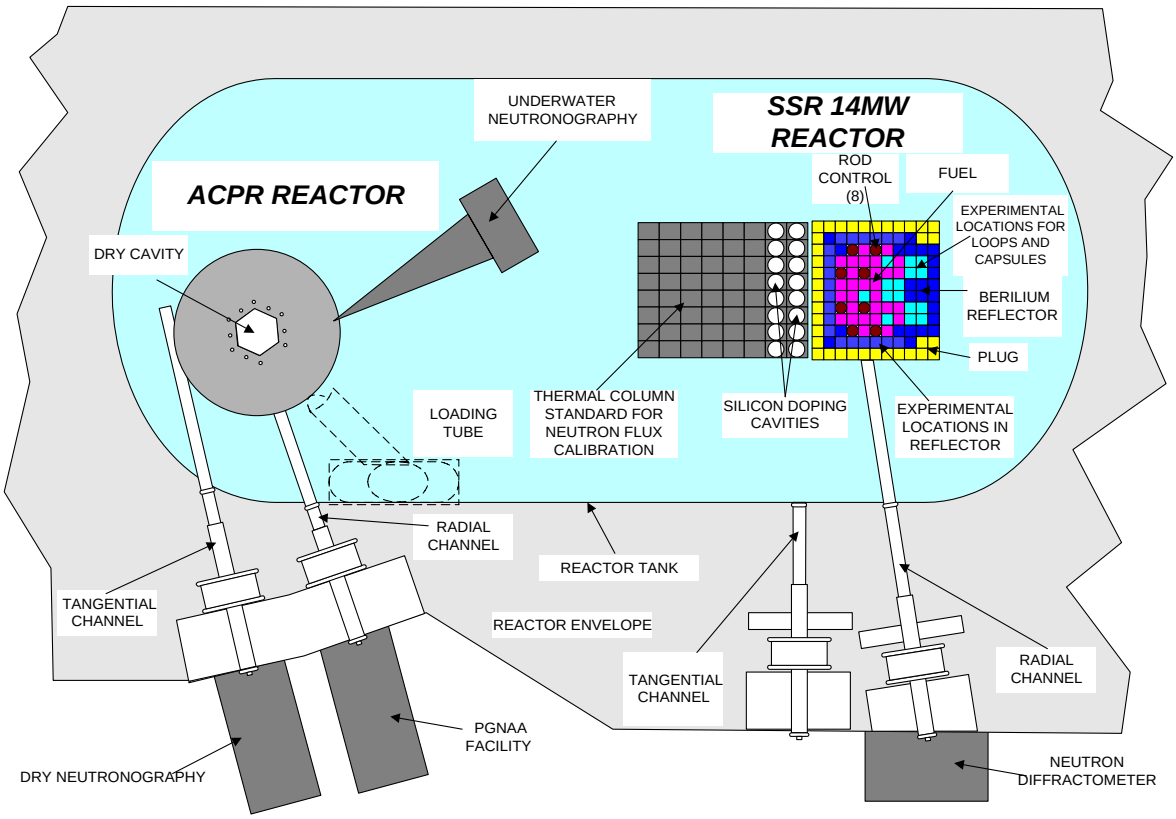

TRIGA SSR Main Characteristics

LEU fuel core	
Low Enriched Uranium (LEU)	10% weight U235, 23% U235 enrichment
Composition	Er-U-Zr1.6 eutectic alloy fuel moderator, Er 2.8% weight
Clad Material	Incoloy 800
Pellet Diameter	1.27 cm
Clad Diameter	1.372 cm
Fuel Length	56 cm
Total Length	76 cm

Reflector	
Type	Beryllium with and without central hole
Number	20 with central hole & 20 without central hole
Dimension	Same cross section as the fuel bundle
Control Rods	
Number	8
Type	Sinterized Boron
Poison Type	B4C natural

Total Weight	0.438 kg of B_4C
Bundles Number	29
Fuel Elements Bundle	25

Actuation Mechanism	Rack and drive pinion
Operational Features	
Max. Power	14MW
Max. Thermal Flux	$2{,}9x10^{14}$ n/cm^2·s
Max. Central Fuel Temp.	To Be Determined

TRIGA ACPR Main Characteristics

Fuel	
Type and Enrichment	12 wt% U- ZrH fuel, 20 wt% ^{235}U
Cladding material	stainless steel with dimples
Diameter	3.56 cm
Cladding diameter	3.76 cm O.D.
Section length	38 cm
Rods number	146+6 fuel followers
Control rods	
Number	6
Type	fuel followered type
Poison material	natural B_4C
Rod drive	rack and pinion
Transient rods	
Number	2 fast transient rods and 1 adjustable transient rod
Poison material	92% enriched B_4C
Rod drive	fast: pneumatic, adjustable: rack and pinion drive
Reactor performances	
Steady state power	500 KW
Maximum peak power	20,000 MW
Maximum core energy release	106 MW s
Pulse width	4.6 ms 1/2 peak power
Prompt neutron Lifetime	32μs

Initially the standard core contained 29 HEU fuel bundles

- ✓ XC1, XC2, XC3 experimental locations with a similar geometry as one fuel bundle,
- ✓ XL1, XL2, XL3 experimental locations with a similar geometry as four fuel bundles.

That was the configuration used to determine the TRIGA SSR 14MW core performances (see Fig. 2).

Figure 2 TRIGA SSR Startup Core Configuration, November 17th, 1979

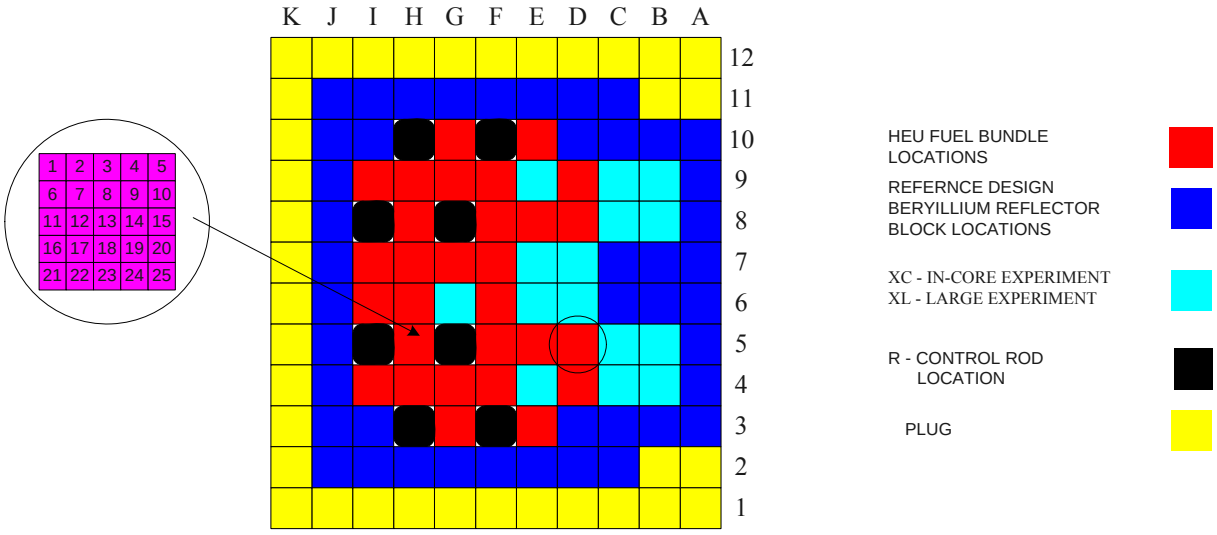

Over time the core configuration was modified due to acquisition/fabrication of the irradiation devices used for CANDU nuclear fuel and materials testing. In any configuration the location XC1 used in connection with Loop A was kept unmodified. The reason is that this irradiation device has a fixed position within reactor core. TRIGA SSR 14 MW use for research and testing program accomplishment imposed HEU refueling in order to maintain an excess of core reactivity.
An effective use of nuclear fuel, assessments and measurements and an adequate management allows us to attain an average burn up of 55%, and to reconfigure the core from 29 to 35 HEU fuel bundles. This core configuration was realized in 1991 and is presented in the following Figure 3:

Figure 3 TRIGA SSR core configuration in 1991

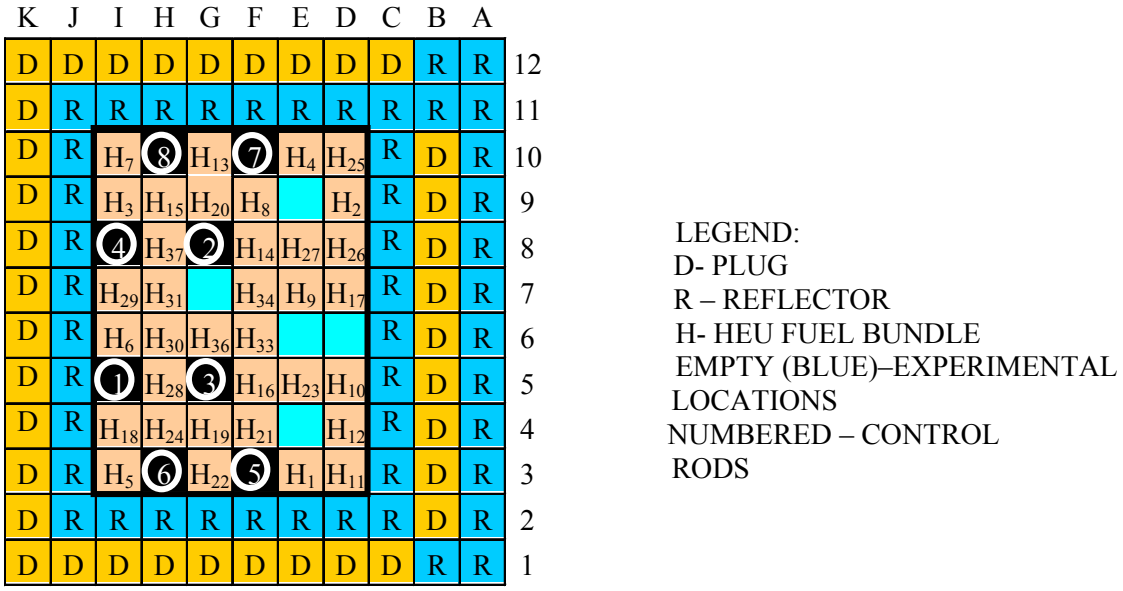

TRIGA reactor conversion has a technical, scientifically, politically and economically significance. The process began in 1992 by core loading with LEU fuel provided by General Atomics, and is related to RERTR program that aims to reduce enrichment in order to decrease the risk of nuclear weapons proliferation. In 1990 it was established an agreement with ANL related to TRIGA SSR core conversion. The main objectives of that agreement were related to neutron and thermal analysis accomplishment in order to determine the feasibility of the conversion project. Once the project was completed at the end of the 2005, in 2006 was performed the conversion from mixed HEU+LEU to full LEU core.

Figure 4 TRIGA SSR core configuration in 1992 after the first step of conversion

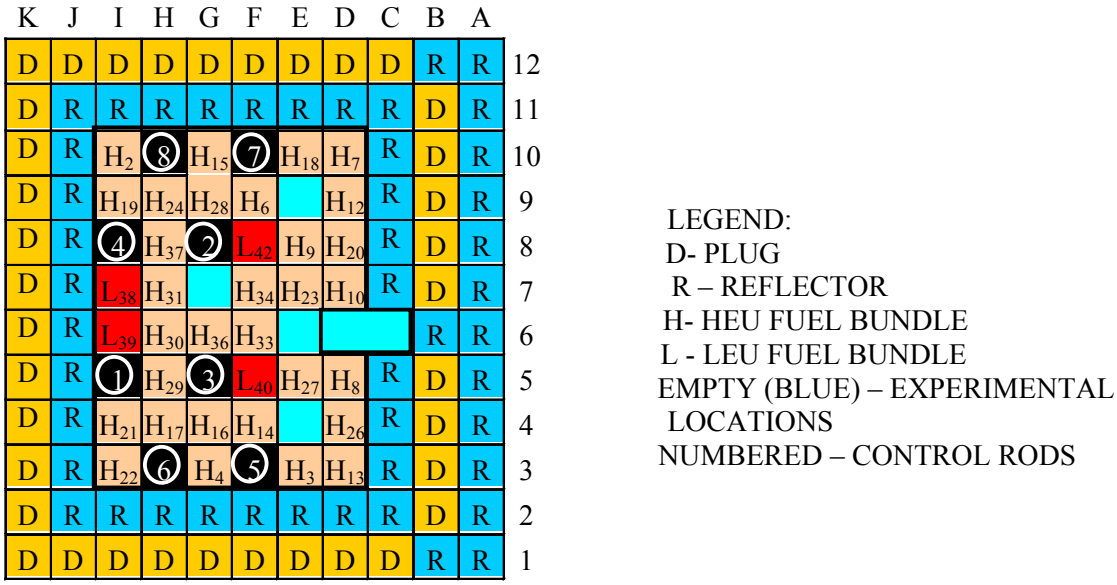

As the Figure 5 emphasize, in March 2004 the mixed reactor core has 18 LEU and 17 HEU fuel bundles by HEU-LEU replacement in successive steps of refueling.

Figure 5 TRIGA SSR core configuration in 2004 before the final step of conversion

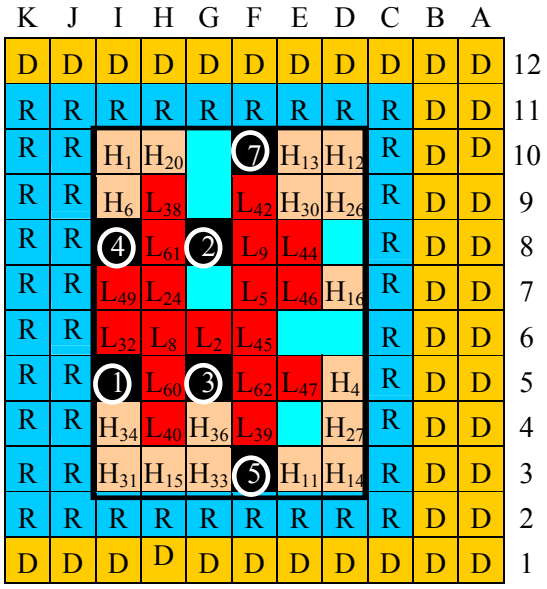

Starting from this configuration in 2006 was completed the final HEU-LEU fuel conversion by complete removal of HEU fuel bundles (Figure6) and refueling with fresh LEU fuel manufactured by CERCA, France. As result we have now a standard reactor core with 29 LEU fuel bundles (Figure7).

Figure6 TRIGA SSR core configuration without HEU

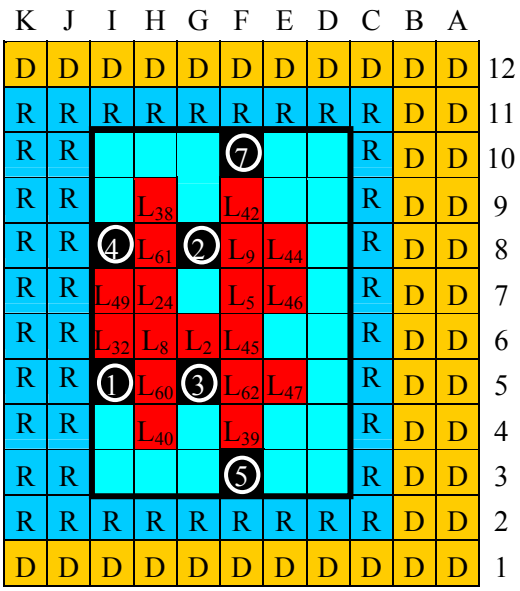

Figure7 TRIGA SSR final core configuration

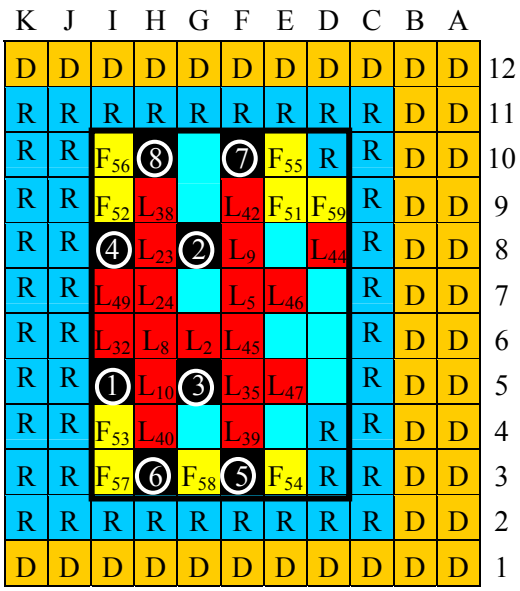

LEGEND:
D- PLUG
R – REFLECTOR
F- FRESH LEU FUEL BUNDLE (FRENCH FUEL)
L - LEU FUEL BUNDLE
EMPTY (BLUE) – EXPERIMENTAL LOCATIONS
NUMBERED – CONTROL RODS

From 1992 until 2005 the TRIGA-SSR 14MW reactor with mixed HEU-LEU core was in operation for 1409.93 days. During this time the released energy was 11504.94 MWd. The following graphic illustrates the reactor function history:

Figure7 TRIGA SSR-14MW REACTOR OPERATION IN 1992 - 2005

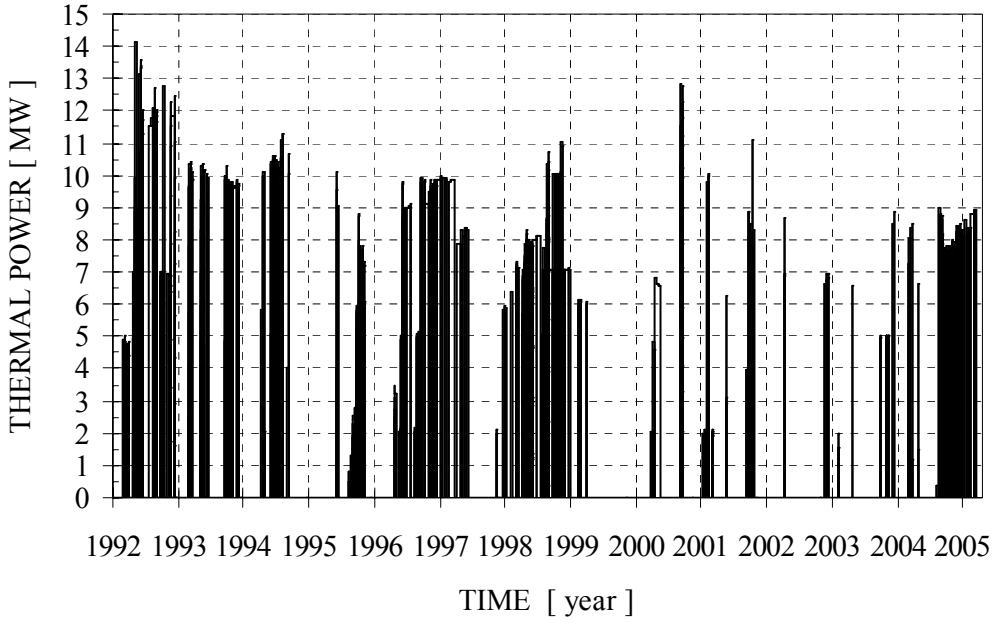

As a result of our assessments the following table emphasizes the differences between HEU and LEU core:

Table1 TRIGA SSR parameters comparison between 29 HEU and 29 LEU bundles core:

Parameter	**HEU**	**LEU**
Fuel bundles	29	29
Reactor Power	14 MW	14 MW
Inlet Temperature	37°C	37°C
Flow rate with one pump in primary cooling system	400 Kg/s	400 Kg/s
Flow rate with two pumps in primary cooling system	700 Kg/s	700 Kg/s
Safety limit for nuclear fuel	1150 °C	1150 °C
Φmax (XC1 location)	2.9×10^{14} $(cm^2 \cdot s)^{-1}$	2.82×10^{14} $(cm^2 \cdot s)^{-1}$
PPFmax	2.5	2.14
APFmax	1.30	1.313
CPFmax	3.25	3.01
a	6.0×10^{-5} $(°K)^{-1}$	5.5×10^{-5} $(°K)^{-1}$
Keff	0.00725	0.00730
Tcmax	705 °C	617 °C
Core life time	8000 MWD (29 fresh HEU fuel)	4500 MWD (11 fresh and 18 burned LEU fuel)
Shim bundle removal		
Pmax	550 MW	500 MW
$T_C$max	810 °C	773 °C *

The assessment of LEU nuclear fuel behavior shows differences between maximum temperature values and maximum flux values for LEU and HEU fuel. These differences appear due to loading diagram with fresh LEU fuel: because of the relative large amount of fuel bundles (11 out of 29) that have been introduced in a single step, these bundles were placed on reactor core edge.

RESULTS OF POST-IRRADIATION EXAMINATION OF THE (U-Mo)–ALUMINIUM MATRIX INTERACTION RATE

G.A. BIRZHEVOY, V.V. POPOV
FSUE "SSC RF – Institute for Physics and Power Engineering"
Bondarenko sq.,249033, Obninsk, Kaluga reg., Russia

O.A. GOLOSOV, V.V. SHUSHLEBIN, V.A. RYCHKOV, M.S. LYUTIKOVA
FSUE Institute of Reactor Materials
624250, г.Zarechniy, Sverdlovskaja reg., Russia

ABSTRACT

For improving the irradiation stability of the U-Mo/Al fuel composition it is necessary to reduce the rate of the interaction between the fuel particles and the Al matrix. Using the Al matrix alloyed by Si and creating the barrier coatings on the fuel particles have been considered as the possible ways.
The first results of post-irradiation examination of the fuel particles interaction with the matrix in U-Mo/Al and U-Mo/Al-12%Si compositions and in the same compositions with the Nb, Zr-1Nb and UO_2 barrier layers around the fuel particles are presented in this paper. In the course of irradiation 60% ^{235}U burn-up has been achieved at 19.7% fuel enrichment.

1 Introduction

It has been reported [1] that for reducing the interaction rate of U-Mo fuel particles with Al matrix the mini-elements, containing the different types of barrier coatings around the fuel particles and two types of matrix material, have been fabricated and exposed to irradiation in the IVV-2M reactor.
This paper presents the first results of post-irradiation examination of the fuel particles - matrix interaction in the U-9%Mo/Al and U-9%Mo/Al-12%Si compositions and in the same compositions with the Nb, Zr-1%Nb and UO_2 barrier layers around the fuel particles irradiated to 60% ^{235}U burn-up at 19.7% fuel enrichment.

2. Fuel composition

The next types of the fuel compositions have been chosen for irradiation:

- U-9%Mo/Al;
- U-9%Mo/**Nb**/Al;
- U-9%Mo/**Zr-1%Nb**/Al;
- U-9%Mo/**UO_2**/Al;
- U-9%Mo/Al-12%Si;
- U-9%Mo/ **UO_2**/Al-12%Si.

The basic matrix is the PA-4N (Al-0.3%Si) powder. The fuel particles have been coated by Nb and Zr-1%Nb alloy using the plasma method. The thickness of the barrier layer was equal to 1-2.5 and 1-2 μm, correspondingly. The UO_2 layer has been obtained on the fuel particles by oxidizing in air, the layer thickness is ~0.3 μm.

3. Mini-elements

Mini-elements have been fabricated by the following manner. The fuel composition was being put into the aluminium cylinder. Its diameter was equal to 10.9 mm, the bottom thickness is equal to 1.5 mm.

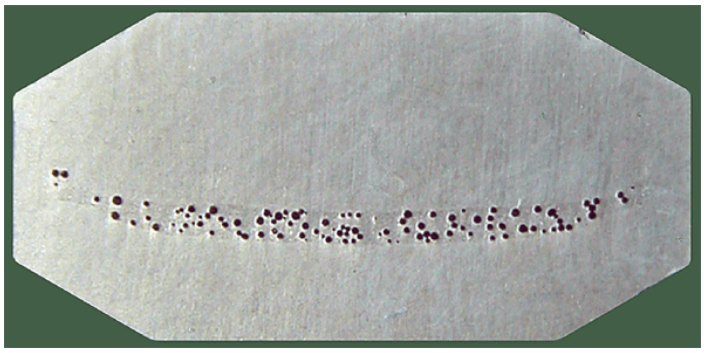

The cover with thickness of 3 mm was being inserted into the cylinder. Then the hot pressing have been carried out. The diameter of mini-elements is equal to 10.88-11.0 mm, the height is equal to 5.07-5.28 mm. The common shape of the mini-element cross-section is shown in Fig. 1.

Fig. 1. Typical mini-element cross-section

4. Irradiation conditions

The scheme of mini-element disposition in the plates of the irradiation assembly in the IVV-2M reactor with the indication of their number and of materials of the matrix and barrier layer is shown in Fig.2. The distance between mini-elements along the plate was equal 14 mm.
The plates were placed vertically in the special irradiation assembly (Fig. 3), and their both sides were being washed by water. The center of the active zone was placed at the level of the third floor mini-element middle.

№52 Al-Si -	№58 PA-4N Nb	№50 Al-Si -	№60 PA-4N Nb
№53 PA-4N -	№48 Al-Si UO_2	№65 PA-4N Zr-1Nb	№63 Al-Si UO_2
№40 PA-4N UO_2	№54 PA-4N -	№61 PA-4N Nb	№66 PA-4N Zr-1Nb
№67 PA-4N Zr-1Nb	№47 PA-4N UO_2	№57 PA-4N -	№43 PA-4N UO_2
№62 PA-4N Nb	№68 PA-4N Zr-1Nb	№45 PA-4N UO_2	№70 PA-4N -

Fig. 2. Mini-element disposition in the plates

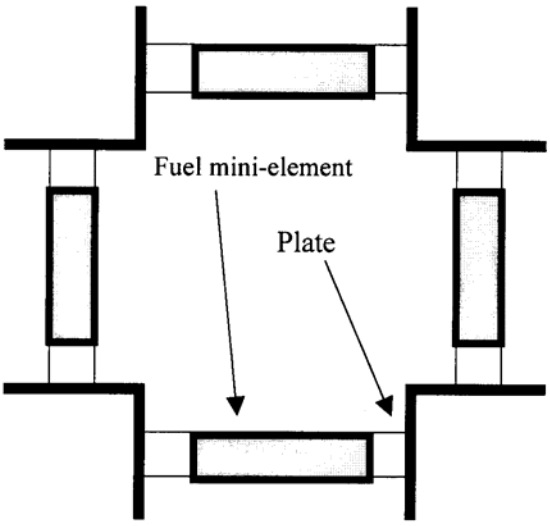

Fig. 3. Cross-section of the irradiation assembly

The irradiation was conducted in the interior of the fuel assembly placed in the 5-5 cell of the IVV-2M reactor active zone for 118 days at the nominal reactor power. The mean heat flux density was equal to 60 W/cm^2. The mean fission rate was equal to 4.0×10^{14} fis./(cm^{3}c). The mean fission density of 4.1×10^{21} fis./cm^3 and the equivalent ^{235}U burn up of 60% have been achieved to the irradiation end.
The thermocouples were placed in the claddings of two mini-elements. The cladding and water temperatures were controlled at the input and output and in the active zone center in the course of the reactor testing.
The calculation of the temperature distribution along the mini-element cross-section is shown in Fig.4.

5. Post-irradiation test results

The mini-element visible failures and the bulges on the claddings were not observed.

The results of the mini-element thickness measurements, attributed to the fuel layer, are shown in Fig.5. The basic U-Mo/Al composition exhibits the highest swelling (~17%). Coating of the U-Mo particles by Nb and Zr-1%Nb alloy reduces the swelling of the basic U-Mo/Al composition by 20-27%, and oxidizing – ~45%.

Using the Al-12%Si alloy as the matrix and the particles without the coating leads to the swelling reducing by comparison with the basic composition by 20%, and using the UO_2 coatings – more than two times.

The mini-element cross-section metallographic test results are shown in Fig. 6.

Cracking of the composition was not detected in all cases. As a rule, the barrier layer around the particles, the interaction zone «matrix-fuel particles» and the region of the fission fragments output to the matrix have been observed. Moreover, the formation of the interaction zone on the Al matrix side is typical for particles with the barrier coatings. This is indirect evidence of the preferential diffusion of U atoms to region of the reaction with the components of the Al matrix.

The results of measuring the barrier coatings thickness, the interaction zone width and the layer width of the matrix, damaged by the fission fragments for different types of the fuel composition are presented in Table.

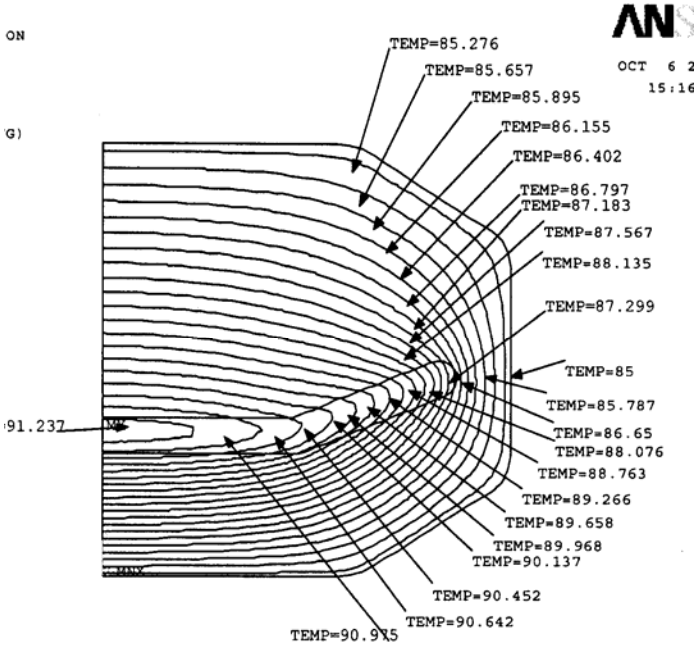

Fig. 4. Temperature distribution along mini-element cross-section

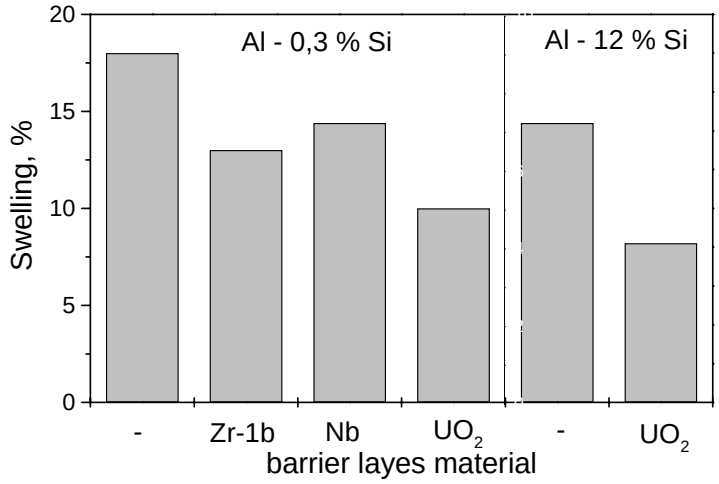

Fig. 5. Swelling of fuel compositions: U-Mo/Al; U-Mo/Nb/Al; U-Mo/Zr-1%Nb/Al; U-Mo/UO_2/Al; U-Mo/Al-12%Si; U-Mo/ UO_2/Al-12%Si.

The maximum interaction layer thickness was observed for the basic U-Mo/Al composition and was equal to ~5 μm. The oxidic coatings (thickness is ~0.3 μm) on the surface of the particles insignificantly reduce the (U,Mo)Al_x layer thickness. The (U,Mo)Al_x layer thickness for the UMo/Nb/Al composition is less by ~30% by comparison with the basic composition and is nearly 6 times less if the coatings from the Zr-1%Nb alloy are used.

The addition of 12% Si to the Al matrix leads to reducing the (U,Mo)Al_x layer thickness by ~15% for the particles without the coatings and - by ~30% for the oxidized fuel particles by comparison with the technically clean Al matrix.

The presence of the metal coatings on the particles surface leads both to reducing the (U,Mo)Al_x layer thickness and to reducing the width of the damaged by the fission fragments Al matrix layer around the particles by 15-20%. This may be an evidence of the less fission fragments (including gaseous fragments) content both in the matrix and in the layer around the fuel particles and, therefore, may positively influence on the behaviour of such compositions under irradiation including the case of the more high burn-up.

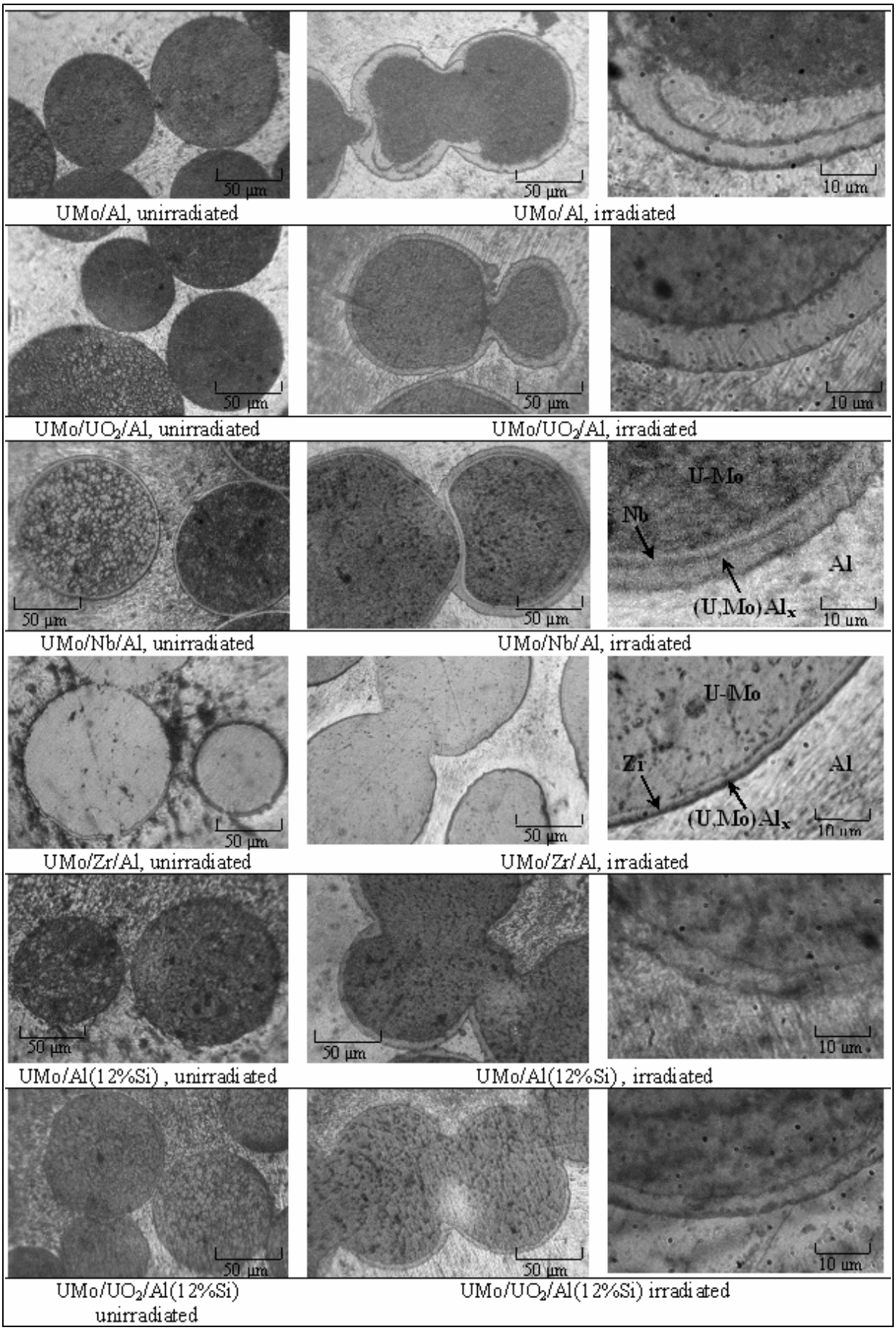

Fig. 6. Structure of the fuel compositions before and after irradiation

Table – Thickness of coatings, $(U,Mo)Al_x$ layer and layer of the matrix damaged by the fuel particles

Composition	Coating thickness, μm		$U,Mo)Al_x$ layer thickness, μm	Layer of the matrix damaged, μm	Thickness of all layers, μm
	Before irradiation	After irradiation			
UMo/Al	-	-	4.9	7.7	12.6
UMo/UO_2/Al	~0.3	~0	4.6	8.1	12.7
UMo/Nb/Al	1.1-2.3	1.0	3.3	6.3	10.6
UMo/Zr/Al	0.9-2.1	1.0	0.8	6.8	8.6
UMo/Al-12%Si	-	-	4.2	9.5	13.7
UMo/UO_2/Al-12%Si	~0.3	~0	3.3	7.2	10.5

The metal coatings thickness is nearly two times less than the initial one (see Table). However the coatings have preserved their integrity and were strongly coupled with the fuel particles and the interaction layer. The oxidic coatings on the irradiated samples have not been observed. This is probably conditioned by either their small thickness or their interaction with the aluminium matrix.
The analysis of the data on the mini-element swelling and the $(U,Mo)Al_x$ layer thickness gives evidence of the absence of correlation between them. This may be presumably because of both the heterogeneous distribution of the fuel particles along the fuel core and the differences of the chemical composition of the very $(U,Mo)Al_x$ layer.

6. Conclusions

The reactor test of the mini-elements containing the U-9%Mo alloy fuel particles without the coatings and with Nb, Zr-1%Nb alloy and UO_2 barrier coatings dispersed in the technically clean Al (0,3% Si) and Al-12%Si alloy matrix have been successfully carried out.
To the test end the next mean irradiation parameters values have been achieved: the fuel flux density – 60 W/cm^2, the fission rate 4.0×10^{14} fis./(cm^{3}c), the fission density – 4.1×10^{21} fis./cm^3, the fuel temperature ~ 92°C, the equivalent burn up - 60%.
The positive influence of the Nb, Zr-1%Nb alloy and UO_2 barrier coatings and the additions of Si to the Al matrix on the mini-element swelling reduction has been observed. Besides, the oxidic coatings and the Si addition to the Al matrix act synergistically leading to the least swelling among the investigated compositions.
The presence of the oxidic and metal coatings and the Si additions in the Al matrix reduces the formation rate of the interaction layer of the $(U,Mo)Al_x$ type.
The least $(U,Mo)Al_x$ layer thickness has been observed in the composition with the Zr-1%Nb alloy barrier coating.
The metal barrier coatings have preserved their integrity, but their thickness has been reduced nearly two times. The presence of the oxidic coatings on the surface of the fuel particles has not been observed after irradiation because of their small initial thickness (<0.3 μm).

References

[1] Birzhevoy G.A., Karpin A.D., Popov V.V., Sugonyaev V.N. Some Approaches to Solving the Problem of Diminishing the Interaction between U-Mo Fuel Particles and Al Matrix // RRFM-2006 10th International Topical Meeting on Research Reactor Fuel Management, Sofia, Bulgaria, 30 April - 3 May 2006.

PLACA/DPLACA SIMULATION OF

MONOLITHIC/DISPERSE UMo PLATES

ALICIA DENIS

Departamento Combustibles Nucleares, Centro Atómico Constituyentes, Comisión Nacional de Energía Atómica, Av. del Libertador 8250, 1429, Buenos Aires. Argentina

Escuela de Ciencia y Tecnología, Universidad Nacional de General San Martín, M. de Irigoyen 3100, 1650, Pcia. de Buenos Aires, Argentina
denis@cnea.gov.ar

ALEJANDRO SOBA

Departamento Combustibles Nucleares, Centro Atómico Constituyentes, Comisión Nacional de Energía Atómica, Av. del Libertador 8250, 1429, Buenos Aires. Argentina
soba@cnea.gov.ar

ABSTRACT

The codes PLACA/DPLACA simulate the irradiation behavior of plate-type fuels under normal operation conditions. They correspond to monolithic and dispersed fuels, respectively. The codes have a modular structure and contain about thirty interconnected and mutually dependent models. They make possible a detailed simulation of the evolution of the more relevant physical parameters of a plate-type fuel element during its permanence within a reactor. In the particular case of the U-Mo/Al system, a model is included to give account of the interaction layer that develops between the alloy and Al. The model assumes that interdiffusion of Al and U through the layer is the rate determining step. The associated Stefan problems are numerically solved. This presentation includes the simulation of irradiation experiments performed with U-Mo/Al fuels: monolithic miniplates fabricated in CNEA and irradiated at the ATR and dispersed-fuel plates belonging to the IRIS-2 experiment. Comparison of the calculation results with the experimental data evidence in these and in previously analyzed cases, the correct performance of the models involved and the good coupling of the ensemble.

1. Introduction

PLACA and DPLACA, which can be considered as two versions of the same code, employ the finite elements method in Cartesian coordinates with linear rectangular elements to solve the differential equations corresponding to the thermal and elastic-plastic problems. Two perpendicular views (*xy* and *yz*) of the plate are considered. They make possible a global analysis of the plate since, when combined yield a quasi-three dimensional description of the system. Transverse sections (*xy*) can be analyzed at any location of the plate, particularly at those considered more critical, allowing a detailed analysis of all the variables involved.

Special attention is paid to the candidate fuel constituted by U-Mo particles dispersed in Al. This system exhibits a singular behavior due to the interaction layer that grows around the fuel particles and can provoke uncontrolled swelling. A model has been developed to give account of this phenomenon [1,2]. It assumes that the kinetics of both interfaces is determined by diffusion of U and Al through the layer. From the computational point of view this is performed by numerically solving the diffusion equations of two species along with the Stefan problems associated to the two moving layer boundaries. This gives to the code a realistic tool since the consumption of fuel particles and matrix is

strongly dependent on the longitudinal position of each finite element, i.e., on the local power history and the consequent temperature distribution.

2. Modelling and calculation procedure

To perform the finite element calculations, the domain is subdivided into linear rectangular elements. The two sections of the plate considered in the codes are shown in Figure 1.

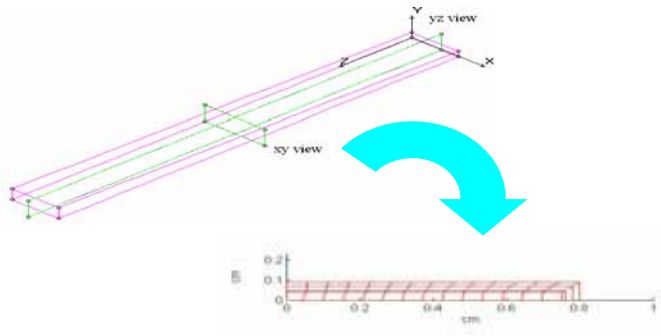

Figure 1: Sections xy *and* yz *of the fuel plate considered in PLACA/DPLACA*

The temperature distribution in the *yz* section is not symmetrical along *z*, but symmetry exists in the *xy* section along both axes. Then, the calculation domain used in the *xy* view is one-forth of the section while that used for the *yz* view contains one half of the respective section. Domain discretization is performed by a mesh generator included in the code. The input parameters are the fuel geometry, the constituent materials and the amount of ^{235}U within the plate, the particle shape and its size distribution if the fuel is of the dispersed type, the coolant velocity and mass flow, and the neutron flux or linear power history of the fuel plate. The history is divided into stationary periods and power ramps; these are divided into a number of stationary steps, at the programmer's choice.

The first calculation step is the temperature distribution which serves as input for the stress-strain distribution problem for which plane strain is assumed. A predictor-corrector algorithm is used to solve the non-linear equations associated to the thermal-elastic-plastic problem. Within each finite element the temperature and power history are assumed uniform.

In the particular case of the U-Mo particles dispersed in Al, a representative volume constituted by a U-Mo particle, the interaction layer, a pores shell and the surrounding Al matrix is chosen in each finite element, all of them according to the proportions in which they are present in the whole material. The interdiffusion equations in spherical coordinates are then solved to determine the intermetallic growth and the corresponding decrease of the amount of fuel and matrix. If the particles are not spherical, a correction factor is applied. The decrease of the initial porosity during fuel burnup (densification) is considered. The results obtained in each representative volume are extended to the volume of the corresponding finite element and then to the whole fuel plate volume. In this procedure the particle size distribution is taken into consideration.

Swelling and growth of the intermetallic layer [3,4] take place during fuel life time and modify the volume fraction of the diverse fuel plate constituents. These processes also deteriorate the heat conduction and, in consequence, temperature within the plate increases; in consequence, layers growth and swelling accelerate even in a constant power regime. For this reason, the code actualizes the temperature distribution after a given burnup interval. Moreover, some of the physical parameters of the system change due to irradiation effects and need also to be actualized.

The code considers aluminum or Zircaloy as possible cladding materials. If it is made of Al, the superficial oxide layer on the external cladding surface is taken into account since its low thermal conductivity is responsible for an extra temperature increase in the domain. Its growth rate depends on

the working temperature and on the water composition. The code contains four models to give account of this growth [5]. If the cladding material is Zircaloy the oxide layer is not considered since its growth is very slow at the normal operation temperatures of research reactors.

To analyze the stress and strain distributions, the total strain vector $\{e\}$ is written as $\{e\} = \{\varepsilon\} + \{\varepsilon^{th}\} + \{\varepsilon^{sd}\}$ where $\{\varepsilon\}, \{\varepsilon^{th}\}$ and $\{\varepsilon^{sd}\}$ represent the strains due to the applied loadings, to thermal expansion and to swelling-densification, respectively.

After determining the temperature and particle radius in each finite element, the code solves at every time step the interdiffusion problem, evaluates the particle and matrix consumption, the growth of the interaction layer and of the porosity annulus and actualizes the volume fraction of each component. These values are then averaged for the whole domain. For non-spherical particles six shape factors are included to give account of different area/volume relations.

3. Test Cases

Both codes were applied to simulate several irradiation histories. In this work the predictions of PLACA are compared with destructive and non-destructive analysis of two miniplates of monolithic LEU, U-7Mo cladded in Zircaloy-4, elaborated in CNEA and irradiated in the ATR during the RERTR-7A experiment [6]. Also, some fuel plates of dispersed UMo particles from the IRIS-2 experiments [7] are simulated with DPLACA.

3.1 Monolithic UMo: MZ25 and MZ50

The monolithic miniplates identified as MZ25 and MZ50 were fabricated by hot co-lamination of U-7Mo plates sandwiched with two Zry-4 plates and designed to have a total thickness of 1 mm and a meat thickness of 0.25 and 0.50 mm, respectively. The dimensional and physical characteristics of the miniplates are summarized in Table 1, along with the available PIE results [8] which include Gamma scanning, dimensional measurements and sectioning for metallographic inspection and determination of burn-up by chemical methods. The Table also includes the results of simulations with PLACA.

Table 1. Dimensional and physical characteristics of miniplates MZ25 and MZ50. Comparison between numerical and available experimental results.

Miniplate	MZ25		MZ50	
Dimensions (mm)	73×18.8×0.25		71×18.6×0.50	
Density (gU/cm^3)	16.5		16.3	
	Exper.	**Num.**	**Exper.**	**Num.**
Burn-up (%)	38	34	33	30
Fission density $\times 10^{21}$ (f/cm^3)	2.7	2.8	2.3	2.5
Max. heat flux (W/cm^2)	135	127	217	235
Max. internal temp. (°C)		100		163
Max. external temp. (°C)		60		78
Total swelling (%)	3.6	5		4.8
Oxide layer (μm)	2.6	0.0		0.0

3.2 Disperse UMo: IRIS-2

Plates fabricated with more than about 50 vol% of atomized U-7wt%Mo powder with a density of 8.3gU/cm^3 and a porosity of 1.5% were used in the IRIS-2 experiment. Figure 2 shows the evolution of temperature (in a *xy* view calculation) at the meat centreline, at the oxide layer-cladding metal

interface, at the external face of the oxide layer and of the coolant at the maximum power plane. The power history used was obtained from [9].

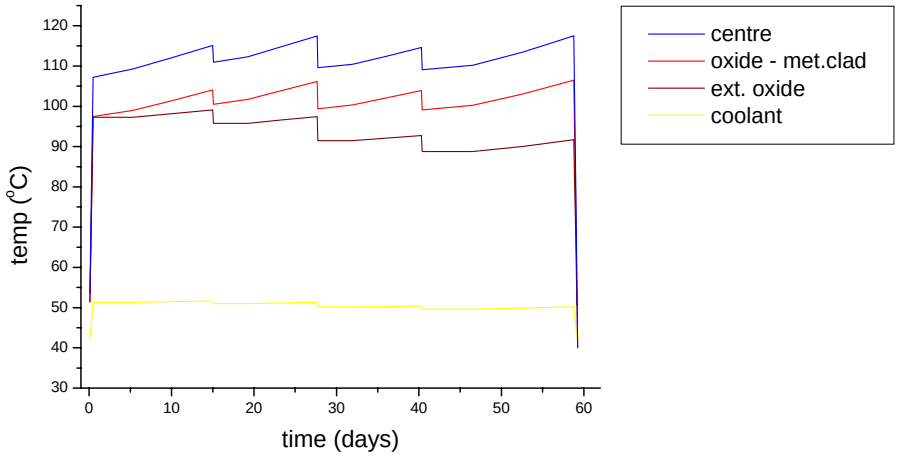

Figure 2: Temperatures of the plate at the maximun flux plane.

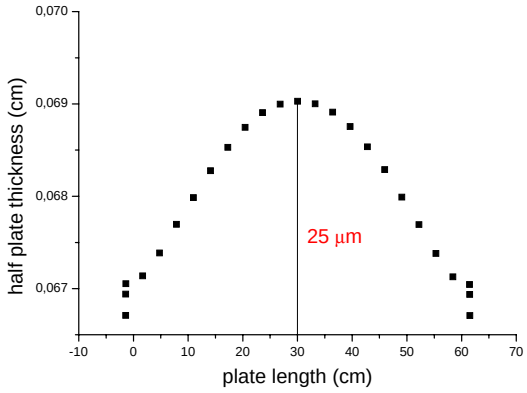

Figure 3. Thickness of one-half of the plate at EOL predicted by DPLACA.

Figure 3 shows the thickness of one-half of the plate along its length at EOL. A *yz* view calculation is used in this case. Burnup, volume percent of UMo, Al and intermetallic variation along the plate length are shown in Figure 4.

4. Discussion

Previous results obtained with PLACA and DPLACA [10] and those presented in this case show a good agreement with the experimental results and with those obtained with other codes. They make possible a detailed simulation of the evolution of the more relevant physical parameters of a fuel plate during its permanence within a reactor. The results evidence the correct performance of the models involved and a good coupling of the ensemble. The modular structure of both codes allows testing and replacement of the different particular models included. Moreover, the *xy* view allows a detailed analysis at any section of the plate, particularly at those considered more critical. Superposition of views *xy* and *yz* makes possible a global analysis of the plate.

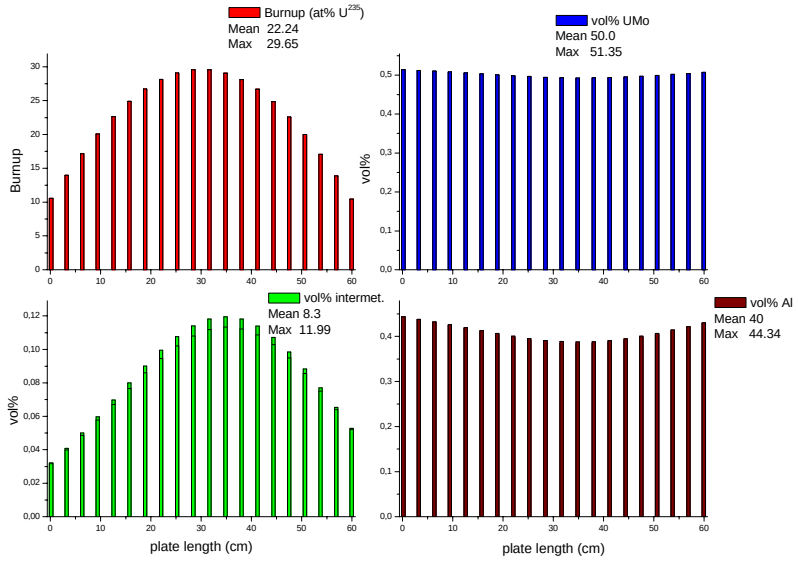

Figure 4 Burnup, Volume % of UMo, Intermetallic and Al vs. plate length at EOL.

References

[1] A. Soba, A. Denis, *An interdiffusional model for prediction of the interaction layer growth in the system Uranium-Molybdenum / Aluminum*, Journal of Nuclear Materials (accepted for publication).

[2] A. Soba, A. Denis, "PLACA/DPLACA: código para la simulación de un combustible tipo placa monolítico/disperso", Revista Internacional de Métodos Numéricos para Cálculo y Diseño en Ingeniería, Barcelona, España (to be published).

[3] A.Leenaers, S. van den Berghe, E.Koonen, C.Jarousse, F.Huet, M.Trotabas, M.Boyard, S.Guillot, L.Sannen, M.Verwerft, *Post-irradiation examination of uranium-7 wt% molybdenum atomized dispersion fuel* , Journal of Nuclear Materials 335 (2004) 39-47.

[4] H.J.Ryu, Y.S.Han, J.M.Park, S.D.Park, C.K.Kim, *Reaction layer growth and reaction heat of U-Mo/Al dispersion fuels using centrifugally atomized powders*, Journal of Nuclear Materials, 321 (2003) 210-220.

[5] Y.S. Kim, G.L. Hofman, N.A. Hanan, J.L. Snelgrove, *Prediction model for oxide thickness on alumium alloy cladding during irradiation*, International Meeting on Reduced Enrichment for Research and Test Reactors, Chicago, USA, 2003.

[6] E. Pasqualini, *Dispersed (coated particles) and monolithic (zircalloy-4 cladding) UMo miniplates.* Proceedings RERTR 2005, Boston, USA.

[7] F. Huet, V. Marelle, J. Noirot, P. Sacristan, P. Lemoine, *Full-sized plates irradiation with high UMo fuel loading. Final results of IRIS 1 Experiments*, International Meeting on Reduced Enrichment for Research and Test Reactors, Chicago, USA, 2003.

[8] E. Pasqualini, *Advances and Perspectives in U-Mo Monolithic and Dispersed Fuels*, RERTR-2006, Oct.29-Nov.2, 2006, Cape Town, South Africa.

[9] S.Dubois, personal communication.

[10] A.Soba, A. Denis, *Simulation with PLACA/DPLACA of monolithic and dispersed fuel plates*, RERTR 2006, Oct.29-Nov.2, 2006, Cape Town, South Africa.

STRUCTURE STUDIES OF DISPERSED U-Mo FUEL AFTER IRRADIATION AND ISOCHRONOUS ANNEALING WITHIN THE TEMPERATURE RANGE OF 150 - 580 ^{O}C BY THE NEUTRON DIFFRACTION METHOD

O.A. GOLOSOV, V.B. SEMERIKOV, A.E. TEPLYKH, M.S. LYUTIKOVA
The Institute of Nuclear Materials
Zarechny, Sverdlovsk region, 624250, Russia

E.F. KARTASHEV, V.A. LUKICHEV
NIKIET
Moscow, 101000, Russia

ABSTRACT

The data about the phase and structural state of (U, Mo)Al_x layer have been scarce so far, thereby precluding from development of the measures for reducing the rate of layer growing.
This paper presents the results of the structure study on the dispersed uranium-molybdenum fuel after irradiation to different burn up levels from 33 to 97% and one-hour annealings within temperatures of 150 to 580 ^{o}C by the neutron diffraction method.

1. Introduction

The experiments with U-Mo dispersion fuel which were performed in the frame of the RERTR national programs have revealed formation of an interaction layer such as (U,Mo)Al_x. For the present time neither the phase composition, nor the structural parameters of (U,Mo)Al_x layer have been determined. There are only some scattered experimental data on chemical composition of this layer where the content of Al varies as corresponds to compounds from (U,Mo)Al_3 to (U,Mo)Al_8 [1, 2]. It is assumed that under irradiation temperature below 200 ^{o}C (U,Mo)Al_x layer would be amorphous. No experimental data to confirm this assumption are available yet. The only study [3] has demonstrated that the UAl_3 crystal phase formed in the fuel rods at 20 % burnup and irradiation temperature of fuel meat exceeding 200 ^{o}C. The lack of data on structure and phase composition of (U,Mo)Al_x layer precludes from developing the measures aimed at reducing or complete inhibition of the layer growth.

The present paper gives the results of studying the structure of U-Mo dispersion fuel following its irradiation in IVV-2M reactor (Zarechny) up to the different values of burnup (from 33 to 97 %) and after annealing during 1 hour in the temperature range from 150 to 580 ^{o}C performed by the neutron diffraction method.

2. Materials and the experiment technique

The specimens of 40x8x1.3 mm size cut at different axial points from the fuel elements of the combined FAs of KM003 and KM004 types tested in IVV-2M reactor. The specimens are characterized in Table 1. Two specimens G13 and G100 were taken from KM003 FA, which corresponded to the axial positions of the specimens G96 and G97 from KM004 FA (Fig.1). It should be pointed out that G98 specimen was cut from the fuel element portion, which was in the direct contact with the areas of cladding pillowing. The fuel meat of this specimen contained separated gas pores and their agglomerations as well as minor cracks up to 1.5-2 mm in length.

Each specimen contained two fuel claddings of 0.45 mm thick and one layer of the fuel meat of 0.45 mm thick. Three such specimens were combined into a single package for making the experiments on neutron diffraction.

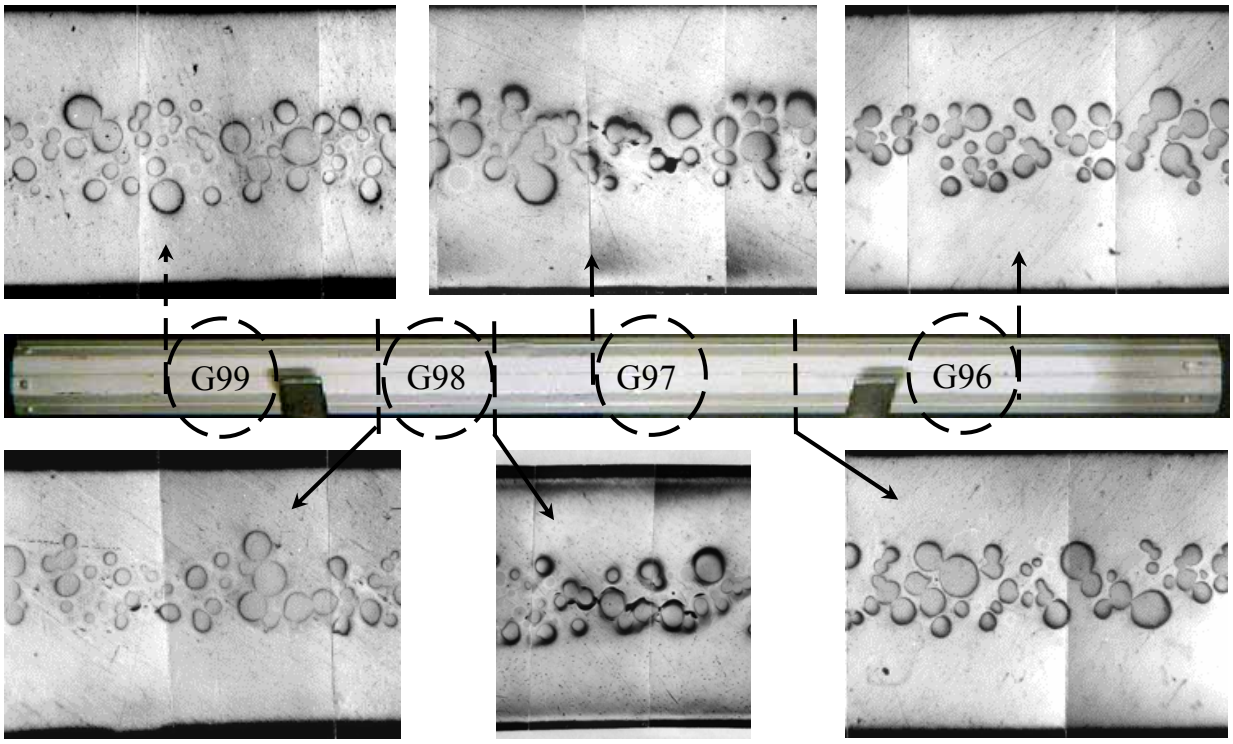

Fig. 1. Appearance of the fuel element from KM004 FA and macrostructure of the fuel meat at different axial cross-sections of the fuel element

Specimen No.	FA No.	Bu[1], %	φ, 10^{14} fiss/(cm^3s)	Ψ, 10^{21} fiss/cm^3	T_{BOL}, ^{0}C	q_{BOL}, W/cm^2	IL[2], μm	Volume ratio of phases in a specimen, %			
								Al	U-Mo	IL	Al_{FP}[3]
G13	KM003	32.9	2.6	2.1	43.5	48	1.2	87.0	12.1	0.9	13.4
G100	KM003	51.1	4.5	3.8	61.4	80	3.6	85.6	11.6	2.8	14.2
G96	KM004	55.1	3.1	4.1	48.6	66	3.5	85.7	11.6	2.7	14.2
G97	KM004	96.3	5.5	7.2	77.2	115	11.3	80.7	10.1	9.2	16.9
G98	KM004	96.9	5.7	7.3	85.3	118	11.2	80.8	10.1	9.1	16.8
G99	KM004	78.4	4.6	5.9	86.4	95	9.0	82.3	10.5	7.2	16.0

1) equivalent burnup;
2) thickness of (U,Mo)Al_x layer;
3) aluminum matrix damaged by fission products

Tab. 1. Characterization of specimens under testing

The neutron diffraction experiments have been performed at IVV-2M reactor (in Zarechny). The experimental data were obtained for the angular range from 5^o to 105^o by 2Θ with the step of 0.1^o. The spectra of all specimens were obtained at the first stage. After that three specimens (G96, G98 and G99) have been subjected to step-by-step, 50 ^{o}C each, annealing in the temperature range from 150 to 580 ^{o}C, annealing time was 1 h. Neutronograms were taken after each annealing.

3. Experimental results and their discussion

Fig. 2 shows the neutron spectra obtained for the specimens irradiated to the different burnups and after isochronal annealing for G96, G98 and G99 specimens. For the purposes of better demonstration, the spectra of each specimen are shifted along the intensity scale.

The specimens under testing contain the strong coherent reflexes from the following crystal phases (Fig. 2a): the alloy on the basis of γ-U-9% Mo, Al as the base of the aluminum matrix and fuel claddings made of SAV-1 alloy. Several other visible minor reflexes have been interpreted as those induced by Mo-based alloy ($Mo_{90}U_{10}$ phase) and UAl_3. Besides, some neutronograms at angles of 51-52 and 60 degrees show the traces of reflexes induced by γ-FeNiCr alloy caused by the stainless steel

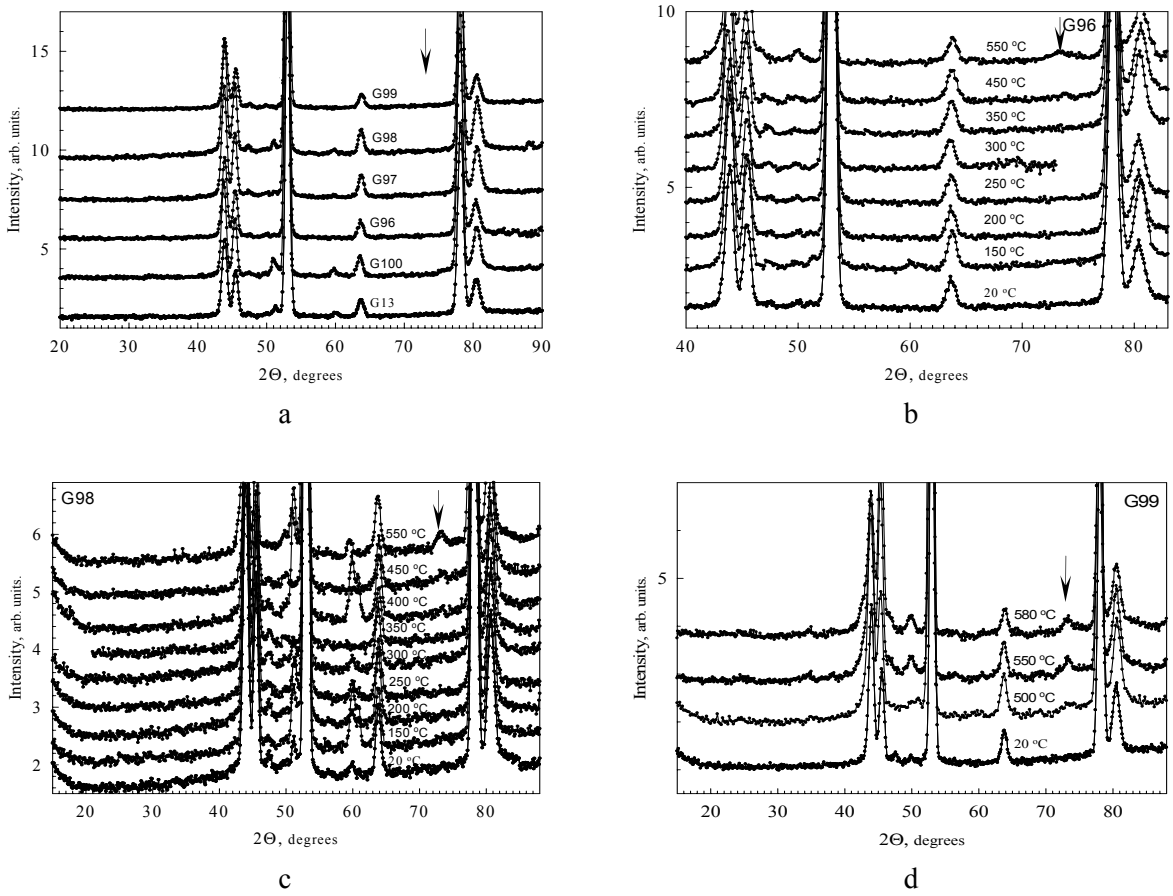

Fig 2. Neutron diffraction spectra for the specimens with different burnups (*a*) and after isochronal annealing in the temperature range of 150-580°C (*b-d*). The position of UAl_3 phase line (220) is marked with arrow.

position limiter placed inside the vanadium container. The spectra of specimens under testing did not include any reflexes corresponding to such intermetallide phases as UAl_2, UAl_4 or to the more complex structures based on U-Mo-Al system.

The thorough investigation of the diffraction spectra given in Fig. 2a made it possible to notice that reflexes corresponding to Al resulted in an increase of diffusion background caused by scattering of the amorphous Al-based phase at short-range order. This phenomenon can be clearly seen in Fig. 3 that illustrates the neutronograms for the specimens with minimum (G13) and maximum (G98) burnups, and minimum and maximum contents of $(U,Mo)Al_x$, i.e. 0.9 and 9.1 %, respectively.

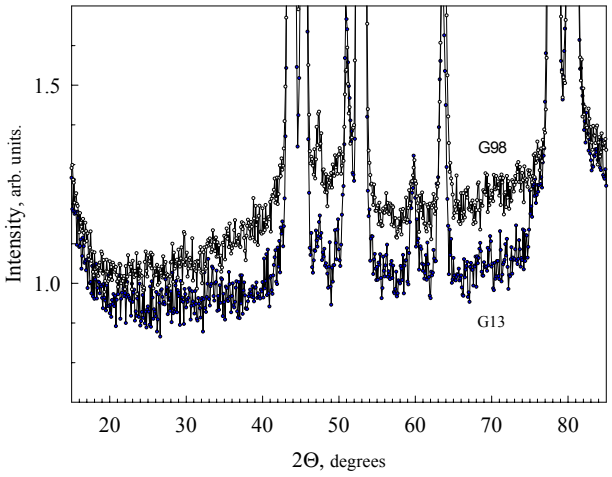

Fig. 3. Neutronograms of G13 and G98 specimens enlarged along the intensity

After processing of the experimental data given in Fig. 2a it is possible to observe that the contents of $Mo_{90}U_{10}$ and UAl_3 phases does not practically depend on burnup and makes up ~1.5 and ~0.5 %, respectively, Fig. 4. It is necessary to specify that the content of UAl_3 phase was found at the level of error for the determination of phases with content less than 1 %. At the same time the amount of Al and γ-UMo phases decreases as burnup rises, that is caused by the reaction between these phases:

volume ratio of Al is reduced by ~8 % as burnup rises from 33 to 97 %, whereas the content of γ-UMo phase decreases only by ~0.6 %. As a result of interraction between fuel particles under irradiation, the amorphous phase such as (U,Mo)Al_x is formed. The volume fraction of this phase could be estimated by the results of optical metallography. The fraction of (U,Mo)Al_x phase increases almost by an order of magnitude (from 0.9 to 9.1 %) as burnup rises from 33 to 97 %.

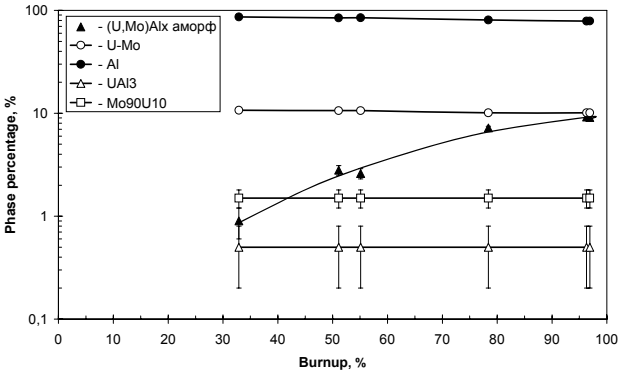

Fig.4. The effect of burnup on changing the content of Al, γ-UMo, UAl_3 and of the amorphous phase such as (U,Mo)Al_x

Figs. 2b-d show the neutronograms for G96, G98 and G99 specimens obtained at room temperature and after annealing. These neutronograms have the same specific features as those given in Fig.2a. Besides, it should be noted that at annealing temperature above 350 °C the reflexes increase at angles 49.6 and 72.8, which correspond to the reflections (200) and (220) for UAl_3.

Processing of the spectra shown in Figs. 2b-d allows to obtain the relationships between the content of the amorphous phase (U,Mo)Al_x and the crystal phase UAl_3 which are illustrated in Fig.5. Tthe percentage of any of these phases does not change until temperature is below 300°C. However, at annealing temperature above 350°C the specimens G96 and G98 demonstrate the noticeable amount of UAl_3 phase and the simultaneous decrease of the percentage of the (U,Mo)Al_x amorphous phase. It is necessary to point out that the curves for (U,Mo)Al_x have been plotted assuming that UAl_3 would be formed inside the former phase. At the same time it is possible that the UAl_3 crystal phase may be formed as a result of interaction between fuel particles and the Al matrix rather than as recrystallization of the (U,Mo)Al_x amorphous phase.

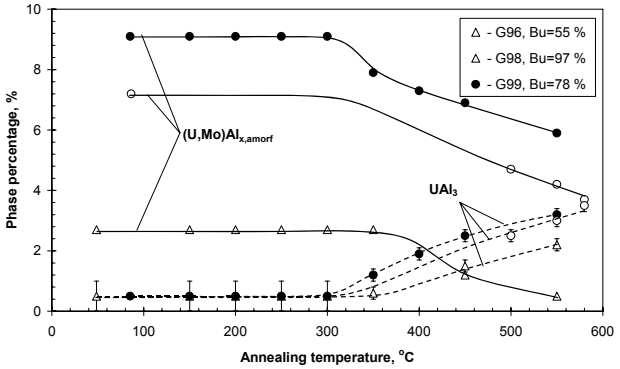

Fig. 5. The effect of annealing temperature on changing the content of the (U,Mo)$Al_{x,\ amorph}$ amorphous phase and UAl_3

Fig. 6 illustrates changes of UAl_3 content in the specimen under testing as a function of temperature. The figure also shows the calculated variations of the UAl_3 content which were obtained based on the equation derived from the data on heat test on interaction between unirradiated U-9%Mo alloy and commercial pure Al [4]:

$$\delta = 237.8 \cdot \tau^{0.40} \cdot \exp(-6310 / RT);$$

where δ – thickness of (U,Mo)Al_x layer, μm; τ – time, h; T – absolute temperature, K.

In accordance with data given in Fig. 6, for the specimens G98 and G99 with relatively thick (U,Mo)Al_x layers (11.2 and 9.0 μm, respectively) the noticeable percentage of UAl_3 phase, formed only due to thermal interaction between fuel particles and Al matrix, could be expected at temperature exceeding 450 °C. Thus, experimentally found values of UAl_3 percentage in G98 specimen at the annealing temperature in the range of 350-450 °C could be higher by almost an order of magnitude than the

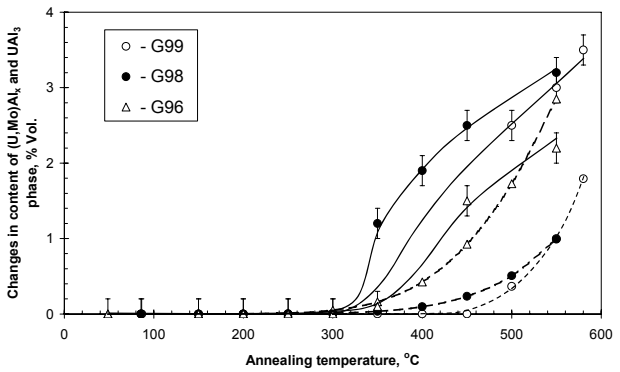

Fig. 6. The effect of annealing temperature on changes in percentage of UAl_3 phase: solid lines - experimental data, dashed lines – calculated values

expected values of UAl_3 percentage, if this phase would be the result of heating effect. Consequently, the occurrence of UAl_3 phase in G98 specimen can be explained only by the process of recrystallization in the $(U,Mo)Al_x$ amorphous phase. As is clear from the data in Fig.6, recrystallization of the $(U,Mo)Al_x$ amorphous phase begins in the temperature range between 300 and 350 ^oC. It is probably true also for the specimen G99 which was annealed only at 500-580 ^oC. However, the specimen G99 with less thick (by ~20 %) $(U,Mo)Al_x$ layer as compared with the specimen G98 has demonstrated almost equal percentage of UAl_3 phase at annealing temperature of 500 and 550 ^oC.

Unlike the specimens G98 and G99, the occurrence of noticeable amount of the heating UAl_3 phase could be found as early as at 350^oC for the specimen G96 where thickness of $(U,Mo)Al_x$ layer was less (3.6 μm). However, percentage of this phase is smaller compared to percentage of UAl_3 phase obtained during the experiment in the temperature range from 350 to 450 ^oC. If temperature is above 500 ^oC, percentage of UAl_3 phase of heating origin and obtained experimentally is almost the same.

4. Conclusions

It has been revealed that the specimens of fuel elements in KM003 and KM004 FAs with U-9%Mo dispersion fuel are characterized by the following phase composition: γ-UMo, Al, UAl_3, disordered Mo-based alloy $Mo_{90}U_{10}$ and amorphous phase with short-range order such as Al.

It has been demonstrated with accuracy of 1 % of the volume that tested specimens of FEs had no other crystal phases such as UAl_2, UAl_4 and more complex structures based on U-Mo-Al system.

It has been experimentally proven that tested specimens contained either amorphous or finely crystalline phase with the size of coherently dispersed particles less than 30 Å.

The following relationships of the said crystal structures as function of burnup and annealing temperature have been established:

- Percentage of γ-U-9%Mo phase depends only slightly on burnup;
- Percentage of UAl_3 crystal phase does not exceed 0.5 % and is almost the same in the range of burnups from 33 to 97 %;
- Percentage of $Mo_{90}U_{10}$ phase is constant and equal to ~1.5 % and hardly depends on burnup;
- Percentage of amorphous phase such as $(U,Mo)Al_x$ depends on irradiation parameters and increases as fuel burnup rises;
- As annealing temperature increases, percentages of the main phases such as γ-UMo, $Mo_{90}U_{10}$ and Al practically do not change;
- In the range of annealing temperature from 150 to 300-350 ^oC percentages of the amorphous phase and UAl_3 practically do not change;
- Annealing at temperature above 300-350 ^oC results in crystallization of the amorphous phase with formation of the UAl_3 intermetallide phase. Percentage of the latter increases, as annealing temperature rises, being as high as ~30-50 % of the $(U,Mo)Al_x$ amorphous phase at annealing temperature of 550-580 ^oC.

Under the specified annealing temperatures (T=150-580 ^oC, t=1 h) the entire percentage of the $(U,Mo)Al_x$ amorphous phase could not be transformed to the crystal state.

It has been determined that temperature of 300 ^oC is the boundary value in terms of accelerated formation of the UAl_3 intermetallide phase.

5. References

[1] J.M. Hamy, F. Huet, B. Guigon, P. Lemoine et al. Status of March 2003 of the UMo development program // 7th Int. Mtg. RRFM 2003, Aix en Provence, France, 9-12 march 2003.

[2] A. Leenaers, S. Van den Berghe, L. Sannen et al. Postirradiation observations on U-7%wtMo atomized dispersion fuel // 8th Int. Mtg. RRFM 2004, Munich, Germany March 2004.

[3] K.T. Conlon, D.F. Sears. Neutron powder diffraction of irradiated low-enriched uranium-molybdenum dispersion fuel // 10th Int. Mtg. RRFM 2006, Sofia, Bulgaria, April-May, 2006.

[4] V.G. Aden, V.V. Popov, A.Ye. Rusanov, V.M. Troyanov. Investigations of a reduced enrichment dispersion fuel (U-Mo alloy in aluminium matrix) for research reactor fuel pins // 3th Int. Mtg. RRFM'1999, Bruges (Belgium) 28-30 March 1999.

REMOVAL OF SPENT NUCLEAR FUEL FROM KURCHATOV INSTITUTE RESEARCH REACTORS FOR REPROCESSING: PROBLEMS AND PLANS

V.G. VOLKOV, A.A. DROZDOV, YU.A. ZVERKOV, S.M. KOLTYSHEV, I.A. KUZNETSOV, V.D. MUZRUKOVA, S.G. SEMIENOV, S.YU. FADIN

Russian Research Centre "Kurchatov Institute"
1 Kurchatov Square, 123182 Moscow, Russia

ABSTRACT

The paper presents problems and main results of activities on removal of spent nuclear fuel (SNF) from research reactors of the Kurchatov Institute for reprocessing. Up to 1990, standard spent fuel assemblies (SFAs) from the Institute reactors were on a regular basis removed to Mayak enterprise for reprocessing. The scheme of removing the standard SFAs was based on the use of casks of TUK-19 type. Between 1990 and 2003, no work on SNF removal from the Institute was conducted, but in 2004-2005, three shipments of SFAs were completed. In 2006 the work on SNF removal was continued. A special feature of this shipment lay in the fact that new generation casks of TUK-128 type were used for transportation of the SFAs. Main design features of the TUK-19 and TUK-128 casks are described. The Institute spent fuel includes almost all kinds of nuclear fuel used in research reactors of Russian design. Classification of the Institute SNF according to Mayak requirements for acceptance of spent fuel for reprocessing is presented. In order to perform further activities on removal of SNF, a "Programme of Management of Research Reactor SNF Accumulated at the Kurchatov Institute Site" has been developed. The main activities on preparation of SFAs for removal, the procedure and schedule of SFA removal for reprocessing are described. It is expected that implementation of the Programme will establish a well-documented basis for organization of further activities on decommissioning of shutdown reactors at the Institute.

1. Introduction

Kurchatov Institute, established in 1943, is currently one of the largest scientific nuclear centres of Russia. Complex solution of the problem of safe and environmentally clean energy generation on the base of nuclear fission reactions, which required a considerable experimental base, was one of the Institute's main activity areas.

The Institute's experimental complex has operated the total of 12 research nuclear reactors of different types (the first commissioned in 1946), as well as about 20 critical and sub-critical experimental facilities and 3 "hot" material research laboratories for works with irradiated nuclear fuel.

Currently the Institute has 6 research reactors in operation. Another six reactors have been shut down in various years, and some of them have been dismantled, and some others now expect decommissioning. Research reactors, which form the Institute's experimental reactor base, are listed in Table 1, together with their basic parameters.

For many years of its experimental reactors' operation, the Institute has accumulated considerable amounts of spent nuclear fuel (SNF) on its site.

Currently over 5 tons of SNF (including over 900 spent fuel assemblies (SFAs) and their fragments) with total activity exceeding 10^{16} Bq (over 3×10^{5} Ci) is stored in the Institute's territory. This

circumstance determines the urgency of SNF removal from the Institute, the site of which is situated within the borders of Moscow.

Reactor	Reactor type	Dates of start-up/ reconstruction	Capacity/after reconstruction, MW	Status
F-1	Uranium-graphite reactor	1946	0.024	In operation
RFT	Channel-type uranium-graphite reactor	1952/1957	10.0/20.0	Partially dismantled (1962)
VVR-2	Tank-type water-water reactor	1954/1960	0.3/3.0	Dismantled (1983)
IRT	Pool-type reactor	1957	2.0	Dismantled (1979)
OR	Tank-type water-water reactor	1960/1983-86	0.3/0.3	In operation
MR	Channel-type in-pool reactor	1963/1967	20.0/50.0	Shut down (1993)
Romashka	High-temperature reactor with thermoelectric converter	1964	0.04	Dismantled (1967)
Gidra	Homogeneous solution pulse reactor	1972	0.01-30.0 MJ (in pulse)	In operation
Topaz-2	High-temperature reactor with thermionic converter	1973	0.1	Dismantled (1986)
IR-8	Pool-type uranium-graphite reactor	1981	5.0 (design - 8.0)	In operation
Argus	Homogeneous solution reactor	1981	0.02	In operation
Gamma	Tank-type water-water reactor	1982	0.125	In operation

Tab 1: Basic parameters of research reactors of the Kurchatov Institute

2. Storage conditions and classification of the Institute's SNF

SNF accumulated on the Institute's site is represented by spent fuel assemblies (SFAs) and fuel elements from: already dismantled RFT, IRT, Romashka, Topaz-2 and VVR-2 reactors; reconstructed OR reactor; and MR reactor, which was shut down for decommissioning.
SNF was removed to on-site temporary storage facilities created in the Institute's territory in order to meet the research reactors' operation requirements, and to assure safe management of spent fuel.
SNF from RFT, IRT and MR reactors is stored in the central "dry" storage facility situated on the main site of the Institute.
SNF from Romashka and Topaz-2 reactors is stored in the "dry" storage facility of the "R" complex, also situated on the main site of the Institute.
SNF from VVR-2 and OR reactors is stored in "aqueous" storage facility of the "Gas Plant" complex situated on the supplementary site of the Institute.
The technical condition of all temporary SNF storage facilities existing in the Institute's territory conforms to the contemporary requirements related to physical protection and nuclear/radiation safety assurance.
It should be said that the SNF accumulated in the Institute comprises almost all types of nuclear fuel ever used in research reactors of Russian design. This SNF includes not only the working (regular) SFAs of research reactors, but also experimental fuel assemblies and elements used in reactor research and tests of various structures, fuel compositions and construction materials. For this reason, the Institute's SNF is characterized by diverse structural features, fuel composition types, U-235 fuel enrichments, fuel burnup depths, cooling periods, and status of fuel assembly components and construction materials used. SFAs also include leaking fuel assemblies, as well as assemblies containing defective fuel.

Taking into account the requirements the spent fuel should meet to be accepted for reprocessing by PA Mayak, the Institute's SNF could be divided into the three following groups:

- reprocessable fuel, i.e., fuel meeting PA Mayak's acceptance requirements;
- conditionally reprocessable fuel, i.e., fuel not quite fit for reprocessing at PA Mayak, requiring repackaging into leak-tight canisters and baskets, as well as additional coordination of its acceptance for further reprocessing;
- irreprocessable fuel, including defective fuel, which requires long-term storage, since currently there is no reprocessing technology for it.

More details on the Institute's SNF are given in Table 2.

№	Reactor	SFA type	SFA					Fuel elements
			Reprocessable SNF			Irreprocessable SNF		
			completely	conditionally	defective	leak-tight	defective	
1	MR	Pilot	-	-	226	-	-	970
2	MR	Fuel element fragments	-	-	-	-	-	16
3	RFT	Working	-	-	-	108	90	-
4	IR-8	Working	8	-	-	-	-	-
5	Topaz-2	Working-1	-	151		-	-	-
6	Topaz-2	Working-2	-	26	18			
7	Ромашка	Working	-	-	-	11	-	-
8	VVR-2, OR	Working-1	155	-	39	-	-	-
9	VVR-2, OR	Working-2	-	68	17	-	-	-
10	Total spent fuel assemblies or elements		408		300	119	90	986
			708			209		
11	TOTAL		917					

Tab 2: Types and numbers of SFAs to be removed from the Institute's site (status of 2007)

3. Current status of works on SNF removal from the Institute's territory

Before 1990, the working SFAs of the Institute's research reactors have been regularly shipped for radiochemical reprocessing to the specialized enterprise – PA Mayak. Then the technological scheme of SFA transportation has been based on using old-generation TUK-19 shipping casks and TK-5 railway carriages.

Between 1990 and 2003, SNF removal works in the Institute have been frozen because of insufficient financing. In 2004 the Institute resumed SNF removal operations. In 2004-2005, three batches of the Institute's working SFAs were prepared and delivered to the destination on the basis of the restored shipping scheme using TUK-19 transportation casks.

In November 2004 and in March 2005, two special trains delivered 128 working SFAs from MR reactor (64 SFAs in each train) to PA Mayak.

In April 2005, the transportation of the third batch of 64 SFAs was prepared and carried out, again using TUK-19 transportation casks. SFAs sent by this train included spent fuel assemblies from the physical model of MR reactor.

The regular SNF loading and transportation system operating inside MR reactor premises was used for the transportation of MR physical model. In the preparatory process before MR physical model's SFA removal, the technical state and parameters of 70 assemblies were analysed, and 64 assemblies were

selected for transportation. A special certificate was then compiled for each assembly, indicating initial fuel parameters, fuel irradiation regimes and other data required by PA Mayak.
In 2006, the Institute continued its SNF removal activities, and shipped another 40 working SFAs from IR-8 reactor to PA Mayak.
This batch had a pilot status, because it used a new-generation TUK-128 shipping cask to contain and transport the fuel. That's why one of the principal goals of this SNF shipment was to confirm the efficiency of this new-generation shipping cask.

4. TUK-19: structural features and SNF loading/transportation scheme

TUK-19 shipping cask is intended for transporting research reactor SFAs, and includes the container No 19 and the basket. TUK-19 has the following basic technical parameters:

Transportation index	20
Mass, kg	4 750
Maximum U-235 fuel enrichment, %	below 90
Maximum residual power, W	below 112
Outside surface gamma dose equivalent rate, mrem/h	below 200
Surface temperature, °C	
- maximum	60
- minimum	-50

After SFAs were loaded, the container is filled with air or air/inert gas mixture. Structural layout of TUK-19 shipping cask is shown in Fig. 1.
TUK-19 shipping casks are transported on special TK-5 railway carriages, which provide vertical positioning, reliable fastening and transportation of eight TUK-19 shipping casks, and meet the technological requirements of SNF transportation.
TK-5 carriage is a four-wheel transporter with a body coated with stainless steel from the inside and partitioned by walls into one cargo section and two auxiliary rooms. The cargo section contains a frame with 8 cells, in which TUK-19 shipping casks are installed and fixed with special grips. The cargo section deck is made in form of two flaps opened using hydraulic or manual drive. The cargo section also contains decontamination solution and radioactive waste collecting tanks, the control panel and mechanisms opening the deck flaps, as well as spare parts and accessories.
The special train transporting the SNF in TUK-19 casks includes: a locomotive; a cover carriage; a carriage for PA Mayak escort team; an armed guard team carriage; two TK-5 carriages; and another cover carriage.
PA Mayak is an official owner of TK-5 carriages and TUK-19 casks.
All three shipments used the following technology of loading SFAs into TUK-19 and TUK-19 – into TK-5 carriages.
The upper lid was removed from TUK-19, and the cask was installed (using a crane) on a special rail-guided cart, together with the overload transfer cask. After that, TUK-19 and the transfer cask were delivered on the cart to SNF storage premises.
Then the protective plug was removed using the frame crane from the storage cell containing a metallic canister with SFAs to be shipped. Metallic canisters used for SFA storage in the storage cells are equipped with special grips. After removing the protective plug, the first operator, under the shady shielding, hooked the frame crane to the canister and then left the storage premises. The second operator, using video monitoring and frame crane remote control systems, removed the canister containing SFAs from the storage cell and loaded it into the transfer cask. After that, the first operator re-entered the storage area, unhooked the frame crane from the canister, hanged the SFA grip on the frame crane hook, hooked the SFA to it, and left the area again.
Then the SFA was removed – using the frame crane controlled remotely – from the canister placed into the transfer cask, and loaded into a fixed TUK-19 cask cell. Then three other SFAs were loaded into TUK-19 in accordance with the same order. After the last (fourth) SFA was loaded into TUK-19, the upper protective lid was installed on the cask using the frame crane, and loaded TUK-19 was removed from the storage premises on the rail-guided cart.

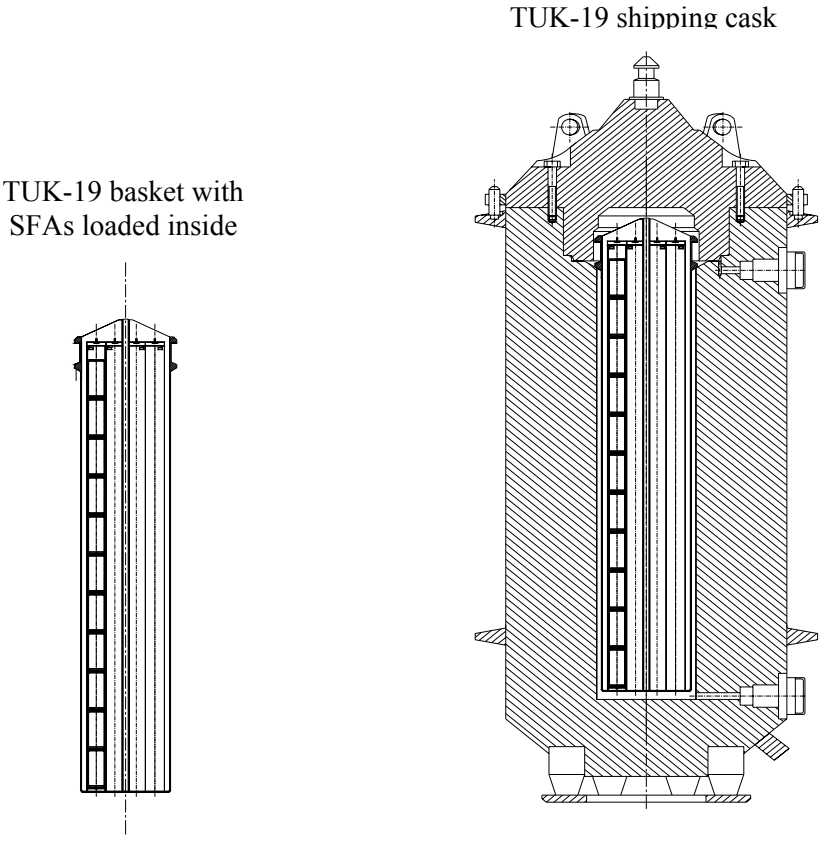

Fig 1. TUK-19 shipping cask layout

After all TUK-19 casks were loaded in accordance with the above technology, the loaded casks were installed by a crane on a special car, and successively delivered to the transfer site organized at the Institute's railway spur, where they were loaded into TK-5 carriage using the truck crane.
Use of the above technology of loading and transportation of the Institute's SNF in TUK-19 and TK-5 carriage had the following benefits:

- over 30 years of SNF transportation experience using TUK-19 and TK-5;
- high reliability of this scheme of SNF transportation to PA Mayak (over time, almost all SNF shipments using TUK-19 and TK-5 were performed in routine conditions; only rarely – in normal conditions; and never – in accident conditions);
- since PA Mayak is the SNF conveyor and TUK-19 and TK-5 owner, the specialists from this enterprise participate in SNF acceptance for reprocessing from its earliest stage;
- PA Mayak discharges TK-5 and TUK-19 on a regular basis, so no development or manufacturing of additional equipment is required;
- no additional reloading of TK-5 with loaded TUK-19 casks is required on the way.

5. TUK-128: structural features and SNF loading/transportation scheme

Unlike TUK-19 shipping cask used earlier, TUK-128 is a dual-purpose shipping cask: its structural features allow using it for both transportation and storage of SFAs (up to 50 years long). Besides, TUK-128 has a larger capacity, which makes it possible to load up to 20 SFAs into it (compare with 8 SFAs loaded into TUK-19).
TUK-128 shipping cask has the following basic technical parameters:

Outside diameter of container body, without dampers, mm	1120
Inner diameter of container body, mm	520
Container diameter including journals, mm	1310
Container cavity height, mm	960

Container height including lids, mm	1520
Container height, including top and bottom dampers, mm	2250
Container body mass, with journals and facing, kg	7857
Outside lid mass, kg	445
Internal lid mass, kg	410
Unloaded basket mass, kg	256
Loaded container mass, without dampers, kg	9227
Loaded container mass, with dampers, kg	11534
Container body material	high-strength, nodular graphite cast iron

TUK-128 shipping cask layout is shown on Fig. 2.

TUK-128 casks are transported in ISO containers, which undergo a special modification beforehand. The ISO container modification includes the fabrication of improved elements fastening these containers to railway flatcar, as well as TUK-128 retention into the ISO container.

It should be noted that, since the required reloading equipment was not yet ready, the standard transfer cask of IR-8 reactor and the standard loading technology previously used for TUK-19 were refined and successfully used in the pilot SFA batch shipped in TUK-128 casks. For that reason, in the framework of preparing the pilot SFA transportation in TUK-128 casks, as well as other transportation, technological and other auxiliary equipment, it became necessary to develop and use in the working process the following organizing and technical documents:

- On-site transportation process flow diagrams of TUK-128 shipping cask, ISO container, standard IR-8 transfer cask and technological equipment management;
- On-site process regulations of IR-8 research reactor SFAs' loading into TUK-128 shipping cask;
- On-site programme of "cold" tests of TUK-128 cask and of the device intended for SFA loading into TUK-128.

In course of the pilot transportation, the SFAs from IR-8 reactor were loaded into TUK-128, and TUK-128 – into ISO container, in accordance with the following technological sequence.

Two TUK-128 in two ISO containers were delivered on the Institute's site on trucks and installed in the reloading area organized at the Institute's railway spur.

With the help of the crane, TUK-128 casks were removed from ISO containers. After their dumpers were removed, the truck loader successively delivered TUK-128 casks to MR reactor building.

On the site near the MR reactor building, TUK-128 casks were installed on a special cart and successively delivered to the MR reactor hall, where their outside and internal lids were removed.

After that, a conductor funnel was installed on the fixed cell of TUK-128, in which a standard SFA from IR-8 reactor should be loaded.

Standard SFAs from IR-8 reactor were delivered to MR reactor hall in a standard IR-8 under-load transfer cask. To do that, the standard transfer cask was first delivered to IR-8 reactor hall and installed on the transfer hatch of this reactor's cooling pond. Then the operator, using a special manual grip, moved the standard SFA of IR-8 to be loaded into TUK-128 from its cooling pond cell and installed it into this pond's loading socket. After that, the grip of the standard transfer cask was put in its downward position and fixed to the assembly; then the grip with the SFA fixed to it was put in upward position and drawn into the standard transfer cask. After that, the protective gate of the standard transfer cask was closed, and the truck loader delivered the transfer cask with SFA inside to the site near the MR reactor building and then to MR reactor hall.

In the reactor hall, the standard transfer cask was installed above the fuelling channel of the shield cell in the reactor hall. After that, the protective gate of the standard transfer cask was opened, and the standard SFA of IR-8 reactor was installed on the bottom of the fuelling channel using the transfer cask grip. Then the grip of the transfer cask containing the SFA was unhooked, and the transfer cask was removed from the fuelling channel. After that, the first operator entered the MR reactor hall, manually fixed the special grip (hanged in advance on the SFA crane hook), and left the reactor hall. Then the second operator, using the crane, removed the SFA from the fuelling channel, moved the SFA to TUK-128, and installed it into a cell of this cask's basket through the conductor funnel.

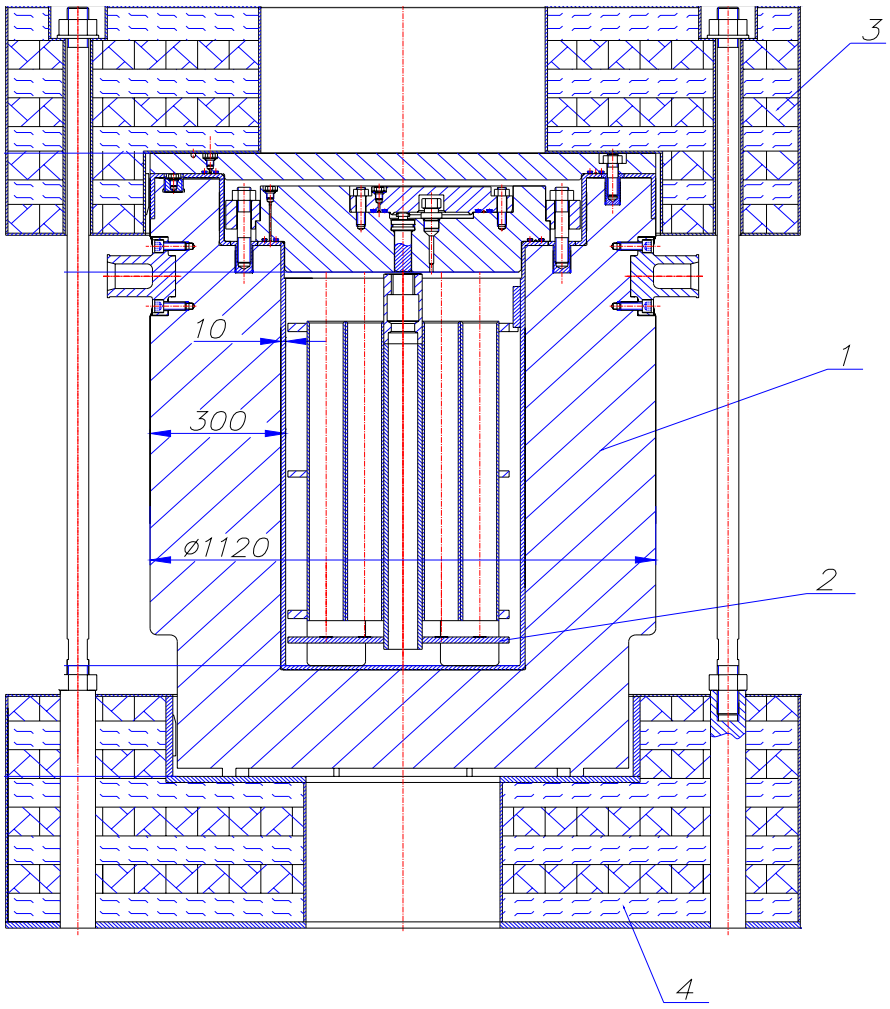

Fig 2. TUK-128 shipping cask layout:
1 – shipping cask; 2 – basket with SFAs; 3 – upper damper; 4 – lower damper

The grip was unhooked from the SFA automatically, after the SFA reached the bottom of the basket cell – thus, any further SFA movement was impossible. The conductor funnel was reinstalled on the next TUK-128 basket cell, and the standard transfer cask returned to the IR-8 reactor hall to receive a next SFA from this reactor.

After the twentieth (last) SFA was loaded into the cask basket, the internal and the outside protective lids were successively installed on TUK-128, and the cask's leak-tightness was checked. Then a special car delivered TUK-128 with SFAs inside to the transfer site at the Institute's railway spur, where the truck crane loaded TUK-128 into ISO container (already installed on a railway flatcar). Inside the container, TUK-128 was unfastened in accordance with the standard scheme.

6. Plans of further activities to remove SNF from the Institute's site

In order to organize and perform further activities on preparing and removing the SNF from the Institute, the "Programme of Management of Research Reactor SNF Accumulated at the Kurchatov

Institute Site" has been developed. The Programme determines the basic activity areas and their related timetables.
Besides the removal of the accumulated SNF, this Programme also provides for the liquidation of old SNF storage facilities, which have exhausted their design lifetime, at the Institute's site.
The total complex of works included in this Programme would take 5 years to complete.
Financial estimation of activities to be performed in view of preparing and removing all SNF accumulated on the Institute's site totals to about 30 million USD.
Basic areas and indicators of the activities to be performed under the Programme are summarized in Table 3.

SNF type	Number of SNF trains	Number of shipping casks			Number of SFAs		
		Cask type	In each train	Total	In each cask	In each train	Total
Pilot SFAs and fuel elements of MR reactor	4	TUK-19	16 casks	64 casks	3 SFAs or 4 canisters with fuel elements	3 trains with 48 SFAs in each, 1 train with 30 SFAs and 24 canisters with fuel elements	174 SFAs, and 491 fuel elements
Fuel elements, standard SFAs of VVR-2 and OR reactors; SFAs of IR-8 reactor	2	TUK-128	4 casks in 2 ISO-container	8 casks	7 casks with 20 canisters in each, 1 casks with 12 canisters and 8 SFAs	1 train with 80 canisters with fuel elements, and 1 train with 72 canisters with fuel elements	152 canisters with fuel elements, and 8 SFAs
SFAs from Topaz-2 reactor	4	TUK-19	3 trains with 16 casks in 2 TK-5 carriages, and 1 train with 8 casks in TK-5 carriage	56 casks	3 SFAs	3 trains with 48 SFAs in each, and 1 train with 24 SFAs	168 SFAs
SFAs from Romashka reactor	1	TUK-128	2 casks in ISO-container	2 casks	1 cask with 6 SFAs, and 1 cask with 5 SFAs	11 SFAs	11 SFAs
SFAs from RFT reactor	2	Dual-purpose rein-forced concrete casks	3 casks	6 casks	5 casks with 36 SFAs, and 1 cask with 18 SFAs	1 train with 108 SFAs, and 1 train with 90 SFAs	198 SFAs

Table 3. Basic areas and indicators of the activities under the SNF Removal Programme

7. Conclusion

It is expected that implementation of the SNF Removal Programme described above would establish a well-documented basis needed to deploy further activities on the decommissioning of retired research reactors in the Kurchatov Institute.

In future, the Institute's experience in organizing and performing the research reactor SNF management activities could be used to solve similar tasks of removing the SNF from other research reactors, including those built abroad.

RRFM IGORR 2007

LYON, France 11.3. - 15.3. 2007

European Nuclear Society
Rue de la Loi 57
1040 Brussels, Belgium
Telephone +32 2 505 30 54
Fax + 32 2 502 39 02
rrfm2007@euronuclear.org
www.euronuclear.org

Layout and Design: Marion Brünglinghaus, ENS